ABSTRACT

Title of Thesis: VARIABLE RECRUITMENT OF MINIATURE PNEUMATIC ARTIFICIAL MUSCLES AND SPACE QUALIFIED PNEUMATIC ARTIFICIAL MUSCLES.

Sylvie Adams DeLaHunt
Master of Science, 2016

Thesis Directed By: Professor Norman M. Wereley,
Department of Aerospace Engineering

The natural compliance and force generation properties of pneumatic artificial muscles (PAMs) allow them to operate like human muscles in anthropomorphic robotic manipulators. Traditionally, manipulators use a single PAM or multiple PAMs actuated in unison in place of a human muscle. However, these manipulators experience efficiency losses when operated outside their target performance ranges. The unidirectional actuation behavior of a miniature PAM bundle and bidirectional actuation behavior of an antagonistic pair of miniature PAM bundles are characterized and modeled. The results are used to motivate the application of a variable recruitment control strategy to a parallel bundle of miniature PAMs as an attempt to mimic the selective recruitment of motor units in a human muscle to improve the operating efficiency of the actuator. Additionally, the fabrication and quasi-static testing results for PAMs assembled from candidate space qualified bladder and braided sleeve materials for use in space robotics are assessed.

VARIABLE RECRUITMENT OF MINIATURE PNEUMATIC ARTIFICIAL MUSCLES AND SPACE QUALIFIED PNEUMATIC ARTIFICIAL MUSCLES.

By

Sylvie Adams DeLaHunt

Thesis submitted to the Faculty of the Graduate School of the
University of Maryland, College Park, in partial fulfillment
of the requirements for the degree of
Master of Science
2016

Advisory Committee:
Professor Norman M. Wereley, Chair
Professor Derek A. Paley
Professor Robert M. Sanner

Acknowledgements

I would like to start by thanking my advisor, Dr. Norman Wereley, for his guidance and support during my graduate research, as well as his encouragement for my pursuits outside of my graduate studies, including my involvement in Maryland's Women in Aeronautics and Astronautics student group. I would also like to thank the other members of my thesis committee, Dr. Derek Paley and Dr. Robert Sanner, for their feedback on my thesis and their flexibility with scheduling my thesis defense.

A big thank you to Tom for taking the time to introduce me to the processes for fabricating, characterizing, and modeling pneumatic artificial muscles, as well as for showing me how to operate the machine shop equipment. Thank you to Jonathan for the mechanical design suggestions and for being my group fitness class partner, and to Steve for assistance with anything computer-related. Also, thank you to Ryan and Robbie for your willingness to answer my emails about your prior research and for helping me think through challenges I faced in my own research. I would also like to thank my colleagues who helped create a supportive and fun graduate community, including Andrew, Ami, Brian, Lauren, Elaine, Elizabeth, Elena, Will, and Will.

Thank you to Tom and Aileen and the rest of the Department of Aerospace Engineering for always being so helpful and for creating a welcoming environment throughout my undergraduate and graduate studies at Maryland.

I would not be where I am today with the amazing support of my parents. Thank you mom and dad for pushing me to achieve my dreams, teaching me to fight for what I believe in, and encouraging me to pursue all of my interests, both within and outside of engineering. And a special thank you to Rubbel for

your continuous support throughout the past two years of completing my graduate degree—I am really excited for what our future holds!

Finally, this material is based upon work supported by the National Science Foundation Graduate Research Fellowship under Grant No. DGE 1322106.

Table of Contents

List of Tables

List of Figures

1. Introduction

1.1. Background and Motivation

1.1.1. Pneumatic Artificial Muscles

The complex composition of human muscles allows them to generate forces and motion. Muscles are made up of muscle fiber bundles with a thick, interwoven layer of connective tissue. Strong bundles of fibrous tissue form tendons, which connect the ends of muscles to bones. When muscles contract, tendons pull on the adjacent bones, causing the bones to move about joints in response. Parallel muscles have muscle fiber bundles that are aligned in parallel with one another along the axial dimension of the muscle. A fusiform muscle is a specific type of parallel muscle that is spindle-shaped with a wider middle segment and thinner, stronger tendons at each end. During contraction, the middle of a fusiform muscle grows in width and shrinks in length, preserving its volume (Tözeren 2000, Watkins 2014).

Pneumatic artificial muscles (PAMs), also referred to as McKibben artificial muscles, are lightweight actuators composed of an elastomeric tube inside a braided sleeve with two end fittings. When pressurized through one of their two end fittings, the braid orientation causes PAMs to expand radially and contract axially, generating a pulling force in the axial direction until an equilibrium position is achieved. PAMs produce their maximum force when held at their resting state (blocked force) and zero force after being allowed to fully contract to their actuated state (free contraction). Figure 1.1 shows a PAM being held at its blocked force and free contraction states. The natural

compliance of PAMs and their method of force generation allow them to operate like human fusiform muscles as "soft" actuators for use in bioinspired robotics. Like human muscles, PAMs can only generate pulling axial forces, not pushing forces.

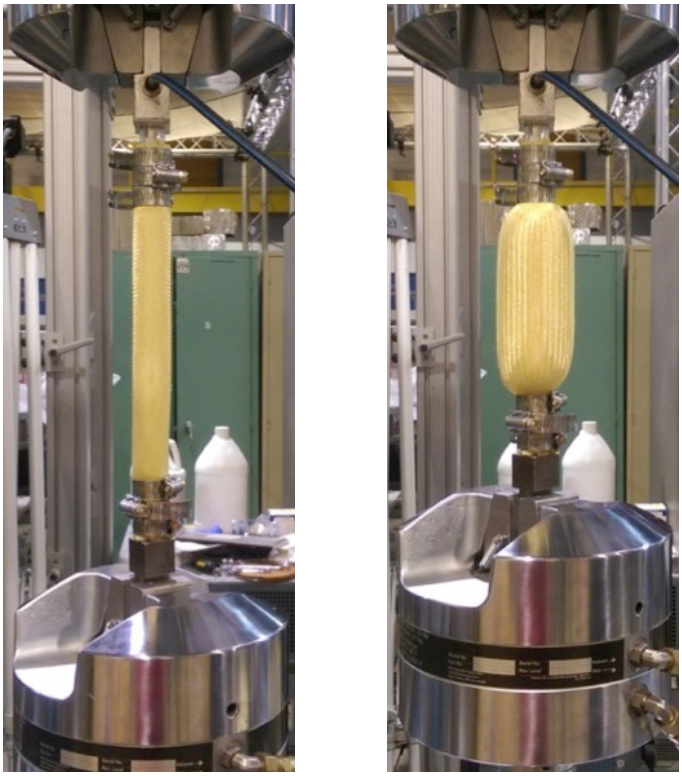

(a) Blocked Force (b) Free Contraction

Figure 1.1: A PAM held at its (a) blocked force state and (b) free contraction state during quasi-static testing in a servo-hydraulic test machine.

Researchers have investigated the use of PAMs in various robotic designs, including robotic hands (Boblan *et al.* 2003, Röthling *et al.* 2007), arms (Tondu *et al.* 2005, Robinson *et al.* 2011), legs (Colbrunn 2000, Vermeulen 2006) and rehabilitative designs (Caldwell and Tsagarakis 2002, Park *et al.* 2014). PAMs have also been as actuators for aerospace applications, including morphing wings (Peel *et al.* 2009) and trailing edge flaps (Woods *et al.* 2011, Woods *et al.* 2014). Due to their natural

compliance, PAMs can be a safer choice than traditional actuators for use in robotic manipulators intended to interact with humans (Tondu 2012).

PAMs have a simple structure and can be fabricated in a range of sizes depending on the availability of appropriate bladder and braided sleeve materials. Recent research has been conducted on the fabrication, testing, and modeling of miniature PAMs for use in small-scale robots and micro-air vehicles (Chen *et al.* 2011, De Volder *et al.* 2011, Vocke *et al.* 2012, Hocking and Wereley 2013, Pillsbury *et al.* 2015). Typically, the diameters of miniature PAMs are on the order of millimeters, while the diameters of full-scale PAMs are on the order of tens of millimeters.

Additional benefits of PAMs include their high power-to-weight ratios and specific work at low actuation pressures (Chou and Hannaford 1994, Robinson *et al.* 2011, Vocke *et al.* 2012). PAMs have excellent fatigue-resistance properties and have been endurance tested for over 120 million cycles with minimal wear and no noticeable performance degradation (Woods *et al.* 2012). For a more detailed review of PAMs, see Tondu (2012).

1.1.2. Variable Recruitment

Motor units are the smallest controllable units within human muscles. Each motor unit is composed of a bundle of muscle fibers, which contract in unison as the motor unit is activated. Currently, anthropomorphic robotic manipulators regularly employ a single PAM to act in place of a human muscle. However, human muscles operate through selective recruitment of their motor units. The muscular force produced by a human muscle can be increased by increasing the firing rate of the active motor units, or by exciting (recruiting) additional motor units (Erim *et al.* 1996, Winter 2005).

According to Henneman's size principle, the smaller, lower force, fatigue-resistant motor units in a human muscle are recruited before larger, higher force, less fatigue-resistant motor units (Henneman *et al.* 1965a, Henneman *et al.* 1965b, Winter 2005). The human nervous system can recruit the appropriate amount of muscle fibers to most efficiently perform a wide variety of tasks, ranging from precise movements to high force pushing and pulling, only recruiting the least fatigue-resistant motor units when necessary.

Only recently have researchers begun assessing the application of a similar variable recruitment control strategy to PAMs as an attempt to mimic the selective recruitment of motor units in human muscles. Azizi and Roberts (2013) assessed variable gearing in a pennate array of PAMs, where the PAMs were arranged at an angle offset from the axial direction of the muscle. Bryant *et al.* (2014) were able to generate a range of forces through separate and combined actuation of two motor units in a parallel bundle of fluidic artificial muscles (FAMs). When considering variable recruitment in the shoulder joint of a robotic manipulator with a parallel arrangement of PAMs, Robinson *et al.* (2014) observed the efficiency benefits of activating fewer PAMs at higher operating pressures, where a smaller percentage of the total input energy to the system is lost in overcoming the initial radial elasticity of PAM bladders. Meller *et al.* (2015) varied the number of FAMs recruited in the muscle bundle of a bipedal robot as a method of reducing throttling losses.

When a bundle of PAMs is operated like a human muscle bundle, a single PAM represents a muscle fiber, while a set of PAMs actuated in unison, such as those connected to a single pressure valve, represent a motor unit. In human muscles, muscular

force is increased by either increasing the firing rate of active motor units or by recruiting additional motor units. In bundle of PAMs, additional force can be generated by increasing the actuation pressure of active PAMs or by pressurizing additional PAMs. The application of a variable recruitment strategy to a bundle of PAMs would allow the appropriate number of PAMs to be recruited to most efficiently complete a given task, thereby allowing a single bundle to more efficiency perform a variety of tasks requiring wider ranges of force production or contraction.

1.1.3. Antagonistic Pairs

Human muscles operate as agonist, synergist, or antagonist muscles. When activated, agonist muscles contract and generate a pulling force to perform a desired motion, such as flexion or extension about a joint. Synergist muscles assist agonist muscles at the onset of motion and help stabilize the motion about the joint. In response to the motion of the agonist muscles, the relaxed antagonist muscles extend and produce an opposing force. The body's nervous system regulates muscular forces to achieve controlled movement (Tözeren 2000). The same muscle group can operate as either an agonist or an antagonist muscle group depending on whether it is in contraction or extension, with the range of motion dictated by its corresponding human joint.

The biceps-triceps pair of muscles is one example of an antagonistic muscle pair. The biceps produce the flexion movement about the elbow joint, while the triceps produce the corresponding extension movement. The quadriceps and hamstring are another example of an antagonist pair, producing the flexion and extension movements about the knee. Muscles generate force through pulling, but they cannot generate pushing

forces, which is why an antagonistic muscle pair is needed to produce bidirectional motion around human joints.

Like human muscles, PAMs are unidirectional actuators that can only generate pulling forces in the axial direction. When pressurized, PAMs expand radially and contract axially, generating an axial pulling force proportionate to their level of contraction. PAMs are designed to operate like human muscles in the agonist role. However, PAMs can also serve in the role of an antagonist muscle. When operated as antagonist muscles, PAMs create opposing forces to resist stretching, proportionate to the amount they are stretched. PAMs have a high passive stiffness and their antagonistic force increases substantially as they are extended past their resting length. Like agonist PAM forces, antagonist PAM forces also increase with pressure and experience hysteresis during their loading and unloading cycles (Vocke *et al.* 2014).

A unidirectional PAM actuator must be operated in an agonist-antagonist configuration for applications requiring bidirectional motion, such as trailing edge flaps (Woods *et al.* 2011, Woods *et al.* 2014) and robotic arms (Tondu *et al.* 2005, Ariga *et al.* 2012). When two PAMs are connected about a pivot point as an antagonistic pair, as depicted in Fig. 1.2, either PAM can be pressurized to act as the agonist muscle or relaxed to act as the antagonist muscle. This configuration allows PAMs to produce bidirectional motion.

When two PAMs are operated as an antagonistic pair, the antagonist PAM generates an opposing force to counter the force generated by agonist PAM. The achievable deflection and available work of the system when operated with an antagonist muscle pair is significantly limited due to the high passive stiffness of the antagonist

PAM as it is stretched past its resting length. Two regularly implemented modifications to improve the system performance are choosing system geometry that decreases the passive torque and introducing a bias contraction with a corresponding bias pressure to maintain joint stiffness (Vocke *et al.* 2014).

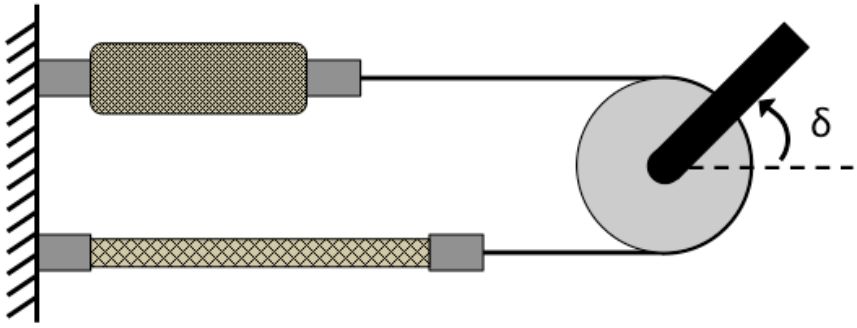

Figure 1.2: A simple bidirectional actuator with two PAMs in an agonist/antagonist configuration.

1.1.4. Space Qualified PAMs

PAMs are used in robotic manipulators, including robotic hands (Boblan *et al.* 2003, Röthling *et al.* 2007), arms (Tondu *et al.* 2005, Robinson *et al.* 2011), and legs (Colbrunn 2000, Vermeulen 2006). Researchers have developed pneumatically actuated power assist devices for hand gripping (Sasaki *et al.* 2004, Tadano *et al.* 2010, Wu *et al.* 2010) and arm actuation (Ying *et al.* 2007), which could be applied to improve the mobility of hands and arms in pressure suits (Salmoiraghi and Akin 2012). Pillsbury *et al* (2015) considered the use of miniature PAMs to pneumatically power an extra-vehicular activity (EVA) glove exoskeleton to improve the dexterity of astronauts wearing EVA gloves.

There are numerous applications for robotics in space, examples of which include rovers, the Space Shuttle Robotic Manipulator System, and the International Space

Station Mobile Servicing System. Wilcox *et al.* (2006) provide a review of space robotics. However, little prior research has been conducted related to the use of PAMs as actuators for space robotics.

Key benefits of PAMs include their high power-to-weight ratios and specific work at low actuation pressures (Chou and Hannaford 1994, Robinson *et al.* 2011, Vocke *et al.* 2012). PAMs have a simple structure that can be assembled from commercially available materials. Additionally, PAMs have been endurance-tested for over 120 million loading cycles with minimal wear and without any noticeable performance degradation (Woods *et al.* 2012). Although the range of applicable bladder and braided sleeve materials would be limited for space-qualified PAMs, the high power-to-weight ratios and specific work offer potential weight-savings benefits over traditional electric motors. Additionally, the excellent durability and fatigue-resistance properties of PAMs would be beneficial for longer duration space robotics missions.

To utilize PAMs in space robotics, researchers must determine the appropriate choice of space-qualified materials to use as PAM bladders and braided sleeves. Finckenor and de Groh (2015) provide an overview of the necessary considerations when selecting materials for use in space in *Space Environment Effects* from NASA's International Space Statin Researcher's Guide Series. Materials in space are exposed to vacuum, radiation, atomic oxygen, and thermal cycling. They risk contamination and impacts from debris. NASA maintains a handbook that overviews the appropriate measures for conducting material testing at ground facilities.

To meet space qualification requirements, PAMs must be fabricated from space qualified materials that will perform well during mass loss testing, temperature range

evaluations, and thermal cycling. Additionally, the PAMs must be capable of handling the necessary loading for space robotics applications.

1.2. Contributions of Thesis Research

The first objective of this research was to investigate and model the unidirectional actuation behavior of bundles of miniature PAMs and the bidirectional actuation behavior of an antagonistic pair of miniature PAMs bundles. The experimental and modeling results, comparisons of energy equivalent configurations, and efficiency assessments are used to motivate the application of a variable recruitment control strategy to bundles of miniature PAMs as an attempt to mimic the selective recruitment of motor units in human muscles. This bioinspired control strategy would allow muscle bundles to operate the fewest number of miniature PAMs necessary to achieve a desired performance objective, thereby improving the efficiency of PAM actuated robotic manipulators over wider ranges of force generation and displacement. The quasi-static agonist and antagonist unidirectional actuation behavior of the miniature PAM bundles, as well as the bidirectional actuation behavior of an antagonistic pair of miniature PAM bundles, are characterized and modeled to improve understanding of the actuation behavior of the bundles for use in robotic manipulators.

Prior variable recruitment work has been restricted to full-scale PAMs and FAMs, and has only considered the unidirectional actuation behavior of artificial muscle bundles (Bryant *et al.* 2014, Robinson *et al.* 2014, Meller *et al.* 2015). Miniature PAMs can be used to assemble more compact muscles bundles with greater quantities of motor units, which would be more representative of the composition of human muscle bundles. Additionally, considering the unidirectional and bidirectional actuation behavior of

bundles of miniature PAMs provided additional insights into the bundle behavior that would be less noticeable at larger scales, leading to improved modeling techniques.

The second objective of this research was to assess whether PAMs assembled from candidate space qualified materials were able to handle the necessary loads and achieve the performance requirements for space robotics applications, and to compare the relative actuation performance of different bladder and braided sleeve materials.

1.3. Overview of Thesis

This thesis is organized into five chapters. A majority of the thesis work relates to the characterization and modeling of the actuation behavior of bundles of miniature PAMs as unidirectional actuators or as bidirectional actuators in an antagonist pair configuration. The remainder of the research covers the fabrication and characterization of full-scale PAMs for space qualified robotic applications.

Chapter 1: Introduction. This chapter presents an overview of the background and motivation for considering the applicable of a variable recruitment control technique to bundles of miniature PAMs, and for the development of PAMs from space qualified materials for space robotics. It also covers the objectives of the present research.

Chapter 2: Variable Recruitment of Miniature Pneumatic Artificial Muscles. This chapter describes the characterization of the agonistic actuation behavior of bundles of miniature PAMs, as well as a new modeling technique to account for the length variations of miniature PAMs in a bundle. It motivates the application of a variable recruitment control strategy through the consideration of energy equivalent configurations and an efficiency analysis.

Chapter 3: Antagonistic Pair of Bundles of Miniature Pneumatic Artificial Muscles. The antagonistic actuation behavior of miniature PAMs are characterized and modeled. A description of the development of a bidirectional actuator with an agonist/antagonist configuration of miniature PAM bundles is provided. Characterization and modeling of the quasi-static behavior of the bidirectional actuator is described.

Chapter 4: Space Qualified Pneumatic Artificial Muscles. The fabrication and quasi-static testing observations and results for full-scale PAMs assembled from candidate space qualified bladder and braided sleeve materials are discussed and compared in this chapter.

Chapter 5: Conclusions. The key findings and observations from the previous chapters are summarized. Also discussed are the contributions of this work, as well as suggestions for future work.

2. Variable Recruitment in Bundles of Miniature Pneumatic Artificial Muscles

2.1. Introduction

The complex composition of human muscles allows them to generate forces and motion. Muscles are made up of muscle fiber bundles with a thick, interwoven layer of connective tissue. Strong bundles of fibrous tissue form tendons, which connect the ends of muscles to bones. When muscles contract, tendons pull on the adjacent bones, causing the bones to move about joints in response. Parallel muscles have muscle fiber bundles that are aligned in parallel with one another along the axial dimension of the muscle. A fusiform muscle is a specific type of parallel muscle that is spindle-shaped with a wider middle segment and thinner, stronger tendons at each end. During contraction, the middle of a fusiform muscle grows in width and shrinks in length, preserving its volume (Tözeren 2000, Watkins 2014).

2.1.1. Pneumatic Artificial Muscles

Pneumatic artificial muscles (PAMs), also referred to as McKibben artificial muscles, are lightweight actuators composed of an elastomeric tube inside a braided sleeve with two end fittings. When pressurized through one of their two end fittings, the braid orientation causes PAMs to expand radially and contract axially, generating a pulling force in the axial direction until an equilibrium position is achieved. PAMs generate their maximum force when held at their resting state, and zero force after being allowed to fully contract to their actuated state. The natural compliance of PAMs and

their method of force generation allow them to operate like human fusiform muscles as "soft" actuators for use in bioinspired robotics.

Researchers have investigated the use of PAMs in various robotic designs, including robotic and prosthetic hands (Boblan *et al.* 2003, Röthling *et al.* 2007), arms (Tondu *et al.* 2005, Robinson *et al.* 2011), legs (Colbrunn 2000, Vermeulen 2006) and rehabilitative designs (Caldwell and Tsagarakis 2002, Park *et al.* 2014). Due to their natural compliance, PAMs can be a safer choice than traditional actuators for use in robotic manipulators intended to interact with humans (Tondu 2012).

Additional benefits of PAMs include their high power-to-weight ratios and specific work at low actuation pressures (Chou and Hannaford 1994, Robinson *et al.* 2011, Vocke *et al.* 2012). PAMs have a simple structure, can be assembled from commercially available materials, and have excellent fatigue-resistance properties (Klute and Hannaford 1998, Woods *et al.* 2012). For a more detailed review of PAMs, see Tondu (2012).

2.1.2. Variable Recruitment

Motor units are the smallest controllable components of human muscles. Each motor unit is composed of a bundle of muscle fibers, which contract in unison as the motor unit is activated. Currently, anthropomorphic robotic manipulators regularly employ a single PAM to act in place of a human muscle. However, human muscles operate through selective recruitment of their motor units. The muscular force produced by a human muscle can be increased by increasing the firing rate of the active motor units, or by exciting (recruiting) additional motor units (Erim *et al.* 1996, Winter 2005).

According to Henneman's size principle, smaller, slower-twitch motor units, which have better fatigue-resistance and lower force production, are recruited first. Larger, faster-twitch motor units, with worse fatigue-resistance and higher force production, are recruited last (Henneman *et al.* 1965a, Henneman *et al.* 1965b, Winter 2005). The nervous system can recruit the appropriate amount of muscle fibers to perform a wide variety of tasks, ranging from precise movements to high force pushing and pulling, only recruiting the least fatigue-resistant motor units when necessary.

2.1.3. Variable Recruitment Applied to Pneumatic Artificial Muscles

Only recently have research groups started considering the application of a similar variable recruitment control strategy to PAMs as an attempt to mimic the selective recruitment of motor units in human muscles. Azizi and Roberts (2013) assessed variable gearing in a pennate array of PAMs, where the PAMs were arranged at an angle offset from the axial direction of the muscle. Bryant *et al.* (2014) were able to generate a range of forces through separate and combined actuation of two motor units in a parallel bundle of fluidic artificial muscles (FAMs). When considering variable recruitment in the shoulder joint of a robotic manipulator with a parallel arrangement of PAMs, Robinson *et al.* (2014) observed the efficiency benefits of activating fewer PAMs at higher operating pressures, where a smaller percentage of the total input energy to the system is lost in overcoming the initial radial elasticity of PAM bladders. Meller *et al.* (2015) varied the number of FAMs recruited in the muscle bundle of a bipedal robot as a method of reducing throttling losses.

The following study continues this previous work by extending the application of a variable recruitment control strategy to a parallel bundle of miniature PAMs. The

properties of parallel bundles of miniature PAMs are characterized, a model is proposed to predict the force generation and contraction behavior of bundles, and the model is used to assess the efficiency gains and losses associated with the application of a variable recruitment control technique to muscle bundles. Miniature PAMs can be used to assemble more compact muscles bundles with larger quantities of motor units that are more representative of the composition of human muscle bundles. Additionally, the smaller size of miniature PAMs offered additional insight into the behavior of bundles, leading to an improved modeling technique.

In the following study, a single miniature PAM represents a muscle fiber, a pair of miniature PAMs actuated in unison via a single pressure valve represent a motor unit, and the entire bundle of miniature PAMs represents a human muscle bundle. In human muscles, muscular force is increased by increasing the firing rate of active motor units or by recruiting additional motor units. In miniature PAM bundles, additional force can be generated by increasing the actuation pressure of active miniature PAMs or by pressurizing additional miniature PAMs. This strategy allows the appropriate number of miniature PAMs to be recruited to most efficiently complete a given task, thereby allowing a single bundle to more efficiency perform a variety of tasks requiring wider ranges of force production and contraction.

2.2. Fabrication and Characterization

2.2.1. Fabrication of Miniature PAMs

Due to their simple structure, PAMs can be fabricated in a range of sizes. Recent research has been conducted on the fabrication, testing, and modeling of miniature PAMs

for use in small-scale robots and micro-air vehicles (Chen *et al.* 2011, De Volder *et al.* 2011, Vocke *et al.* 2012, Hocking and Wereley 2013, Pillsbury *et al.* 2015). Typically, the diameters of miniature PAMs are on the order of millimeters, while the diameters of full-scale PAMs are on the order of tens of millimeters.

For this study, the miniature PAMs were assembled from commercially available materials. The bladders were cut from natural rubber tubing with an inner diameter of 3.175 mm (0.125 in) and a wall thickness of 0.787 mm (0.031 in). The braids were cut from a Kevlar braided sleeve with a nominal diameter of 6.35 mm (0.25 in). After the bladder was inserted into the braided sleeve, the braided sleeve had a nominal braid angle of 59°. The end fittings were machined from #10-32 fully threaded aluminum studs. The miniature PAMs were held together with epoxy and end caps cut from aluminum tubing with an outer diameter of 6.35 mm (0.25 in) and a wall thickness of 0.406 mm (0.016 in).

Two end fittings per miniature PAM were machined using a lathe. The threaded aluminum studs were stepped down so that their first 6.35 mm (0.25 in) in length had outer diameters of 3.2 mm (0.126 in) to allow a snug fit when the end fittings were inserted into the bladders. The remaining lengths of the two studs were left unaltered, so that the miniature PAMs could be screwed into attachment pieces by their end fittings for testing. Small ridges were then cut into the stepped-down portion of the studs to create more contact area for epoxy to seal the end fittings to the bladder. Finally, a 2.083 mm (0.082 in) through-hole was drilled through one of the two end fittings. This “open” end fitting was later used to supply pressurized air to the assembled miniature PAM for actuation. The other end fitting remained “closed.”

The natural rubber tubing for the bladder was cut to a length of 63.5 mm (2.5 in), plus an additional 12.7 mm (0.5 in) to accommodate the stepped-down portion of the two end fittings. The Kevlar braided sleeve was cut to a sufficient length to encompass the bladder, plus the lengths of the two end fittings, with additional length to account for fraying of the ends of the braid. Two end caps, with lengths of 11.43 mm (0.45 in), were cut from the aluminum tubing. The materials before and after assembly can be seen in Fig. 2.1a.

To begin the assembly process, a thin layer of Hardman Part A and Part B 8173 epoxy were applied to the outside of the stepped-down portion of the "open" end fitting, with care taken not to get any epoxy inside the through-hole. The stepped-down portion of the end fitting was then inserted into one end of the bladder. Once the epoxy cured, the bladder was inserted into the Kevlar braid, and then the two end caps were slid over the bladder and braid. The epoxy was applied to the stepped-down portion of the remaining end fitting. With the braid pushed back to expose the open end of the bladder, the stepped-down portion of the second end fitting was inserted into this open end of the bladder. After the Hardman epoxy was left to cure for half an hour, a thin layer of Loctite E-90FL Hysol Epoxy Adhesive was rubbed onto the braid over the segment where one of the two end fittings had been inserted into the bladder. One end cap was then slid over epoxy, and any excess epoxy was removed. This process was repeated for the other end cap. After this epoxy cured for a day, one end of the miniature PAM was inserted into a 6.35 mm (¼ in) collet so that the inner edge of the end cap was aligned with the edge of the collet. Then the collet was inserted into a collet holder and tightened to strengthen the bond between the end fitting, bladder, braid, and aluminum tubing. This crimping process

was repeated for the other end cap of the miniature PAM. Once finished, the leftover braid material extending past the end caps was removed. The eight fully assembled miniature PAMs used in this study can be seen in Fig. 2.1b.

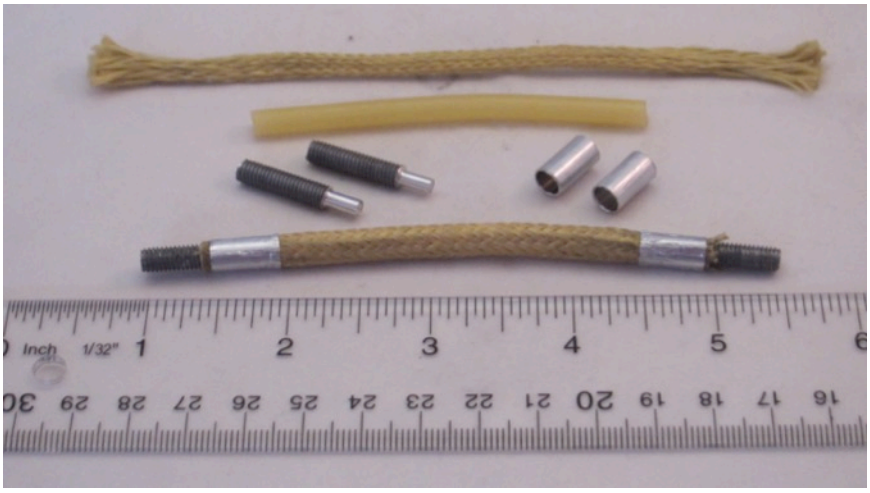

(a) Miniature PAM materials

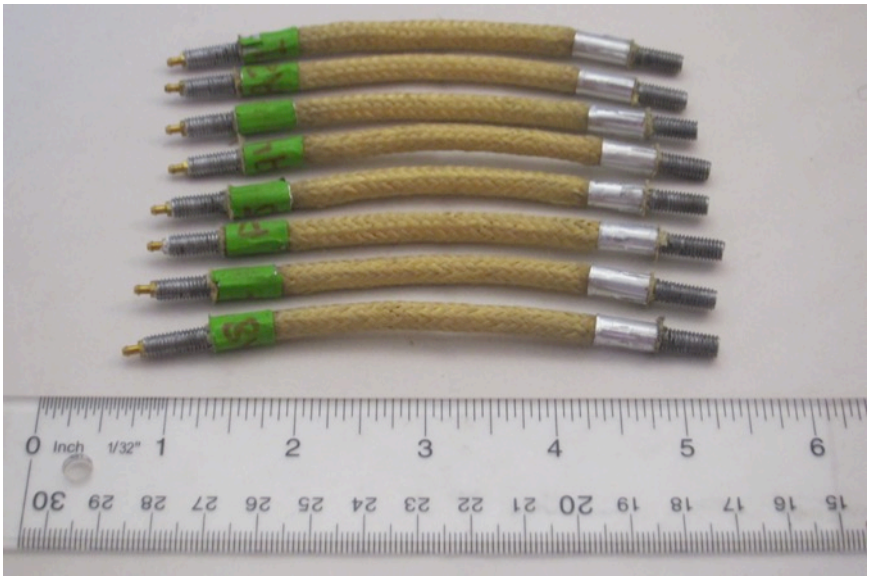

(b) Assembled miniature PAMs

Figure 2.1: Miniature PAM materials and assembled miniature PAMs.

The eight miniature PAMs produced for the study had “active” lengths (natural resting lengths of unpressurized PAMs) ranging from 6.63 cm (2.61 in) to 7.06 cm (2.78

in) with an average active length of 6.77 cm (2.66 in) and a standard deviation of 0.14 cm (0.05 in). The outer diameter of each miniature PAM was 0.56 cm (0.22 in). The active length for each miniature PAM is provided in Table 2.1.

2.2.2. Experimental Characterization of Miniature PAMs

Experimental characterization of the performance of each miniature PAM was completed through quasi-static testing using a 100 kN (22 kip) MTS servo-hydraulic test machine. Testing was used to evaluate the relationship between operating pressure, force, and contraction for the miniature PAMs. During testing, each miniature PAM was pressurized to a specified operating pressure, and then cycled in the MTS machine between its blocked force and its free contraction states. The blocked force at a given pressure is the maximum force produced by a pressurized PAM, which occurs when it is held at its active length. The free contraction at a given pressure is the maximum stroke of a pressurized PAM, which occurs at the contracted length when the PAM no longer produces any force. A PAM being held at its blocked force and free contraction states can be seen in Fig. 2.2.

The MTS machine collected displacement data during testing to measure the contraction of the miniature PAMs, while force data was collected with a Honeywell load cell (Model No. 31) rated for 445 N (100 lb). The Honeywell load cell provided more accurate force measurements than the larger load cell in the MTS machine for the low forces generated by the miniature PAMs. Pressurized air was supplied to the miniature PAMs by a Husky Pro 227 L (60 gal) air compressor, and the pressure was regulated with a Wilkerson Dial-Air pressure regulator (model No. R21-04-000) with an SSI Technologies, Inc. digital pressure gauge (Part No. MGA-300-A-9V-R).

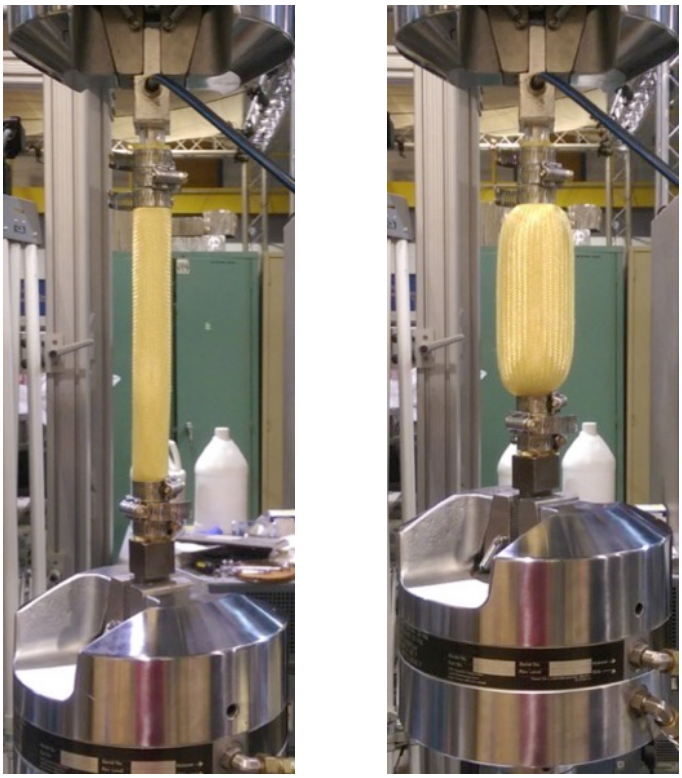

(a) Blocked Force (b) Free Contraction

Figure 2.2 A PAM held at its (a) blocked force state and (b) free contraction state during quasi-static testing in a servo-hydraulic test machine.

While being held at its resting length by the MTS grips, the miniature PAM was pressurized to the desired operating pressure for the given test. After being pressurized, the miniature PAM was briefly held at its blocked force state. The miniature PAM was then allowed to fully contract through a controlled movement. After briefly resting at this free contraction state, the machine returned the miniature PAM to its blocked force state, completing one cycle. Three cycles were completed per test.

The Mullins effect describes the stress softening of a bladder material that causes the blocked force and free contraction values for a PAM to increase with each cycle during the initial stretching of a bladder at new, higher operating pressures (Diani *et al.* 2009, Hocking and Wereley 2013). Prior to the start of testing, each miniature PAM was

cycled between its blocked force and free contraction states, until these peak values stabilized, to limit the influence of the Mullins effect on the experimental data. A pressure of 655 kPa (95 psi), 34.5 kPA (5 psi) greater than the maximum operating pressure for the tests, was chosen for the initial cycling. Due to the specific natural rubber tubing selected as the bladder material, the miniature PAMs for this test typically only needed to be cycled three times before the stress-softening effects became negligible. The miniature PAM tests were completed at testing pressures of 621 kPa (90 psi) through 68.9 kPa (10 psi), in 68.9 kPa (10 psi) increments. At each new testing pressure, the miniature PAM was first cycled between blocked force and free contraction to ensure that the peak force and contraction values were consistent.

The experimental results for one miniature PAM are plotted in Fig. 2.3a. The hysteresis in the data is a consequence of internal friction in the miniature PAM (Chou and Hannaford 1996, Davis and Caldwell 2006). The bottom half of each curve is the unloading portion (from blocked force to free contraction) and the top half is the loading portion (from free contraction to blocked force). The data shown in Fig. 2.3b is the average data for each pressure curve. To simplify the following data analyses and modeling, the remainder of this chapter will only consider the average experimental data.

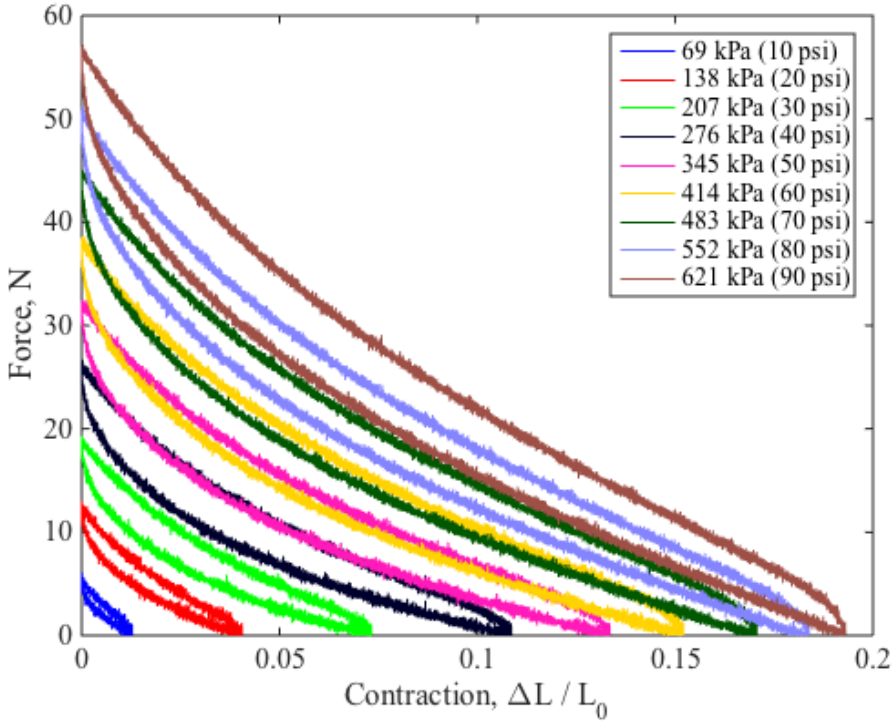

(a) Experimental data

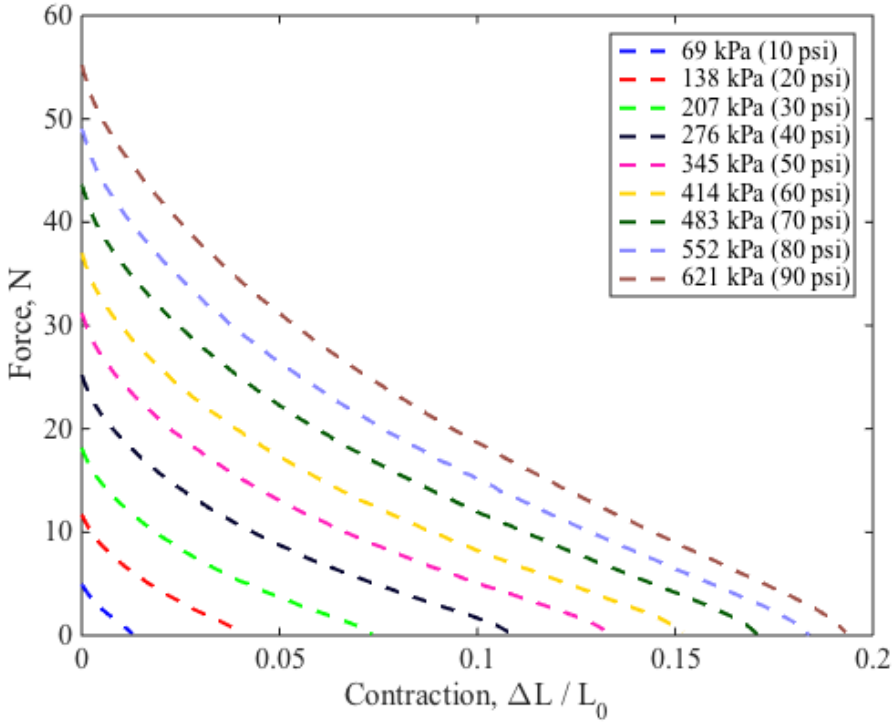

(b) Average data

Figure 2.3: Experimental data and average experimental data from the tensile testing of a single miniature PAM.

The properties determined through the experimental testing are described in Table 2.1. The maximum blocked force and free contraction values correspond to the maximum test pressure, with a nominal maximum test pressure of 621 kPa (90 psi). Additionally, blocked force values linearly corrected to correspond to 621 kPa (90 psi) are provided. The variation in free contraction is nonlinear and the difference between the original values and values corrected to correspond to 621 kPa (90 psi) are negligible, with a percent change of less than 1%. As seen in Table 2.1, the miniature PAMs used in this study produced an average force of 55.5 N (12.5 lb) when pressurized to 621 kPa (90 psi) and contracted 19.0% or 1.28 cm (0.50 in) on average. Although the standard deviation for the parameters are small when compared to the average values, they do highlight the impreciseness of miniature PAM manufacturing techniques, resulting in slight differences in sizing and performance characteristics.

Table 2.1: Summary of properties of the individual miniature PAMs from experimental characterization.

PAM No.	Active Length (cm)	Max. Test Pressure (kPa)	Max. Blocked Force (N)	Max. Blocked Force (Corrected to 621 kPa) (N)	Max. Free Contraction (cm)	Max. Free Contraction (%)
1	7.06	621	52.93	52.93	1.36	19.3
2	6.73	607	55.20	56.47	1.24	18.5
3	6.78	616	53.42	53.85	1.28	18.9
4	6.68	616	53.69	54.13	1.22	18.2
5	6.73	624	56.18	55.91	1.27	18.8
6	6.86	623	57.12	56.94	1.36	19.9
7	6.63	612	56.14	56.97	1.25	18.8
8	6.68	625	57.25	56.88	1.29	19.3
Avg.	6.77	618	55.24	55.51	1.28	19.0
Std. Dev.	0.14	6	1.70	1.62	0.05	0.5

2.2.3. Experimental Characterization of Miniature PAM Bundles

A simple aluminum structure was assembled to hold together a bundle of up to eight miniature PAMs in a cruciform configuration. To reduce the likelihood of exposing the load cell to bending forces, the design was chosen to allow the miniature PAMs to be recruited in pairs of two, while maintaining the balance of forces about the center of the structure. Additionally, to prevent frictional forces from affecting the experimental data, adequate spacing of 2.54 cm (1 in) between the center axis of each adjacent miniature PAM was chosen to allow the miniature PAMs to expand without coming into contact with one another. Before and after pictures of assembly of the miniature PAM bundle and the aluminum structure holding the bundle together can be seen in Fig. 2.4.

For this study, the specified recruitment pattern from two to eight miniature PAMs can be seen in Fig. 2.5. This miniature PAM bundle has four motor units of two miniature PAMs recruited in unison each. For experimental characterization of the bundles, the miniature PAMs were paired based on their blocked force values from Table 2.1. The first two miniature PAMs recruited were No. 6 and No. 8, with blocked forces of 57.1 N (12.8 lb) and 57.2 N (12.9 lb) respectively. Then, No. 5 and No. 7, with blocked forces of 56.2 N (12.6 lb) and 56.1 N (12.6 lb), were recruited to achieve four total active PAMs. Next, No. 1 and No. 3, with blocked forces of 52.9 N (11.9 lb) and 53.4 N (12.0 lb) respectively, were recruited to achieve six total active PAMs. Finally, No. 2 and No. 4, with blocked forces of 55.2 N (12.4 lb) and 53.7 N (12.1 lb) respectively, were recruited to achieve the maximum eight total recruited miniature PAMs for this bundle. Similar experimental results were achieved with different pairings of miniature PAMs;

however, only the results from the specific recruitment order specified above are provided for brevity.

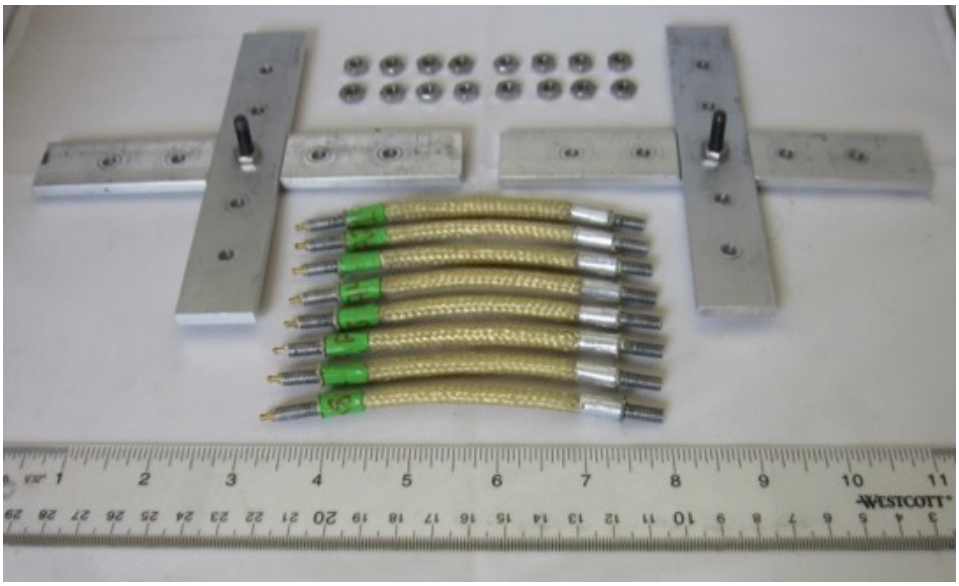

(a) Pre-assembly

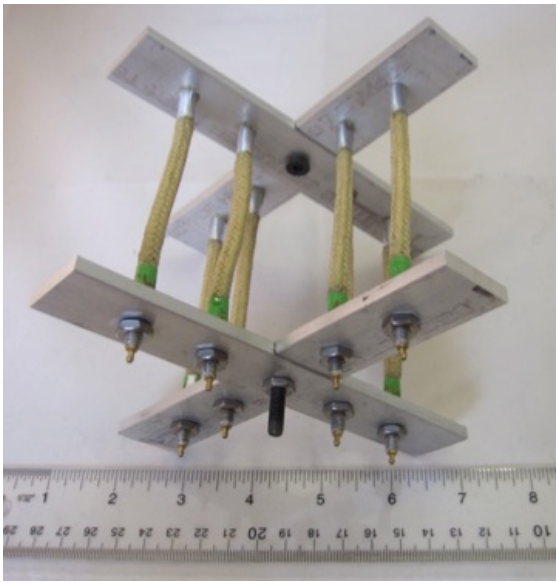

(b) Post-assembly

Figure 2.4: Pre-assembly and post-assembly images of the bundle of miniature PAMs.

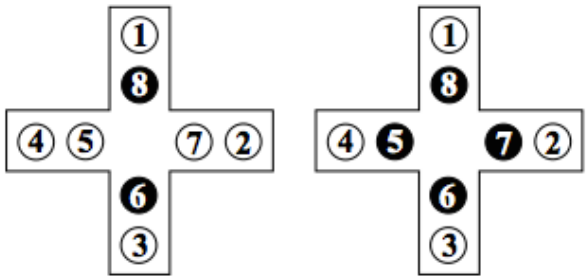

(a) 2 active PAMs (b) 4 active PAMs

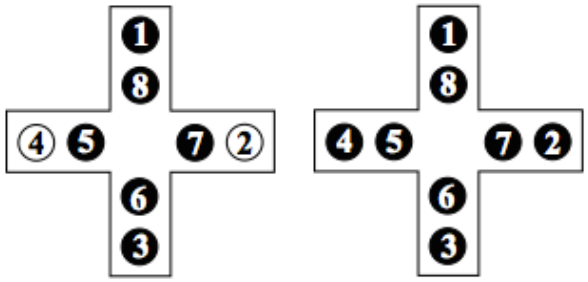

(c) 6 active PAMs (d) 8 active PAMs

Figure 2.5: Variable recruitment order for the bundles of miniature PAMs used in this study. A black circle indicates an active miniature PAM and a white circle indicates an inactive miniature PAM or no miniature PAM.

A similar experimental characterization approach and test setup were used for the bundles of miniature PAMs as were used to characterize the actuation behavior of the individual miniature PAMs. The structure holding the bundles was designed to clamp into the MTS grips, and the bundle was cycled between its blocked force and free contraction states at internal pressures ranging from 552 kPa (80 psi) to 138 kPa (20 psi) in 138 kPa (20 psi) increments. Air was supplied individually to each miniature PAM in the bundle through a hose fitting. Due to the pressure limitations of the hose fittings, a maximum pressure of 552 kPa (80 psi) was chosen for the bundles, rather than 621 kPa (90 psi), as was used for the individual miniature PAMs. The bundles were cycled at testing pressures within the range of test pressures used to experimentally characterize each PAM individually, so no additional cycling was necessary to account for the Mullins effect. A bundle of eight miniature PAMs, with two active (pressurized) miniature PAMs

and six inactive (unpressurized) miniature PAMs, can be seen at its blocked force state in Fig. 2.6. The natural compliance of the miniature PAMs can be observed in the figure where the inactive miniature PAMs bend out of the way as the active miniature PAMs are allowed to axially contract.

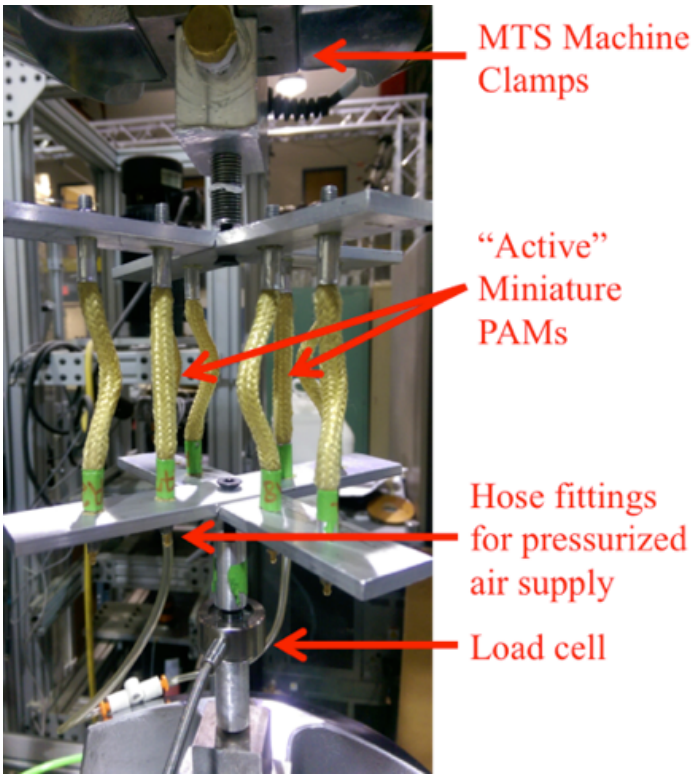

Figure 2.6: A bundle of two active and six inactive miniature PAMs in an MTS servo-hydraulic test machine.

Table 2.2 contains the blocked force and free contraction data for the bundles characterized both with and without the inactive miniature PAMs included in the bundles. With the inactive miniature PAMs in-situ, the total number of miniature PAMs in the bundle is equal to eight, regardless of the number of active miniature PAMs. With the inactive miniature PAMs ex-situ, the total number of miniature PAMs in each bundle is equivalent to the total number of active miniature PAMs. The former in-situ configuration is more representative of a variable recruitment scenario, where the total

number of miniature PAMs would remain constant as the active number of miniature PAMs changed to meet varying performance requirements. However, the collection of both sets of data allowed the effect of the inactive miniature PAMs on the bundle performance to be observed. Note that for eight active miniature PAMs, there are zero inactive miniature PAMs in each case.

Table 2.2: Properties of bundles with inactive miniature PAMs in-situ and ex-situ.

No. of Active PAMs	Max. Blocked Force			Max. Free Contraction		
	Ex-situ (N)	In-situ (N)	% change (%)	Ex-situ (%)	In-situ (%)	% change (%)
1*	57.2	n/a	n/a	19.3	n/a	n/a
2	89.7	79.8	11.0	15.9	12.8	19.3
4	172.4	168.9	2.0	16.1	15.2	5.6
6	241.4	221.9	2.0	16.1	15.1	6.2
8	291.8	291.8	0	16.0	16.0	0

The trend in the experimental data demonstrates that the maximum blocked force of a bundle increases with the number of active miniature PAMs in the bundle. However, this trend is not linear; a bundle of eight miniature PAMs does not produce double the force of a bundle of four miniature PAMs, which in turn does not produce double the force of a bundle of two miniature PAMs. The authors believe that under ideal conditions, with perfectly identical miniature PAMs, blocked force would increase linearly with the number of miniature PAMs. However, differences in miniature PAM characteristics, such as active length, result in performance losses.

The percent free contraction is determined by assuming that the bundle of miniature PAMs is initially constrained to the length of the shortest miniature PAM in the bundle. For the case considered here, the free contraction and percent free contraction

appear to be relatively constant as the number of miniature PAMs is increased, although lower than the free contraction for a single miniature PAM. However, when the inactive miniature PAMs are included in the bundle, the free contraction and percent free contraction appear to increase as the number of active PAMs increases (the number of inactive PAMs decreases). This likely occurs because the unpressurized, inactive PAMs will provide some resistance when compressed, causing the bundle to reach its free contraction state (at which it produces zero total force) sooner. Additionally, there is a slight loss in the maximum blocked force when inactive miniature PAMs are included in the bundle. These losses in force output and free contraction can be seen in Fig. 2.7 and are a function of the number of active and inactive miniature PAMs included in the bundle, as well as the operating pressure and percent contraction.

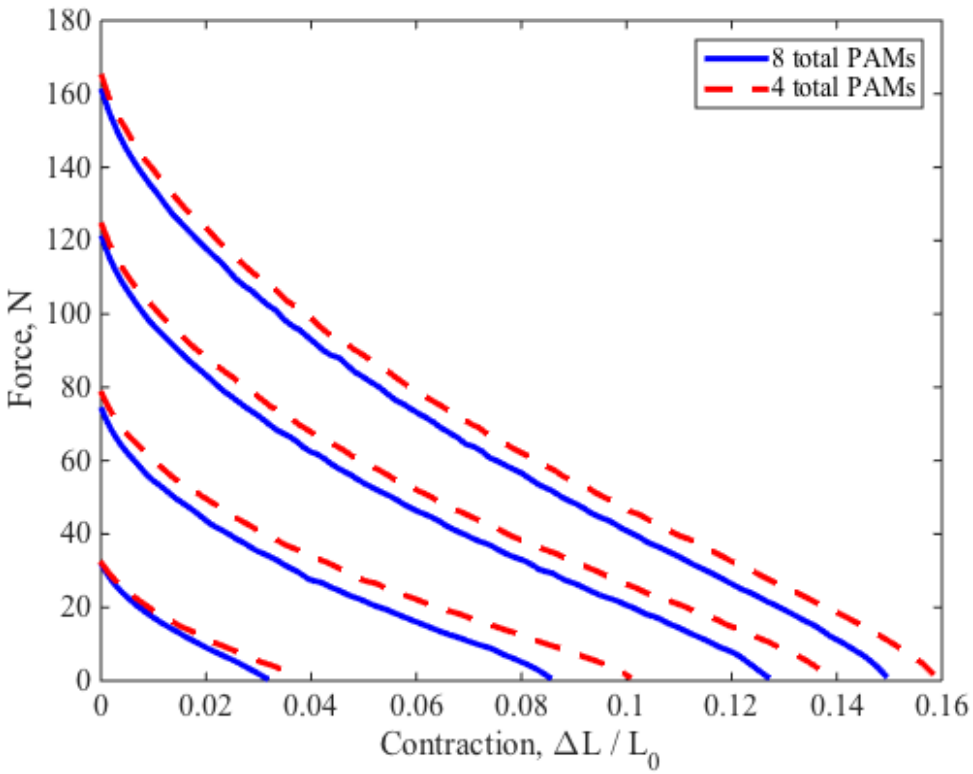

Figure 2.7: Force versus contraction for bundles of eight total or four total miniature PAMs with four active PAMs.

Figure 2.8 demonstrates the efficiency benefits of using the fewest number of miniature PAMs necessary to achieve a desired force production or contraction. The blocked force and free contraction values are maximized when the fewest number of miniature PAMs are operated at full pressure. The initial radial elasticity of the bladder for each active miniature PAM must be overcome. The total energy necessary to overcome this elasticity is a smaller portion of the total input energy at higher operating pressures.

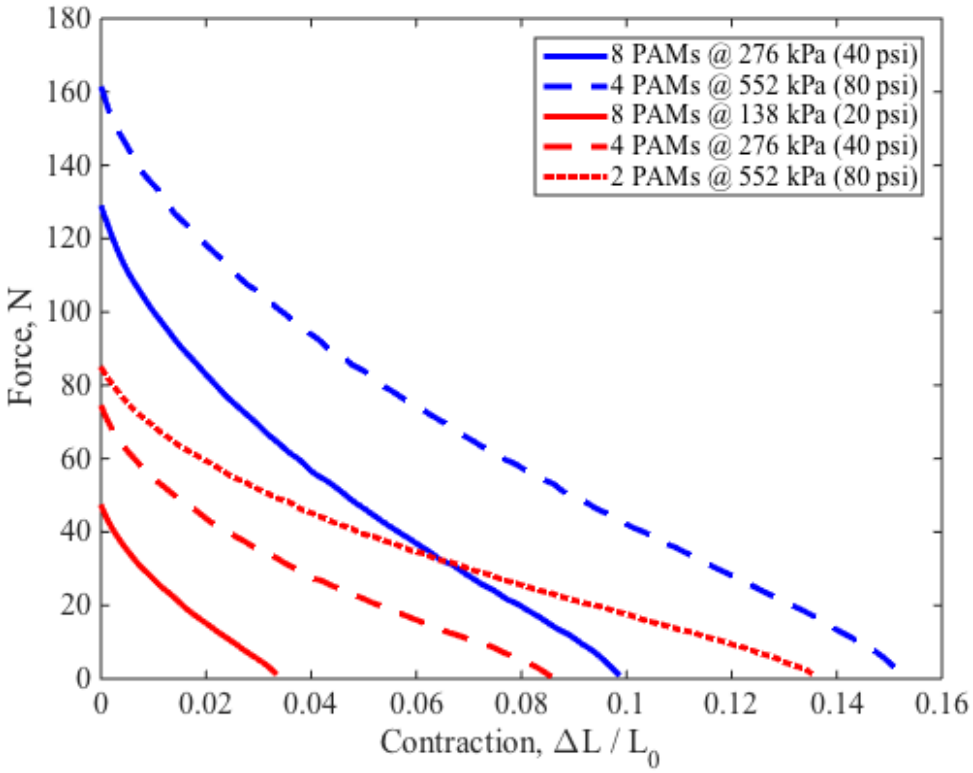

Figure 2.8: In a bundle of eight total miniature PAMs, the performance of four miniature PAMs actuated at full-pressure is plotted against the performance of eight at half-pressure, and the performance of two miniature PAMs actuated at full-pressure is plotted against the performances of four at half-pressure and eight at quarter-pressure.

2.3. Modeling

2.3.1. Modeling of Individual Miniature PAMs

Tondu (2012) provides a review of the models developed to predict the force generation and contraction behavior of PAMs. The miniature PAMs used in this study were modeled using a force balance approach (Kothera *et al.* 2009). A nonlinear stress-strain relationship was assumed for the bladder material (Hocking and Wereley 2013), and this relationship was constrained to have a linear variation in pressure (Pillsbury *et al.* 2015). Only the first and third polynomials in a third-order nonlinear stress-strain relationship were needed achieve sufficient model accuracy to predict the actuation behavior of the miniature PAMs used in this study.

The Gaylord force term, F_G, describes the force generated by a pressurized PAM:

$$F_G = \frac{P}{4\pi N^2}(3L^2 - B^2) \tag{2.1}$$

where P is the actuation pressure, L is the instantaneous actuator length (determined by subtracting the contraction length, ΔL, from the initial length, L_0), B is the length of one fiber in the braid, and N is the number of turns one fiber makes around the bladder. B and N are determined as a function of the braid angle, α, and the outer diameter of the bladder, D:

$$B = \frac{L}{\sin\alpha} \tag{2.2}$$

$$N = \frac{B\cos\alpha}{\pi D}. \tag{2.3}$$

The force balance model improved upon the Gaylord force model by including additional terms to account for bladder elasticity. The total force, F, generated by a PAM is calculated using:

$$F = \frac{P}{4\pi N^2}(3L^2 - B^2) + P\left(\frac{V_B}{L} - \frac{tL^2}{2\pi RN^2}\right) + \sigma_z \frac{V_B}{L} - \sigma_x \frac{tL^2}{2\pi RN^2} \qquad (2.4)$$

where σ_z is the axial stress in the bladder, σ_c the circumferential stress in the bladder, R and t are the instantaneous outer radius and thickness of the bladder, and V_B is the bladder volume, which is assumed to be constant. The first term is equivalent to the Gaylord force term and the second accounts for the non-constant bladder thickness (Kothera *et al.* 2009).

There is a pressure deadband that occurs before the minimum pressure is reached to overcome the initial radial elasticity of a bladder. At this pressure, the miniature PAM begins to contract. To account for the pressure deadband, a corrected actuation pressure, P', is used in the force balance model in place of the actual actuation pressure, P:

$$P' = P - P_{DB} \qquad (2.5)$$

where P_{DB} is the experimentally determined deadband pressure at which the PAM begins to contract.

Additionally, a corrected length, L', is used in place of the real actuator length, L. The corrected length is:

$$L' = L - 2\Delta L \qquad (2.6)$$

where ΔL is a length reduction term to reflect the rounded, non-cylindrical shape of the bladder near the two end fittings (Woods *et al.* 2011).

The length reduction term is found using:

$$\Delta L = \left(\frac{\pi}{2} - 1\right)(R - R_0). \tag{2.7}$$

where R_0 is the initial outer radius of the bladder.

Hocking and Wereley (2013) assumed the bladder material was a strain stiffening nonlinear elastic material to better predict the actuator performance. The axial and circumferential stresses are a polynomial function of the strain:

$$\sigma = \sum_{k=1}^{n} E_k(P)\varepsilon^k \tag{2.8}$$

where n is the model order of the material (chosen by the authors), E_k are the modulus values (optimized to minimize the error between the model and the experimental data), and ε_z and ε_c are the axial and circumferential strain in the bladder:

$$\epsilon_z = \frac{L}{L_0} - 1 \tag{2.9}$$

$$\epsilon_c = \frac{R - \frac{t}{2}}{R_0 - \frac{t_0}{2}} - 1. \tag{2.10}$$

Pillsbury *et al.* (2015) constrained the modulus values, E_k to be linear functions of pressure, so the nonlinear stress-strain relationship is:

$$\sigma = \sum_{k=1}^{n} (E_{kI} + E_{kS}P)\varepsilon^k \tag{2.11}$$

where E_{kI} and E_{kS} are the non-negative intercept and slope of $E_k(P)$ respectively. This assumption of linearity facilitates the use of interpolation to predict actuator performance at new operating pressures.

The optimization technique used to select the modulus values minimized the following error:

$$\Delta = \frac{1}{N_P}\sum_{k}\sqrt{\frac{1}{N_i}\sum_{i}[(F)_{ki} - (F_{AVG})_{ki}]^2} \tag{2.12}$$

where Δ is the average error across each test pressure, F is the force predicted by the model, F_{AVG} is the average experimental force, N_p is the number of test pressures, and N_i is the number of data points considered at each test pressure.

For the miniature PAMs used in this study, the errors were assessed for first-order through fifth-order polynomials. However, the error was sufficiently minimized using only the first and third modulus values in a third-order polynomial. The final stress-strain relationship used for this study was therefore:

$$\sigma = (E_{1I} + E_{1S}P)\epsilon^1 + (E_{3I} + E_{3S}P)\epsilon^3. \tag{2.13}$$

Incorporating the above modifications to the pressure and length terms, with the assumed nonlinear stress-strain relationship with a linear variation in pressure, the final model used for this study was:

$$F = \frac{P'}{4\pi N^2}(3L^2 - B^2) + P'\left(\frac{V_B}{L'} - \frac{tL^2}{2\pi RN^2}\right) + \sigma_z\frac{V_B}{L'} - \sigma_c\frac{tL'^2}{2\pi RN^2}. \tag{2.14}$$

Using the above modeling and optimization process, an individual model was generated for each of the eight miniature PAMs used in the study. The model is plotted versus the average force data for a single miniature PAM in Fig. 2.9. As previously noted, it is most efficient to operate PAMs at higher operating pressures. Thus, the model was only optimized over the 276 kPa (40 psi) to 621 kPa (90 psi) pressure curves to allow the model to most accurately reflect the experimental data in the desired range of operating pressures. Due to the limitations of the model, some accuracy had to be

sacrificed at the blocked force and free contraction states to allow the model to best predict the performance over the majority of the contractile range.

In addition to optimizing the strain modulus values, the optimization code was also used to more precisely predict the braid angle for each of the miniature PAMs used in the study. Although the braid angle of the miniature PAMs was assumed to be a nominal value of 59° based on visual inspection, it is difficult to accurately measure braid angle. The braid angle can vary slightly between miniature PAMs due to inconsistencies in the fabrication process. The braid angles predicted for each miniature PAM during the optimization process are provided in Table 2.3. The average braid angle predicted with the code was 58.81° with a small standard deviation of 0.39°.

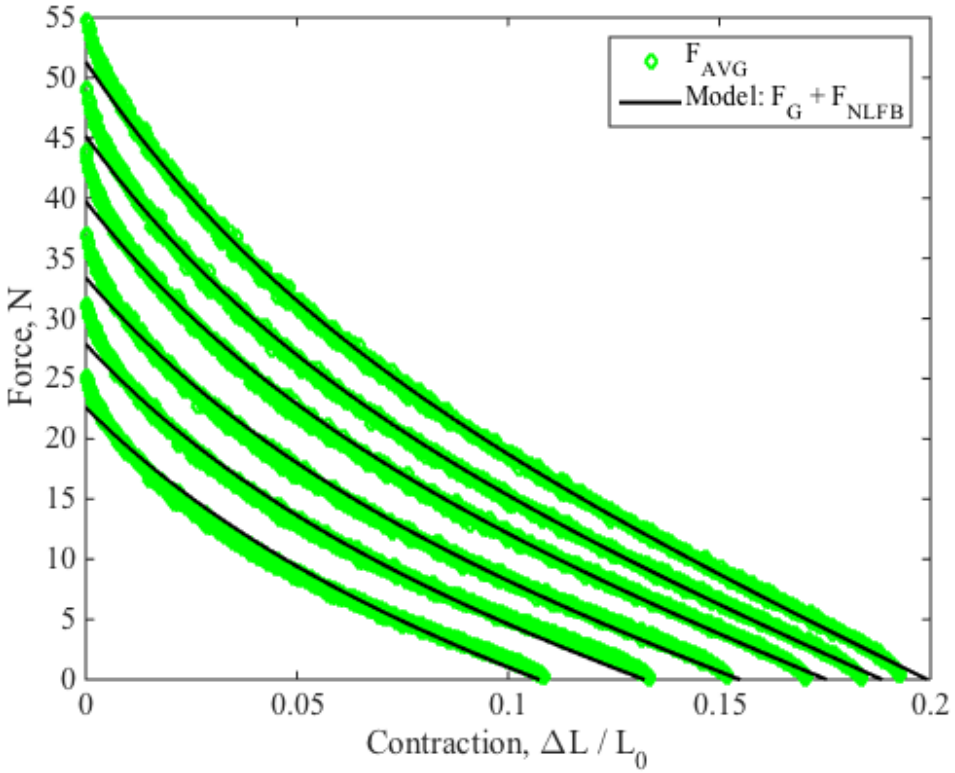

Figure 2.9: Model of actuation behavior of miniature PAMs: the Gaylord Force (F_G) plus the Nonlinear Force Balance Model (F_{NLFB}) plotted versus the average experimental data (F_{AVG}).

Table 2.3: Braid angles of the miniature PAMs predicted through the model optimization process.

PAM No.	Predicted Braid Angle (°)
1	58.98
2	59.14
3	58.21
4	58.27
5	58.90
6	58.65
7	59.16
8	59.14
Avg.	58.81
Std. Dev.	0.39

2.3.2. Modeling of Miniature PAMs Bundles

As noted in Section 2.3, the force generated by a bundle of miniature PAMs is not a direct linear function of the number of miniature PAMs in the bundle. Bryant *et al.* (2014) made a similar observation: the total force generated by their six FAMs actuating in unison was less than the total sum of the force generated by each FAM actuated individually. They suggested that this force loss was a result of interaction between the actuators. However, the same force loss was observed in this study, where the miniature PAMs were spaced sufficiently apart to prevent the individual actuators from coming in contact with one another. Thus, an alternate explanation for the force reduction, other than friction between the actuators resisting radial expansion, is necessary.

The losses in force in the bundle of miniature PAMs considered this study can be predicted by accounting for the differences in active lengths of the miniature PAMs included in the bundle. When the miniature PAMs in a bundle are constrained together and operated in unison, they are held at an equal length. Due to the high antagonistic forces associated with PAMs, a bundle will likely rest at the length of the shortest

miniature PAM in the bundle. Thus, each of the longer miniature PAMs would start at a non-zero initial percent contraction. Because there is a direct correlation between force generation and percent contraction of individual miniature PAMs, this initial percent contraction would result in a loss in the total blocked force of the bundle.

As noted in Table 2.1, the active lengths of the miniature PAMs considered in this study range from 6.63 cm (2.61 in) to 7.06 cm (2.78 in). If each of the miniature PAMs in a bundle of eight miniature PAMs were held at the length of the shortest miniature PAM, then the longest miniature PAM would begin at an initial percent contraction of 6.1%. For the corresponding miniature PAM, pressurized to 552 kPa (80 psi), this corresponds to approximately a 22.2 N (5.0 lb) loss in the blocked force. Each of the other miniature PAMs would have its own corresponding initial percent contraction and blocked force reduction based on their relative resting lengths.

Using this methodology, a model was developed to predict the actuation behavior of a bundle of miniature PAMs:

$$F_{bundle} = \sum_{i=1}^{m} F_i\left(\left(\frac{\Delta L}{L}\right)_i\right) \tag{2.15}$$

where F_{bundle} is the predicted force output of the bundle, m is the number of miniature PAMs in the bundle, and F_i is the predicted force output of the specified individual miniature PAM. The predicted force output of an individual miniature PAMs is constrained to be non-negative and is a function of the percent contraction of the specified PAM from its corresponding active length, $(\Delta L/L)_i$, found using:

$$\left(\frac{\Delta L}{L}\right)_i = \frac{\left(L_{0i} - L_{0,min}\right) + \left(L_{0,min} - L\right)}{L_{0i}} = \frac{L_{0i} - L}{L_{0i}} \tag{2.16}$$

where L_{0i} is the active length of the specified miniature PAM, $L_{0,min}$ is the shortest active length in the bundle, and L is the current length of the bundle. The quantity $(L_{0i} - L_{0,min})$ is the initial contraction of the specified miniature PAM to the resting length of the bundle, assumed to be the resting length of the shortest miniature PAM in the bundle, and $(L_{0,min} - L)$ is the contraction of the bundle from this assumed resting length.

The proposed model is highly dependent on both the actuation behavior of the individual miniature PAMs included in the bundle, and the variation in active lengths of the miniature PAMs. Effectively, the force versus displacement curve for each individual miniature PAM included in a bundle is shifted along the contraction axis by its initial contraction, and then the resulting shifted curves are summed together to predict the total actuation behavior of the bundle.

This shifting and summation modeling process to predict the actuation performance of miniature PAM bundles is demonstrated for a bundle of two miniature PAMs operated at 552 kPa (80 psi) in Fig. 2.10. In this plot, the force versus contraction curve for the longer miniature PAM (PAM 6, blue line) is shifted along the x-axis by its initial contraction to its shifted position (PAM 6s, blue dashed line). Here, the bundle active length is assumed to be the length of the No. 8 miniature PAM (6.68 cm), so the No. 6 miniature PAM (6.86 cm) has an initial contraction of 0.18 cm. The shifted curve is then added to the curve for the shortest miniature PAM (PAM 8, red line) to achieve the corrected model curve (PAM 6s + PAM 8, black line). Because the model is generated from the individual miniature PAM models, it is also sensitive to variations in other parameters, such as braid angle.

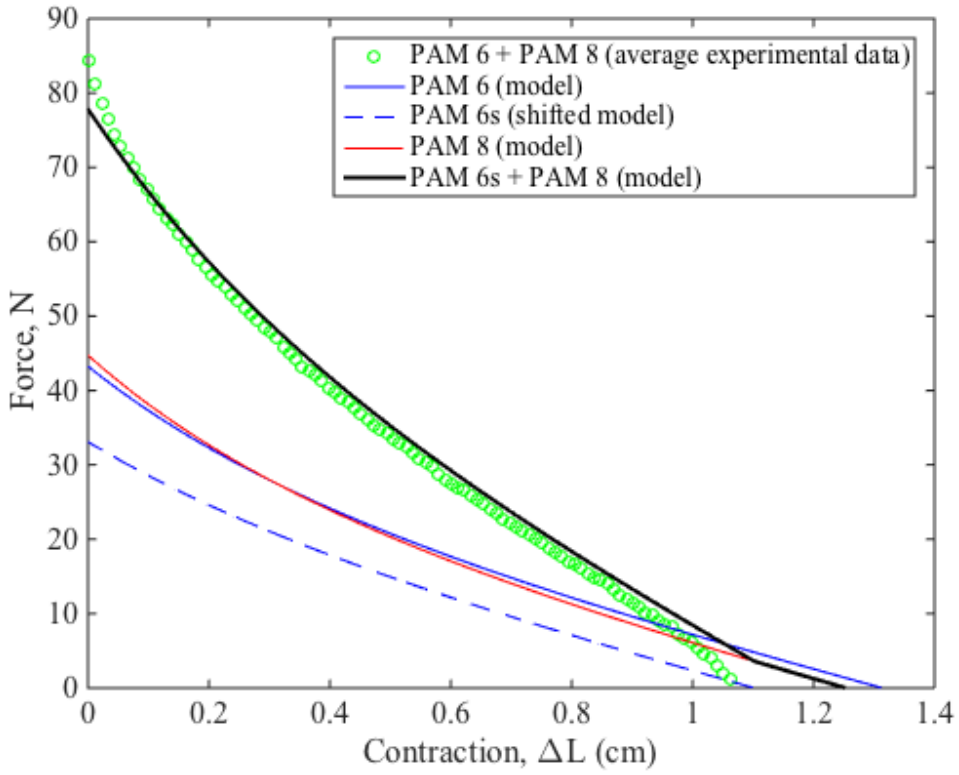

Figure 2.10: Demonstration of miniature PAM bundle modeling process.

The results of the modeling process can be seen in Fig. 2.11, where the values predicted by this corrected model are plotted against the average data from the experimental characterization. The model does not take into account the effect of the inactive miniature PAMs included in a bundle, so the results are compared to the experimental data with the inactive miniature PAMs ex-situ. Also plotted is the ideal model, which is the expected actuation behavior of the bundle if each miniature PAM had an identical resting length. This model is a simple summation of the actuation curves of each individual miniature PAM, without the application of any shifts to account for the variation in resting lengths of the miniature PAMs. The ideal model is also analogous to a bundle where each miniature PAM is precisely shimmed to have the same actuator

length, allowing the blocked force of the bundle to be equivalent to the sum of the blocked forces of each of the individual miniature PAMs.

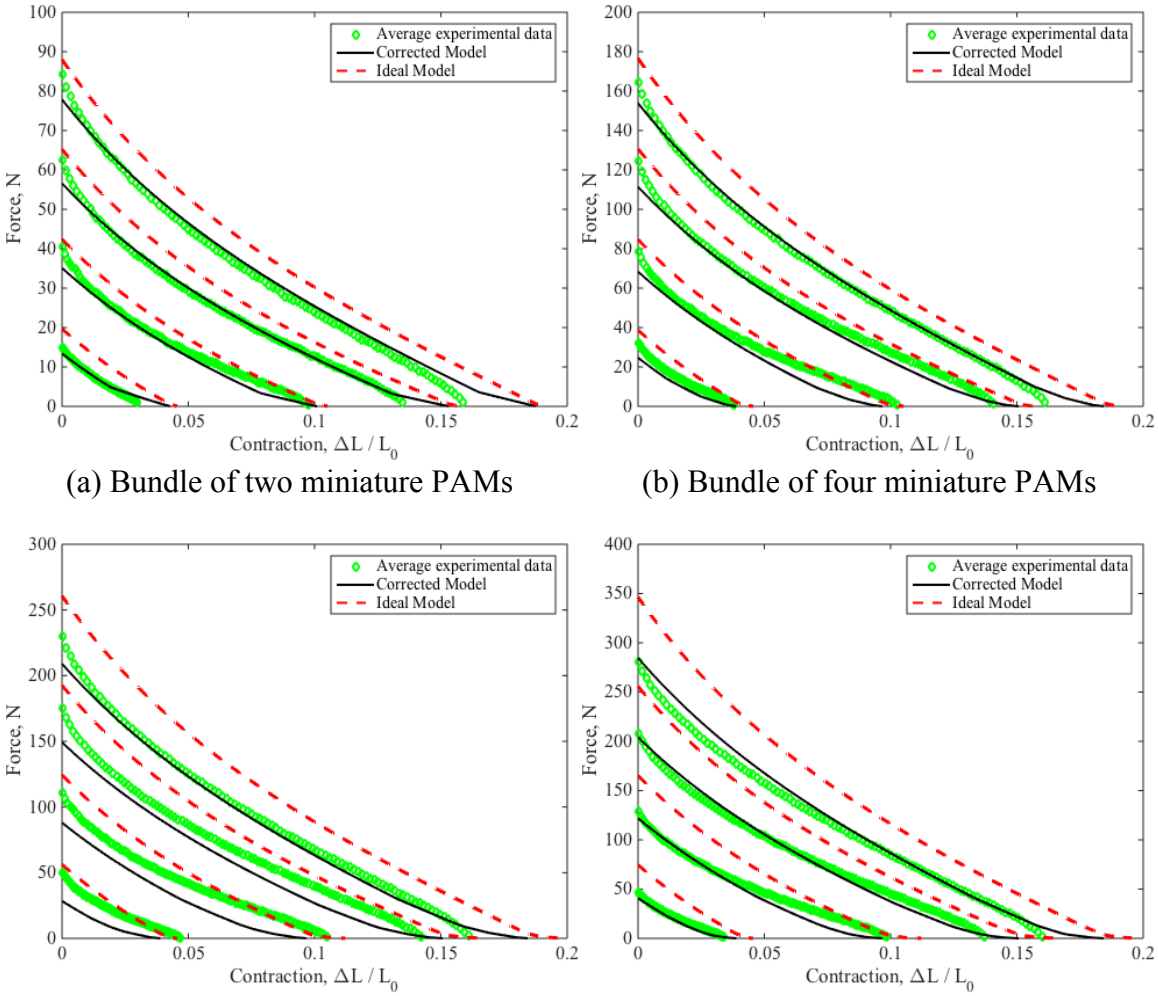

(a) Bundle of two miniature PAMs (b) Bundle of four miniature PAMs

(c) Bundle of six miniature PAMs (d) Bundle of eight miniature PAMs

Figure 2.11: Corrected and ideal models of actuation behavior of a bundle of miniature PAMs plotted versus the average experimental data.

For each bundle of miniature PAMs (with two, four, six, and eight total PAMs), the average percent errors for both the corrected and ideal models were calculated for each of the actuation pressures (138, 276, 414, 552 kPa), using:

$$\%error = \frac{1}{N_i}\sum_{i=1}^{N_i}\left|\frac{(F_{AVG})_i - (F)_i}{F_B}\right| \tag{2.17}$$

where N_i is the total number of data points compared, $(F_{AVG})_i$ is the average experimental force value at each percent contraction value compared, $(F)_i$ is the predicted force value at each percent contraction value compared, and F_B is the blocked force value at zero contraction from the experimental data along the corresponding pressure curve. The percent error was determined over the range of percent contraction for the corresponding experimental data.

The average percent errors for the corrected and ideal models can be seen in Table 2.4. The errors for the corrected and ideal models for a single miniature PAM are the same. The ideal model percent errors are large, justifying the need to develop a better model to predict the actuator performance. As seen in Fig. 2.11, the models tend to be least accurate at predicting behavior in the blocked force and free contraction regions. The highest model errors occur tend to occur at 138 kPa (20 psi), which is likely due to two factors: (1) the individual miniature PAM models were developed through optimization in only the 276-621 kPa (40-90 psi) region, and (2) the blocked force term in the denominator of the percent error calculation is smaller at lower pressures. The authors believe that the higher model error for the bundle with six miniature PAMs is likely due to a slight imbalance in the cruciform structure holding the bundle together.

For this study, the actuation behavior of each miniature PAM was optimized and predicted individually. If the same optimization parameters were applied to each miniature PAM, the resulting percent errors of the updated bundle model are presented in Table 2.5. This data is generated assuming that the No. 8 miniature PAM is optimized, those optimization parameters are applied to the seven other miniature PAMs, and the individual models are still shifted to account for the variation in resting lengths of the

miniature PAMs. The percent errors would vary somewhat if a different miniature PAM was used for the optimization. The updated percent errors are comparable to those in Table 2.4. The results indicate that small errors in the individual models minimally affect the error of the bundle model as a whole. Thus, when it is inconvenient to individually characterize all miniature PAMs in larger bundles, reasonable results can likely be achieved by characterizing a single PAM and applying the same optimization parameters to each PAM in the bundle. It would still be necessary to measure the active length of each individual miniature PAM for the corrected bundle model.

Table 2.4: Average percent errors for models of actuation behavior of miniature PAM bundles.

No. of PAMs	Pressure (kPa)	Ideal Model Avg. % Error (%)	Corrected Model Avg. % Error (%)
1	138	2.8	2.8
	276	3.1	3.1
	414	1.3	1.3
	552	0.7	0.7
2	138	34.7	3.0
	276	7.8	3.7
	414	8.3	1.0
	552	8.4	2.0
4	138	18.7	11.6
	276	7.1	6.5
	414	6.2	2.7
	552	8.4	0.8
6	138	9.5	22.9
	276	8.0	11.9
	414	8.3	6.1
	552	11.4	1.8
8	138	44.9	6.8
	276	15.8	5.0
	414	14.2	2.6
	552	14.8	2.3

Table 2.5: Difference in average percent errors for the corrected model of actuation behavior of miniature PAM bundles when each miniature PAM is individually optimized versus not individually optimized.

No. of PAMs	Pressure (kPa)	Avg. % Error—Individual Opt. (%)	Avg. % Error—Single Opt. (%)	Difference (%)
1	138	2.8	2.8	0
	276	3.1	3.1	0
	414	1.3	1.3	0
	552	0.7	0.7	0
2	138	3.0	4.6	-1.6
	276	3.7	4.7	-1.0
	414	1.0	1.4	-0.4
	552	2.0	1.1	0.9
4	138	11.6	9.5	2.1
	276	6.5	6.2	0.3
	414	2.7	2.8	-0.1
	552	0.8	0.8	0
6	138	22.9	21.7	1.2
	276	11.9	12.0	-0.1
	414	6.1	6.6	-0.5
	552	1.8	2.1	-0.3
8	138	6.8	3.6	3.2
	276	5.0	4.6	0.4
	414	2.6	2.7	-0.1
	552	2.3	2.8	-0.5

The average losses and percent losses in force predicted by the corrected model from those values predicted by the ideal model are provided in Table 2.6. This table provides information on the losses experienced at each pressure and for each number of active miniature PAMs due to the variation in active lengths of the bundle. The average loss and percent loss increase as the number of miniature PAMs increases, due to the additional variation in active lengths. The table also shows the possible gains in force production that could result from improvements in the fabrication process facilitating the

production of more similar miniature PAMs. The loss and percent loss are calculated as follows:

$$loss = \frac{1}{N_i}\sum_{i=1}^{N_i}|(F_I)_i - (F)_i| \tag{2.18}$$

$$\%loss = \frac{1}{N_i}\sum_{i=1}^{N_i}\left|\frac{(F_I)_i - (F)_i}{F_{I,B}}\right| \tag{2.19}$$

where N_i is the total number of data points compared, $(F)_i$ and $(F_I)_i$ are the predicted force values from the corrected and ideal models respectively at each percent contraction value compared, and $F_{I,B}$ is the blocked force value at zero contraction from the ideal model along the corresponding pressure curve.

Table 2.6: Average loss and percent loss from the ideal model to the corrected model.

No. of PAMs	Pressure (kPa)	Average Loss (N)	Average % Loss (%)
2	138	3.8	19.4
	276	4.3	10.2
	414	4.7	7.2
	552	5.3	6.0
4	138	8.3	21.3
	276	9.5	11.2
	414	10.2	7.8
	552	11.5	6.5
6	138	15.2	27.0
	276	19.4	15.6
	414	22.0	11.4
	552	25.8	9.9
8	138	19.0	25.5
	276	23.2	14.1
	414	26.1	10.2
	552	30.6	8.8

Using the same modeling technique described above, an identical model was generated for a bundle assuming the use of eight perfectly identical miniature PAMs.

Then, a variation was introduced into the bundle by increasing the length of a set number of miniature PAMs by a specified percent. The percent force losses of models with a range of introduced percent variations in length from the identical model are provided in Table 2.7. The lower bound on the percent loss was calculated by only varying (increasing) the length of one of the eight miniature PAMs, while the upper bound was calculated by varying the length of seven of the eight miniature PAMs. This bundle model was generated using the optimization parameters and active length of the No. 8 miniature PAM from Table 2.1. The results highlight the desire to minimize the length variations in miniature PAMs included in bundles to reduce the resulting force losses, and indicate that the percent losses are less significant at higher operating pressures.

Table 2.7: Range of average percent losses in force generation from the identical bundle actuator performance corresponding to specified variations in the resting lengths in the bundle for bundles of 8 PAMs.

Pressure (kPa)	% loss for 0.5% variation in resting length (%)	% loss for 1% variation in resting length (%)	% loss for 2.5% variation in resting length (%)	% loss for 5% variation in resting length (%)
138	1.3 – 9.3	2.5 – 17.7	4.8 – 33.7	5.6 – 39.6
276	0.6 – 4.1	1.2 – 8.1	2.5 – 17.6	4.1 – 28.6
414	0.4 – 2.7	0.8 – 5.4	1.7 – 12.2	3.0 – 21.1
552	0.3 – 2.2	0.6 – 4.5	1.4 – 10.2	2.6 – 18.0

The proposed model has only been applied to the bundle of miniature PAMs presented in this study. The authors believe that the model should extend to other bundles of PAMs; however, the effects would likely be less significant in full-scale PAMs. In bundles of longer PAMs, the variations in active lengths due to inconsistencies in the fabrication process would correspond to smaller initial percent contractions, and therefore proportionately less significant losses in blocked force.

2.4. Efficiency

The mechanical work output for each bundle, $W_{out,bundle}$, was calculated using:

$$W_{out,bundle} = \int_0^{\Delta L} F_{bundle} dx \tag{2.20}$$

where F_{bundle} is the force output of the bundle and x is the contraction distance of the bundle, $L_0 - L$.

The initial energy, $E_{initital}$, in an unpressurized miniature PAM is:

$$E_{initial} = P_0 V_0 \tag{2.21}$$

where P_0 is the atmospheric pressure and V_0 is the initial internal bladder volume.

The final energy, E_{final}, in a pressurized miniature PAM is:

$$E_{final} = (P_0 + \Delta P)(V_0 + \Delta V) \tag{2.22}$$

where ΔP is the change in pressure to achieve the final pressurized state and ΔV is the experimentally measured change in volume that occurs when a pressurized bundle expands from its blocked force state to its free contraction state.

The input energy, E_{in}, needed to pressurize a miniature PAM is:

$$E_{in} = E_{final} - E_{initial} = P_0 \Delta V + \Delta P V_0 + \Delta P \Delta V. \tag{2.23}$$

Although the volume and volume change of each individual miniature PAM will be slightly different due to the variation in active lengths, for the purpose of approximating the input energy to a pressurized bundle, each miniature PAM is assumed to have the active length of the shortest miniature PAM in the bundle. The input energy to a pressurized miniature PAM bundle is then assumed to be:

$$E_{in,bundle} = mE_{in} \tag{2.24}$$

where m is the total number of miniature PAMs in the bundle.

The efficiency of the bundle is:

$$\eta = \frac{W_{out,bundle}}{E_{in,bundle}} = \frac{\int_0^{\Delta L} F_{bundle} dx}{m(P_0 \Delta V + \Delta P V_0 + \Delta P \Delta V)}. \quad (2.25)$$

Using this efficiency model, the estimated efficiencies of bundles of miniature PAMs are provided in Table 2.8. The corrected and ideal model efficiencies are calculated using the corrected and ideal models for the actuation behavior of the bundles. Both models use the same method to predict the input energy as described above. The table reveals a significant increase in efficiency at higher operating pressures for both the corrected and ideal model efficiencies. The corrected model experiences a drop-off in efficiency as more miniature PAMs are added to the bundle as a result of the loss in the total work due to the variation in the resting lengths of the PAMs in the bundles. While the ideal model efficiencies also fluctuate slightly as the number of miniature PAMs in the bundle is changed, this variation is due to the slight difference in the actuation behavior for the individual PAMs, rather than a loss in total work due to resting length variations. For an identical model, which predicts the performance of a bundle with perfectly identical miniature PAMs, the efficiencies would all be equivalent to the efficiency of a single miniature PAM (11.6%, 23.0%, 32.0%, and 39.3% for 138, 276, 414, and 552 kPa respectively for PAM No. 8), because there would theoretically be an exact linear increase in both work out and energy in for the bundle as additional miniature PAMs are added.

Table 2.8: Predicted corrected and ideal model efficiencies.

No. of PAMs	Pressure (kPa)	Corrected Model Efficiency (%)	Ideal Model Efficiency (%)
1	138	11.6	11.6
	276	23.0	23.0
	414	32.0	32.0
	552	39.3	39.3
2	138	6.8	12.0
	276	17.6	23.3
	414	26.4	32.1
	552	33.5	39.3
4	138	5.6	11.2
	276	16.4	22.7
	414	25.5	31.8
	552	32.3	38.9
6	138	4.1	11.0
	276	13.5	22.6
	414	22.1	31.6
	552	28.6	38.6
8	138	4.4	10.9
	276	14.1	22.3
	414	22.7	31.2
	552	29.2	38.1

Figure 2.12 shows the predicted efficiency trends for using a bundle of miniature PAMs to lift a payload to a fixed height. The plots were generated using the bundle models to find the force generation at the given height corresponding to each number of miniature PAMs at each operating pressure. This force value was assumed to be the payload weight that could be lifted to the specified height and was plotted versus the efficiency for the corresponding number of miniature PAMs and operating pressure, using the data from Table 2.8. The black line in the figures indicates the maximum achievable efficiency as the payload weight increases. This trend highlights the benefits of operating the fewest number of miniature PAMs at the highest pressure (corresponding to the highest efficiency) to achieve the desired results (lifting a specified payload to a

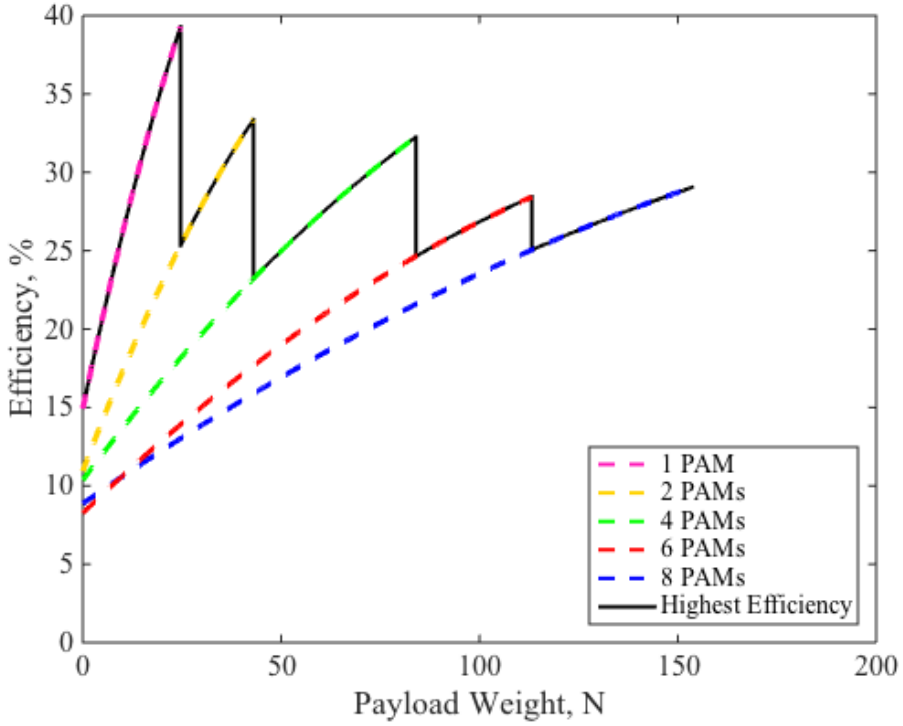

(a) Corrected model

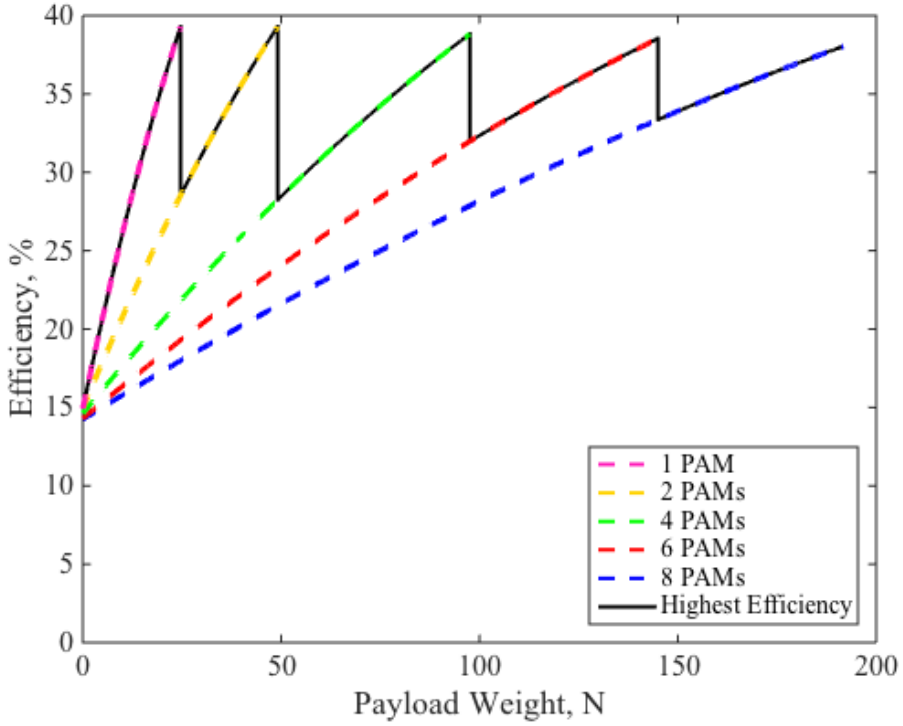

(b) Ideal model

Figure 2.12: Maximum efficiency for using a bundle of miniature PAMs to lift a weight to a specified height of 0.38 cm (0.15 in).

specified height) with the best performance. Figure 2.12a uses the corrected model data and gives a more realistic prediction of the operating efficiency due to the losses in the operation of the bundle, which correspond to a drop off in efficiency as more miniature PAMs are recruited. Figure 2.12b corresponds to the ideal model data and gives an indication of the achievable performance, with improvements to both force generation and efficiency, as improvements to the fabrication process facilitate the development of increasingly similar miniature PAMs.

2.5. Conclusions

In this study, the actuator performance of a bundle of miniature PAMs was experimentally characterized, modeled, and assessed. The analysis was used to better understand the behavior of miniature PAM bundles and to predict the potential efficiency gains achievable through the application of a variable recruitment control strategy to a bundle to mimic the selective recruitment of motor units in human muscles. The main contributions of this study are the following:

(1) The experimental characterization of a bundle of miniature PAMs demonstrated the quasi-static actuation behavior of the bundle. The data revealed a nonlinear increase in force as the number miniature PAMs increased, as well as a slight loss in force generation due to inactive miniature PAMs in the bundles. The results also highlighted the performance benefits of operating the fewest number of miniature PAMs at their highest operating pressure.

(2) A model was proposed to predict the agonistic force generation and contraction behavior of a bundle of miniature PAMs by accounting for the length and performance variations in the individual miniature PAMs included in the bundles.

The proposed model was able to better predict the actuation behavior of the miniature PAM bundles than a simple summation of the individual miniature PAM actuation behaviors, providing a significant improvement in the model accuracy.

(3) The efficiency benefits of applying a variable recruitment control technique to a bundle of miniature PAMs were predicted using the output mechanical work from the models, as well as the estimated input energy at each operating pressure. The results indicated that although there is the slight loss in system efficiency as more variation was introduced into bundles through the addition of new miniature PAMs, this loss was outweighed by the benefits of operating the fewest number of miniature PAMs in more optimal pressure ranges.

(4) The need to minimize the physical variations in the miniature PAMs included in bundles, through enhancements to the accuracy and precision of the miniature PAM fabrication process, was demonstrated. Small reductions in the length variation within a bundle can provide significant improvements in bundle force production and efficiency.

In conclusion, the study indicated that, despite some losses in force production and contraction performance of miniature PAM bundles, there would be clear benefits to applying a variable recruitment control strategy to a bundle of miniature PAMs to allow an actuator to most efficiently perform tasks requiring wider ranges of force production. Future work should include improving the fabrication process for miniature PAMs to reduce the efficiency loses due to resting length variations, or developing a shimming process to effectively match the actuator length of each miniature PAM in a bundle.

3. Antagonistic Pair of Bundles of Miniature Pneumatic Artificial Muscles

3.1. Introduction

Human muscles operate as agonist, synergist, or antagonist muscles. When activated, agonist muscles contract and generate a pulling force to perform a desired motion, such as flexion or extension about a joint. Synergist muscles assist agonist muscles at the onset of motion and help stabilize the motion about the joint. In response to the motion of the agonist muscles, the relaxed antagonist muscles extend and produce an opposing force. The body's nervous system controls the muscular forces to achieve controlled movements (Tözeren 2000). The same muscle group can operate as either an agonist or an antagonist muscle group depending on whether it is contracting or extending, with the range of motion dictated by human joints.

The biceps-triceps pair of muscles is one example of an antagonist muscle pair where the biceps produce the flexion movement about the elbow joint, while the triceps produce the corresponding extension movement. The quadriceps and hamstring are another example of an antagonist pair, producing the flexion and extension movements about the knee. Muscles generate pulling forces, but they cannot generate pushing forces. Therefore, an antagonist muscle pair is needed to produce bidirectional motion about human joints.

Like human muscles, PAMs are unidirectional actuators that can only generate pulling forces in the axial direction. When pressurized, PAMs expand radially and contract axially, generating an axial pulling force proportionate to their level of

contraction. PAMs generate their maximum force when held at their resting state, and zero force after being allowed to fully contract to their actuated state.

PAMs are designed to contract and generate axial forces, such as human muscles operating in the agonist role. However, PAMs can also serve in the role of the antagonist muscle. When operated as antagonist muscles, PAMs create opposing forces to resist stretching, proportionate to the amount they are stretched. As seen in Fig. 3.1, the resultant antagonist force increases substantially as a PAM is extended past its active length. Like agonist PAM forces, antagonist PAM forces also increase with pressure and experience hysteresis during their loading and unloading cycles (Vocke *et al.* 2014).

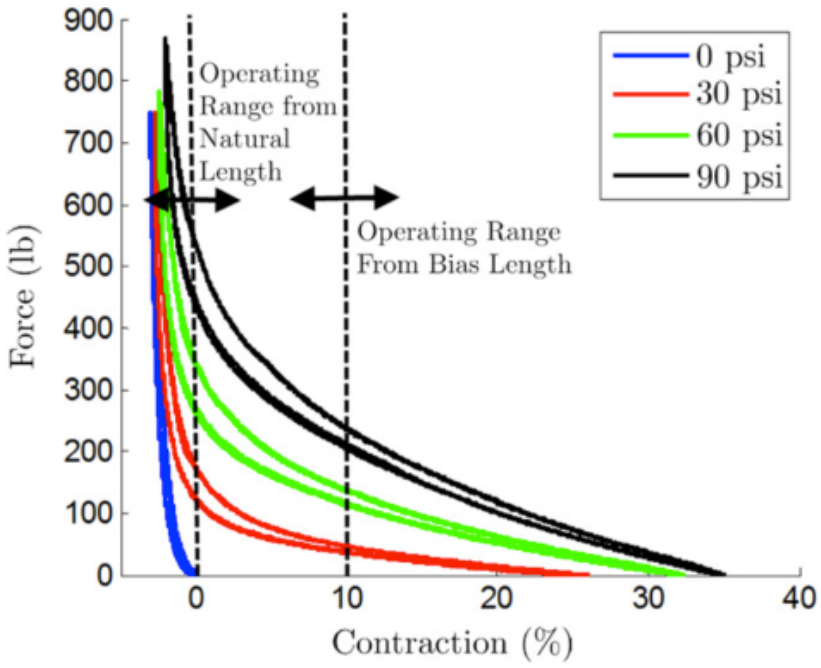

Figure 3.1: "A typical PAM force versus contraction curve, illustrating the typical operating range for an antagonistic actuator" (Vocke *et al.* 2014).

A unidirectional actuator must be operated in an agonist-antagonist configuration for applications requiring bidirectional motion, such as trailing edge flaps (Woods *et al.* 2011, Woods *et al.* 2014) and robotic arms (Tondu *et al.* 2005, Ariga *et al.* 2012). When

two PAMs are connected about a pivot point as an antagonistic pair, as depicted in Fig. 3.2, either PAM can be pressurized to act as the agonist muscle or relaxed to act as the antagonist muscle. This antagonistic pair configuration allows for bidirectional motion about the pivot point. The agonist and antagonist roles can be reversed based on the desired direction of rotation.

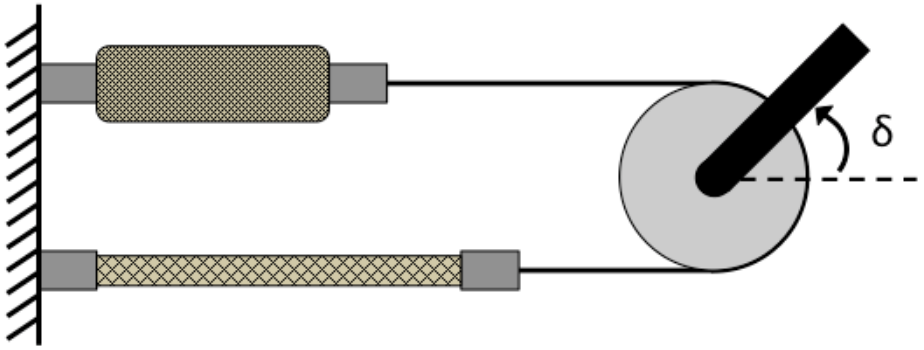

Figure 3.2: A simple bidirectional actuator with two PAMs in an agonist/antagonist configuration.

When two PAMs are operated in an antagonist pair, the antagonist PAM generates an opposing force to counter the force generated by agonist PAM. The achievable deflection and available work of the system when operated with an antagonist muscle pair is significantly limited due to the high passive stiffness of the antagonist PAM as it is stretched past its resting length. Two regularly implemented modifications to improve the system performance are the choice of a system geometry that decreases the passive torque and the introduction of a bias contraction (Vocke *et al.* 2014).

Modifications to the system geometry can be made by appropriate design selection of the mechanism through with PAMs generate the system deflection. Researchers have utilized pulleys (Tondu *et al.* 2005, Shin *et al.* 2009), variable radius pulleys (Shin *et al.* 2011), and offset levers or bell cranks (Woods *et al.* 2011, Vocke *et*

al. 2014). Vocke *et al.* (2012) considered a sliding moment arm in the form of a slotted-T mechanism to increase the difference between corresponding agonist and antagonist moment arms for a bidirectional actuator designed using miniature PAMs in an antagonistic pair configuration for the use on UAVs and other small-scale applications.

Another option for improving the achievable system deflection angle is to introduce a bias contraction and corresponding bias pressure. Researchers have used bias contractions to shift the resting state of the PAMs in the bidirectional actuator from their resting length to a pre-contracted length (Tondu and Lopez 1997, Tondu *et al.* 2005, Deaconescu and Deaconescu 2009). This shift allows a PAM to achieve a greater deflection in response to the overall system deflection before entering the range of the high passive stiffness, as indicated in Fig. 3.1. A bias pressure must be applied to the system to ensure hinge stiffness at the joint when there is a bias contraction. Bias pressure worsens actuator performance but is necessary for maintaining hinge stiffness. The ideal bias contraction and pressure must be chosen based on the specific system properties and performance requirements (Vocke *et al.* 2014).

3.2. Experimental Characterization and Modeling of Antagonistic Performance

3.2.1. Experimental Characterization of Antagonistic Behavior of Miniature Pneumatic Artificial Muscles and Muscle Bundles

A summary of the properties of the eight miniature PAMs used in this study are provided in Table 3.1. These are the same miniature PAMs presented in Table 2.1. Here, only the antagonist behavior of the miniature PAMs at zero pressure is considered. For

the following study, a bidirectional actuator system is considered without a bias contraction, so a bias pressure is not needed to maintain joint stiffness. The antagonist force will increase as pressure is increased. In an antagonist pair configuration, without a bias contraction, minimizing the antagonist force will maximize the total displacement angle of the system.

Table 3.1: Summary of properties of the individual miniature PAMs from experimental characterization.

PAM No.	Active Length (cm)	Braid Angle Predicted through Optimization (°)	Force at 2.5% Extension (N)	Force at 5% Extension (N)
1	7.06	58.98	5.3	24.7
2	6.73	59.14	9.8	41.1
3	6.78	58.21	6.8	28.3
4	6.68	58.27	10.3	42.7
5	6.73	58.90	9.1	39.8
6	6.86	58.65	7.8	34.3
7	6.63	59.16	10.2	43.5
8	6.68	59.14	11.2	48.2
Avg.	6.77	58.81	8.8	37.8
Std. Dev.	0.14	0.39	2.0	8.1

The process for characterizing the individual antagonist behavior of the individual miniature PAMs is similar to the characterization process for the agonist behavior of miniature PAMs, which was described in Section 2.2.2. Experimental characterization of the performance of each miniature PAM was completed through quasi-static testing using a 100 kN (22 kip) MTS servo-hydraulic test machine. Testing was used to evaluate the relationship between force and extension for the miniature PAMs. For this antagonist testing, the miniature PAMs remained unpressurized. Each miniature PAM was cycled three times in the MTS machine between its resting state and five percent extension.

The MTS machine recorded displacement data during the cycling. Force data was simultaneously collected through a Honeywell load cell (Model No. 31) rated for 445 N (100 lb). Pressurized air was supplied to the miniature PAMs by a Husky Pro 227 L (60 gal) air compressor, and the pressure was regulated with a Wilkerson Dial-Air pressure regulator (model No. R21-04-000) with an SSI Technologies, Inc. digital pressure gauge (Part No. MGA-300-A-9V-R).

A plot of the antagonist behavior in the zero to five percent extension range for each of the eight individual miniature PAMs used in this experiment is provided in Fig. 3.3. The resting length of each miniature PAM and its antagonist force at 2.5 and five percent extension is provided in Table 3.1. Each miniature PAM has a similar increasing trend for the force as the extension increases; however, there is some variation in the total force for each PAM at a given percent extension. At five percent extension, the antagonist forces range from 24.7 to 48.2 N (5.6 to 10.8 lb). The general trend in the data shows that the antagonist force at a given percent extension tends to be lower for longer miniature PAMs. The blue, light green, and yellow curves, corresponding to the three longest miniature PAMs (miniature PAM number one, six and three respectively), have the lowest total force values at each measured level of percent extension.

New end plates were designed to hold together the miniature PAMs for the antagonistic testing and characterization of the miniature PAM bundle behavior. The new design featured a flat square plate with a through hole in the center for screws to attach to testing apparatus and 8 symmetric holes around the edge of the plate. This new design minimizes the bundle volume to fit into an antagonist pair testing apparatus, while still maintaining a half-inch spacing between the centers of adjacent miniature PAMs to allow

for sufficient room for radial expansion during pressurization. An assembled bundle can be seen in Fig. 3.4. The same testing procedure was repeated for the bundle as was completed for each individual miniature PAM.

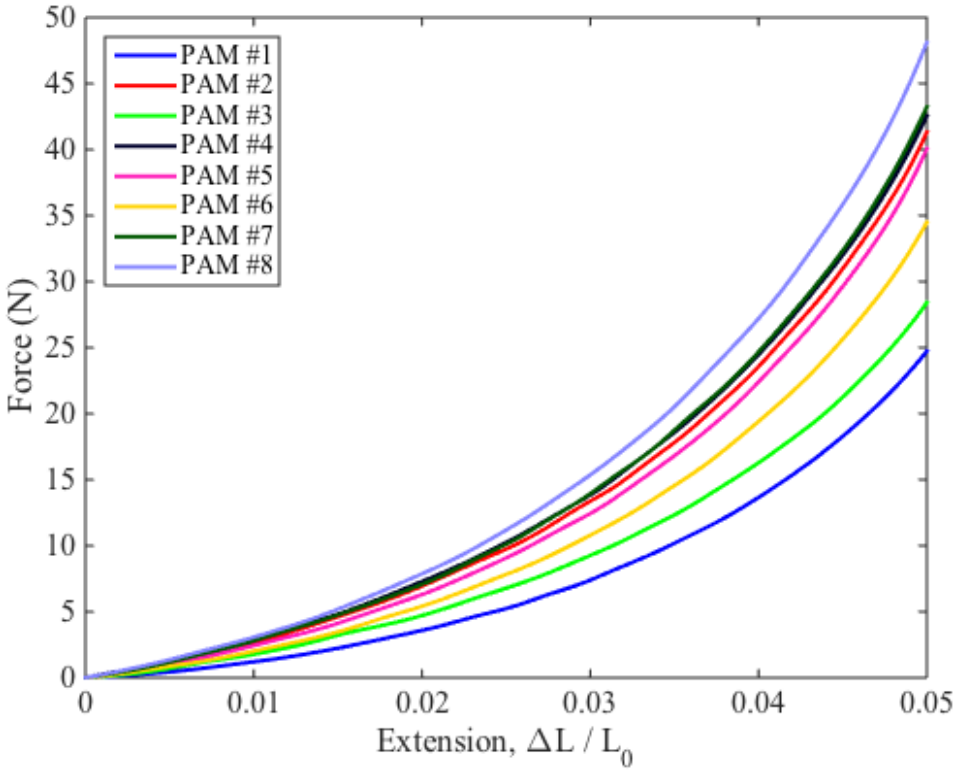

Figure 3.3: Average antagonist experimental data from the tensile testing of eight individual miniature PAMs (PAM numbers correspond to those in Table 3.1).

Figure 3.4: A bundle of eight miniature PAMs.

3.2.2. Modeling of Antagonistic Behavior of Miniature Pneumatic Artificial Muscles

The modeling technique for predicting the agonistic behavior of miniature PAMs was described in Section 2.3.1. The same technique was applied to predict the antagonistic behavior and is summarized below.

A force balance modeling approach was used (Kothera *et al.* 2009) with a nonlinear stress-strain relationship assumed for the bladder material (Hocking and Wereley 2013). In the force balance model, the total force, F, generated by a PAM is calculated using:

$$F = \frac{P}{4\pi N^2}(3L^2 - B^2) + P\left(\frac{V_B}{L'} - \frac{tL^2}{2\pi RN^2}\right) + \sigma_z \frac{V_B}{L'} - \sigma_c \frac{tL'^2}{2\pi RN^2}. \quad (3.26)$$

The first term in the expression is the Gaylord force term, where P is the actuation pressure, L is the instantaneous actuator length (determined by subtracting the contraction length, ΔL, from the initial length, L_0), B is the length of one fiber in the braid, and N is the number of turns one fiber makes around the bladder. B and N are determined as a function of the braid angle, α, and the outer diameter of the bladder, D:

$$B = \frac{L}{\sin\alpha} \quad (3.2)$$

$$N = \frac{B\cos\alpha}{\pi D}. \quad (3.3)$$

The additional terms in the force expression account for the bladder elasticity, where σ_z is the axial stress in the bladder, σ_c the circumferential stress in the bladder, R

and t are the instantaneous outer radius and thickness of the bladder, and V_B is the bladder volume, which is assumed to be constant.

Because antagonist data was only collected for unpressurized miniature PAMs, there is no corrected pressure term in this model. However, the model does include a corrected length term, L', to account for the non-cylindrical shape of the bladder near the end fittings:

$$L' = L - 2\Delta L. \tag{3.4}$$

ΔL is a length reduction term found using:

$$\Delta L = \left(\frac{\pi}{2} - 1\right)(R - R_0) \tag{3.5}$$

where R_0 is the initial outer radius of the bladder.

The axial and circumferential stresses are polynomial functions of the axial and circumferential strain:

$$\sigma = (E_{1I} + E_{1S}P)\epsilon^1 + (E_{3I} + E_{3S}P)\epsilon^3 \tag{3.6}$$

where E_k are optimized modulus values, and ε_z and ε_c are the axial and circumferential strain in the bladder:

$$\epsilon_z = \frac{L}{L_0} - 1 \tag{3.7}$$

$$\epsilon_c = \frac{R - \frac{t}{2}}{R_0 - \frac{t_0}{2}} - 1. \tag{3.8}$$

For the agonistic behavior, only the first and third order polynomial terms in a third-order nonlinear stress-strain relationship were necessary to model the quasi-static variation of PAM force with contraction. Only the first and third order polynomials were needed to accurately model the antagonist behavior as well; however, new optimization

parameters needed to be determined to model the antagonistic behavior. The model of the zero pressure antagonistic behavior of a single miniature PAM using the original optimization parameters determined during the agonist modeling is shown in Fig. 3.5a, while the model generated using the new optimization parameters is shown in Fig. 3.5b. Both are plotted against the average experimental data. Clearly, the model generated using the update optimization parameters is better and predicts the experimental data accurately within the zero to five percent extension range. In Fig. 3.6, the antagonist model prediction is shown for up to ten percent extension. This model demonstrates the high passive stiffness of PAMs in extension.

Using the above modeling and optimization process, an individual model was generated for each of the eight miniature PAMs used in the study. Note that these models were only optimized for an unpressurized miniature PAM and the optimization parameters may need to be recalculated based on pressurized antagonistic experimental data to predict antagonistic data for pressurized miniature PAMs. The antagonist models for each of the individual miniature PAMs are plotted against the corresponding antagonist experimental data in Fig. 3.7. Each of the models predicts the experimental trends well.

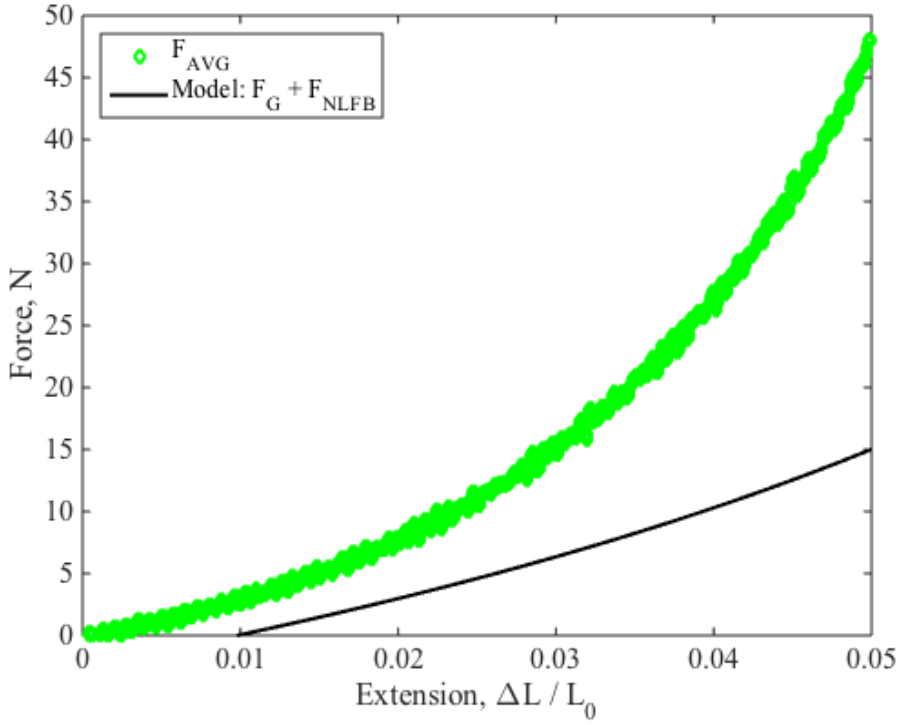

(a) Agonist Optimization Parameters

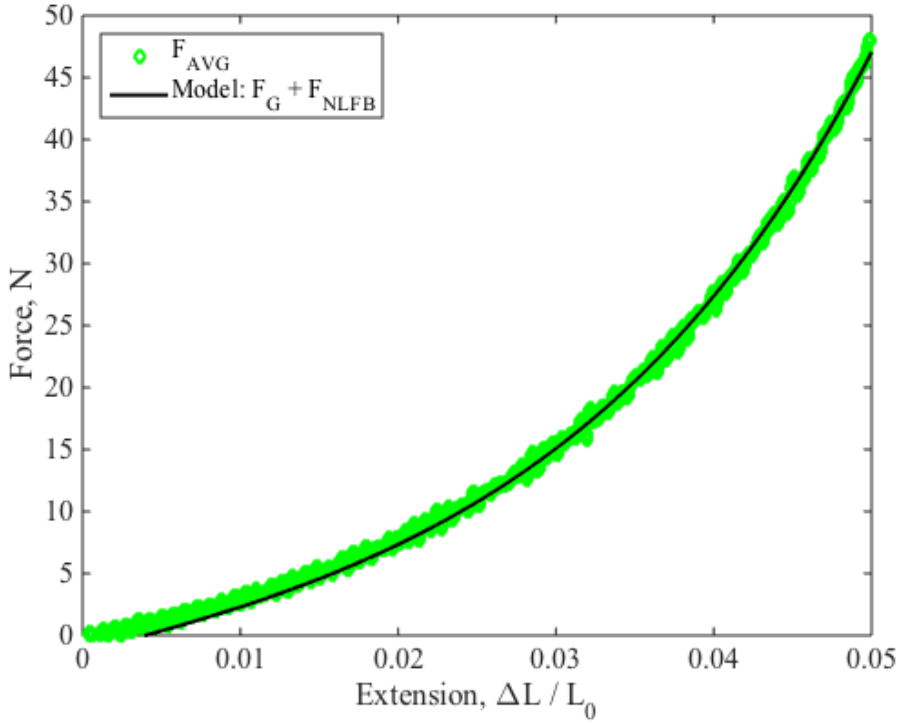

(b) Antagonist Optimization Parameters

Figure 3.5: Model of antagonist actuation behavior of miniature PAMs: the Gaylord Force (F_G) plus the Nonlinear Force Balance Model (F_{NLFB}) plotted versus the average experimental data (F_{AVG}) for zero to five percent extension.

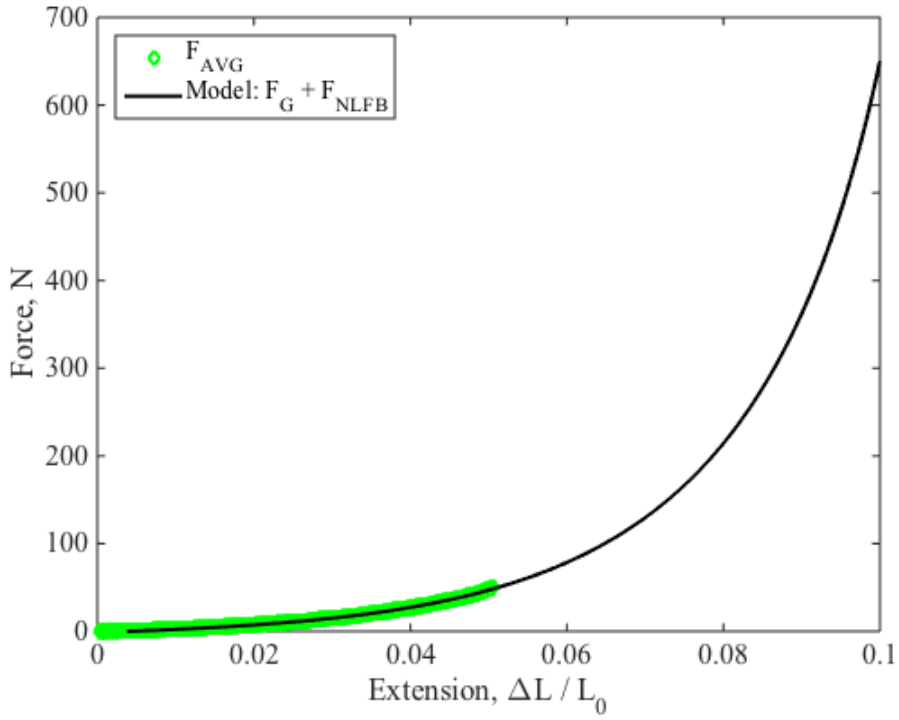

Figure 3.6: Model of antagonist actuation behavior of miniature PAMs for zero to ten percent extension.

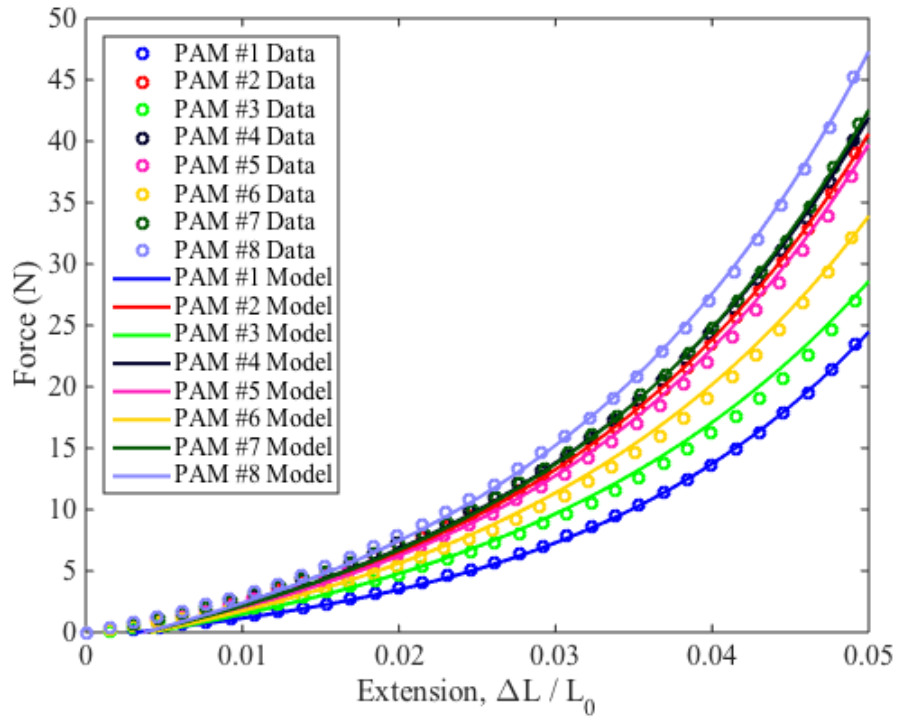

Figure 3.7: Model of antagonist actuation behavior of miniature PAMs plotted versus the average antagonist experimental data from the tensile testing of eight individual miniature PAMs.

3.2.3. Modeling of Antagonistic Behavior of Miniature Pneumatic Artificial Muscle Bundles

The modeling technique used to predict the agonistic behavior of the miniature PAM bundles can also be applied to predict the antagonistic behavior of the bundles. The variations in the active lengths of the miniature PAMs in the antagonist bundle reduce the total antagonistic force. For the bundle considered here, the active lengths of the miniature PAMs range from 6.63 to 7.06 cm (2.61 to 2.78 inches), with an average active length of 6.77 cm (2.67 inches) and a standard deviation of 0.14 cm (0.054 inches). The shortest miniature PAM could extend to 6.5% of its resting length before the longest miniature PAM would begin extending and producing any antagonistic force.

As proposed in Section 2.3.2, the model to predict the actuation behavior of a bundle of miniature PAMs is:

$$F_{bundle} = \sum_{i=1}^{m} F_i\left(\left(\frac{\Delta L}{L}\right)_i\right) \tag{3.9}$$

where F_{bundle} is the predicted force output of the bundle, m is the number of miniature PAMs in the bundle, and F_i is the predicted force output of the specified individual miniature PAM. This model is applicable for predicting both agonist and antagonist bundle behavior.

The predicted antagonist force output of an individual miniature PAM is a function of the percent extension of the specified PAM from its corresponding active length, $(\Delta L/L)_i$. The percent extension is found using:

$$\left(\frac{\Delta L}{L}\right)_i = \frac{L - L_{0i}}{L_{0i}} \tag{3.10}$$

where L_{0i} is the active length of the specified miniature PAM and L is the current length of the bundle.

The proposed model is highly dependent on both the actuation behavior of the individual miniature PAMs included in the bundle, as well as the variation in active lengths of the miniature PAMs. Effectively, the force versus extension curve for each individual miniature PAM included in a bundle is shifted along the contraction axis by its initial contraction, and then the resulting shifted curves are summed together to predict the total actuation behavior of the bundle. Unlike in the agonist bundle, where only the active (pressurized) miniature PAMs contributed to the total force of the bundle, every PAM in the antagonist bundle is stretched and contributes to the total force of the bundle.

The results of the modeling process for bundles of two, four, six, and eight PAMs can be seen in Fig. 3.8. The values predicted by the corrected model, which accounts for the active length variations, are plotted against the average data from the experimental characterization. Also plotted is the ideal model, which is the expected actuation behavior of the bundle if each miniature PAM had an identical resting length. This model is a simple summation of the actuation curves of each individual miniature PAM, without the application of any shifts to account for the variation in resting lengths of the miniature PAMs.

For each bundle of miniature PAMs (with two, four, six, and eight total PAMs), the average percent errors for both the corrected and ideal unpressurized antagonistic models were calculated using:

$$\%error = \frac{1}{N_i}\sum_{i=1}^{N_i}\left|\frac{(F_{AVG})_i - (F)_i}{F_{AVG}(0.05)}\right| \tag{3.11}$$

where N_i is the total number of data points compared, $(F_{AVG})_i$ is the average experimental force value at each percent contraction value compared, and $(F)_i$ is the predicted force value at each percent contraction value compared. The error is normalized by the force value at five percent extension. The percent error was determined by average the error over the range of zero to five percent extension.

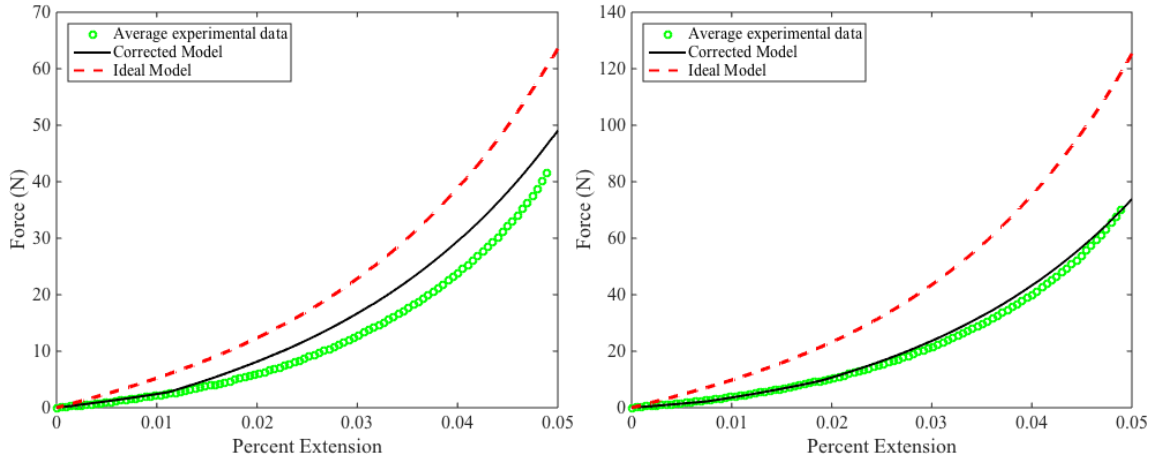

(a) Bundle of two miniature PAMs (b) Bundle of four miniature PAMs

(c) Bundle of six miniature PAMs (d) Bundle of eight miniature PAMs

Figure 3.8: Corrected and ideal models of antagonistic actuation behavior of a bundle of miniature PAMs plotted versus the average experimental data.

The present errors for the cases provided in Fig. 3.8 are provided in Table 3.2. The recruitment order assumed here was: miniature PAMs #3 and #6 as a pair, #1 and #5

added to make four PAMs, #2 and #7 to make six miniature PAMs, and #4 and #8 to make eight PAMs. For reference, the model error for the individual miniature PAM #3 is provided as reference. The experimental and modeling data, as well as their corresponding percent errors, would vary slightly for different combinations of miniature PAM in the bundles. The antagonistic corrected model percent errors are comparable to the errors presented in Table 2.4 for the agonistic behavior. However, the antagonistic ideal model percent errors are much larger than the agonistic ideal model percent errors and would continue to increase if the error was calculated over larger extension ranges. These higher errors occur due to the high passive stiffness of the miniature PAMs in extension.

Table 3.2: Average percent errors for models of actuation behavior of miniature PAM bundles.

No. of PAMs	Ideal Model Avg. % Error (%)	Corrected Model Avg. % Error (%)
1	1.8	1.8
2	21.0	7.2
4	28.0	2.0
6	44.9	1.1
8	38.6	2.3

The antagonistic behavior of a bundle of two miniature PAMs of identical length (miniature PAMs #4 and #8) is provided in Fig. 3.9. Here, the ideal and corrected models are the same, because there is no shift necessary to account for any length variation, and the models predict the average experimental data well. This overlap supports the assumption that reducing the variation in the lengths of miniature PAMs in a bundle can reduce the loss in the total bundle force production.

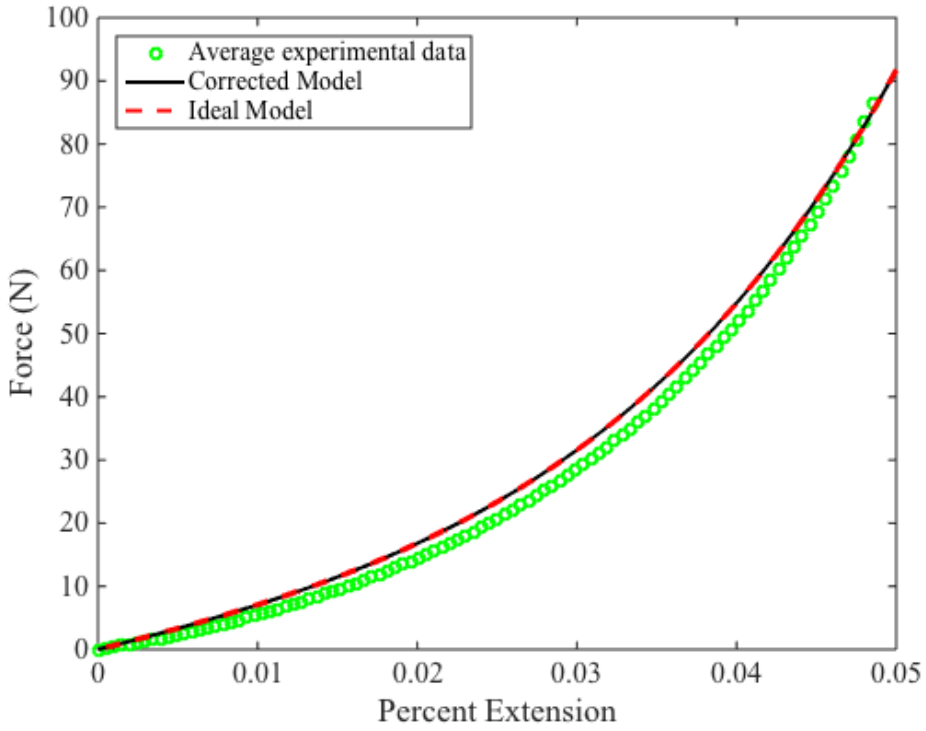

Figure 3.9: Corrected and ideal models of antagonistic actuation behavior of a bundle of two miniature PAMs of equivalent lengths plotted versus the average experimental data.

For the bundle combinations considered in Fig. 3.8, the average percent losses in antagonist force predicted by the corrected model from those values predicted by the ideal model are provided in Table 3.3. This table provides information on the losses experienced for each number of miniature PAMs due to the variation in active lengths of the bundle. The table also shows the possible gains in force production that could result from improvements in the fabrication process facilitating the production of more similar miniature PAMs. The percent loss is calculated as follows:

$$\%loss = \frac{1}{N_i}\sum_{i=1}^{N_i}\left|\frac{(F_I)_i - (F)_i}{F_I(0.05)}\right| \tag{3.12}$$

where N_i is the total number of data points compared and $(F)_i$ and $(F_I)_i$ are the predicted force values from the corrected and ideal models respectively at each percent contraction

value compared. The loss is normalized by the force value predicted by the ideal model at five percent extension.

Comparing the percent losses in antagonist force in Table 3.3 to the percent losses in agonist force in Table 2.6, it is clear that there are higher losses in antagonist force than agonist force due to the length variation in the bundles. These losses would increase if the models were compared over larger ranges of extension.

Table 3.3: Average percent loss for models of actuation behavior of miniature PAM bundles.

No. of PAMs	Avg. % Loss (%)
2	9.0
4	14.7
6	19.6
8	17.2

3.3. Development of a Bidirectional Actuator with an Antagonistic Pair of Pneumatic Artificial Muscle Bundles

3.3.1. Purpose/goals

The unidirectional behavior of a bundle of miniature PAMs was characterized in Chapter 2. However, PAMs must operate in antagonist pairs to achieve bidirectional motion. Thus, a bidirectional actuator was designed to facilitate the characterization and understanding of the bidirectional behavior of bundles of miniature PAMs operated in an agonist-antagonist configuration. For this bidirectional actuator, an antagonist pair of miniature PAM bundles operating a one degree of freedom joint, such as a biceps-triceps pair rotating an elbow joint, is considered.

The bidirectional actuator can be evaluated as a two-dimensional system with one degree of freedom about a single joint. The complexities in the system behavior primarily arise from the nonlinearity and hysteresis in the individual miniature PAM agonist and antagonist forces. The agonist bundle force is a function of the number of active miniature PAMs in the agonist bundle, the actuation pressure, the bundle contraction length, and the variation of resting lengths of the miniature PAMs in the agonist bundle. Similarly, the antagonist force is a function of the total number of miniature PAMs in the antagonist bundle, its extension length, and the variation of resting lengths of the miniature PAMs in the antagonist bundle. The contraction and extension lengths are a function of the system geometry at a given deflection angle.

3.3.2. Design of the Bidirectional Actuator Testing Apparatus

The computer-aided design (CAD) assembly of the antagonistic pair system is shown in Fig. 3.10. Four identical bundle plates were machined to assemble two bundles of up to eight total miniature PAMs each in a square pattern. At the center of each of the four bundle plates is a through hole for a screw to attach the bundle to the testing apparatus. The dimensions of the bundle plates are 5.1 cm x 5.1 cm (2 in. x 2 in.) with 1.3 cm (½ in.) spacing between each adjacent through hole.

The 18-8 Stainless Steel Hex Head Cap Screws (¼”-28 Thread, 2” Long) extending from the bundle plates are attached at one end to a vertical support plate (1/2” thick x 3” height x 6” width). The PAMs in each bundle are aligned so the pressurized air can be supplied from the direction of the vertical support plate. This support plate has two large through holes (0.55”) to feed through the tubing to supply the pressurized air. Any control system for the bidirectional actuator would be located behind this support plate.

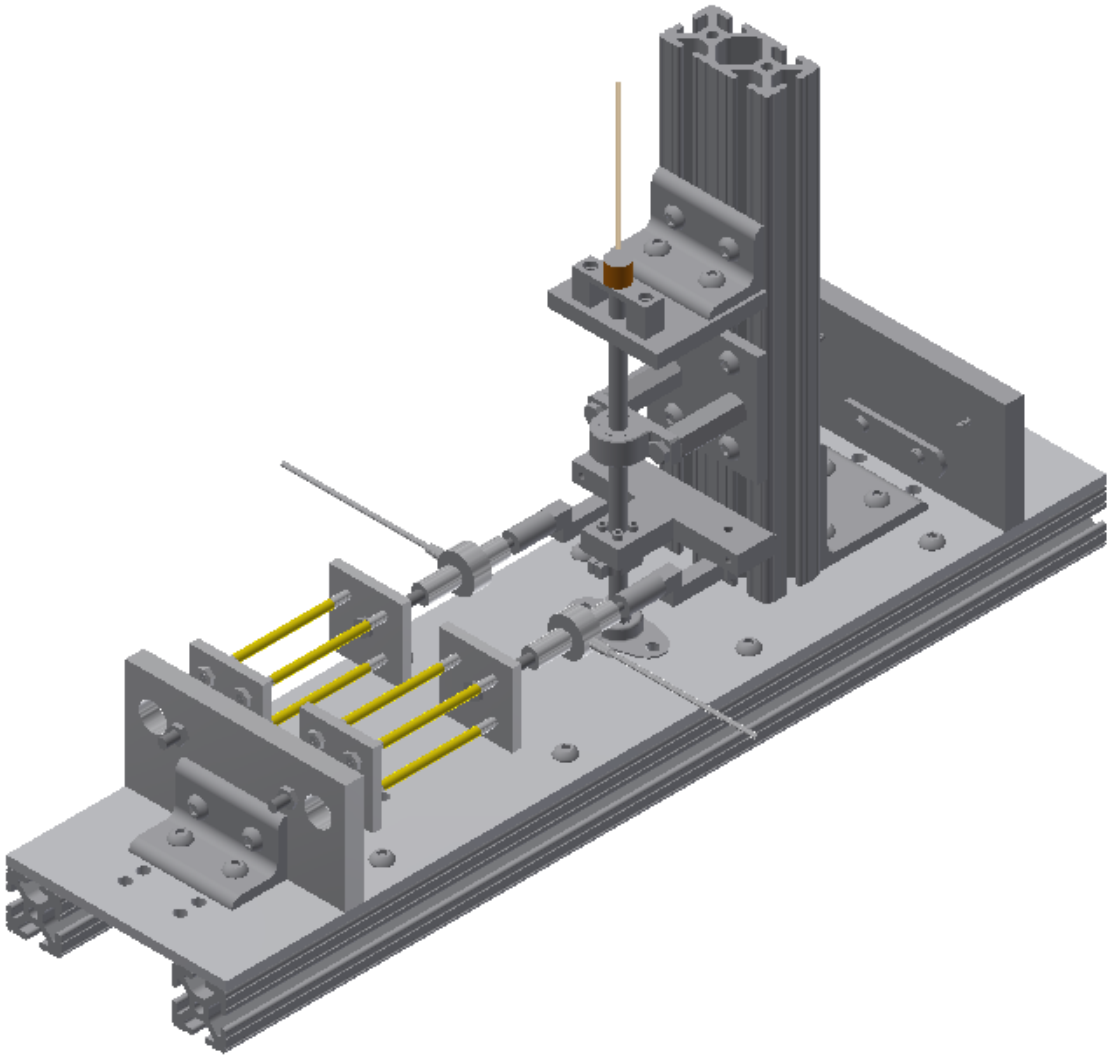

Figure 3.10: CAD model of a bidirectional actuator with an antagonist pair of miniature PAM bundles.

The screw at the other end of each bundle is attached to a load cell, and each load cell is attached to the lever arm of the bell crank mechanism, allowing the load cells to measure the force being generated in their corresponding bundles. TICN-Coated 18-8 Stainless STL Shoulder Screws (1/4” Diameter x 3/8” Long Shoulder, 10-32 Thread) allow the two pivot points at each end of the bell crank level arms to rotate freely as the system displacement angle changes and the miniature PAM bundles contract and extend in length.

A bell crank, which is an offset lever mechanism, was chosen over a simple lever or pulley for the system design. An offset lever mechanism reduces the effective moment arm for the antagonist bundle as the deflection angle is increased, which reduces the antagonist torque resisting the angular motion driven by the agonist muscle. A 0.77” Clamping Hub with (3/16” Bore) is used to attach the bell crank to the 3/16” aluminum pivot shaft. The shaft is supported at the base by a Steel Flange-Mounted Ball Bearing and above the bell crank by a Self-Lubricating Base-Mounted Bronze Bearing. The flange-mounted bearing is attached to a vertical support bar of 15-Series 1.5” x 3” T-Slotted Profiles from 80/20 Inc. via Aluminum Female Threaded Hex Standoffs (5/8" Hex, 1-3/4" Length, 10-32 Screw Size) and an aluminum adaptor plate.

The shaft of an angle sensor is inserted into the top of the pivot shaft and attached with a setscrew, allowing the angle sensor to record the angular displacement of the bidirectional actuator. The angle sensor is attached to a horizontal support plate extending from the 80/20 vertical support bar.

A second vertical plate (1/2” thick x 3” height x 6” width) is attached behind the 80/20 support bar. Two Steel Extension Spring Anchor Studs (1/4"-20 Thread, 1-1/4" Overall Length) are screwed into the front surface of the plate and aligned with two matching extension spring anchor studs screwed into the level arms of the bell crank. This way, two extension springs can be attached to the system to provide additional resistance to any angular displacement.

The entire structure is attached to a thin aluminum base plate (1/4” x 6” x 24”), which is supported underneath by two 80/20 15-Series 1.5” x 1.5” T-Slotted Profiles of 24” length each. The raised base platform allows the vertical support plates and bars to be

more easily attached to the base plate. The support plates and bars are attached to 80/20 15-Series Four and Eight Hole Inside Corner Brackets and the corner brackets are fixed to the baseplate with 80/20 button head socket cap screws inserted into through holes in the plate and screwed into 80/20 15-Series Double Economy T-nuts located underneath the baseplate.

The system was designed for adjustability to facilitate the testing of different size miniature PAM bundles, miniature PAMs, and short full-size PAMs. The vertical support plates for both the miniature PAM bundle attachments and the spring attachments are fixed to the baseplate. Multiple sets of through holes are aligned in even spacing along the base plate to accommodate shifting the attachment point for the support plates to handle different length PAMs and to vary the attachment length of springs.

3.3.3. Experimental Data

A picture of the final bidirectional actuator assembly is shown in Fig. 3.11. The noticeable difference between the CAD drawings and final assembly are the difference in the bundle lengths. The CAD assumed a constant length for each miniature PAM; however, the actual PAMs vary in length. For this setup, the PAMs were grouped into two sets of four to minimize the length variation within each bundle. The four shortest PAMs were grouped and used as the agonist (top) bundle: PAM numbers two, four, seven, and eight, which are 6,73, 6.68, 6.63, and 6.68 cm respectively. The four longest PAMs were grouped and used as the antagonist (bottom) bundle: PAM numbers one, three, five, and size, which are 7.06, 6.78, 6.73, and 6.86 cm respectively. As previously mentioned, the base plate of the system was designed to allow for variation in PAM

lengths so that testing of different miniature PAMs, small PAMs, and bundles could be tested with the same bidirectional actuator setup.

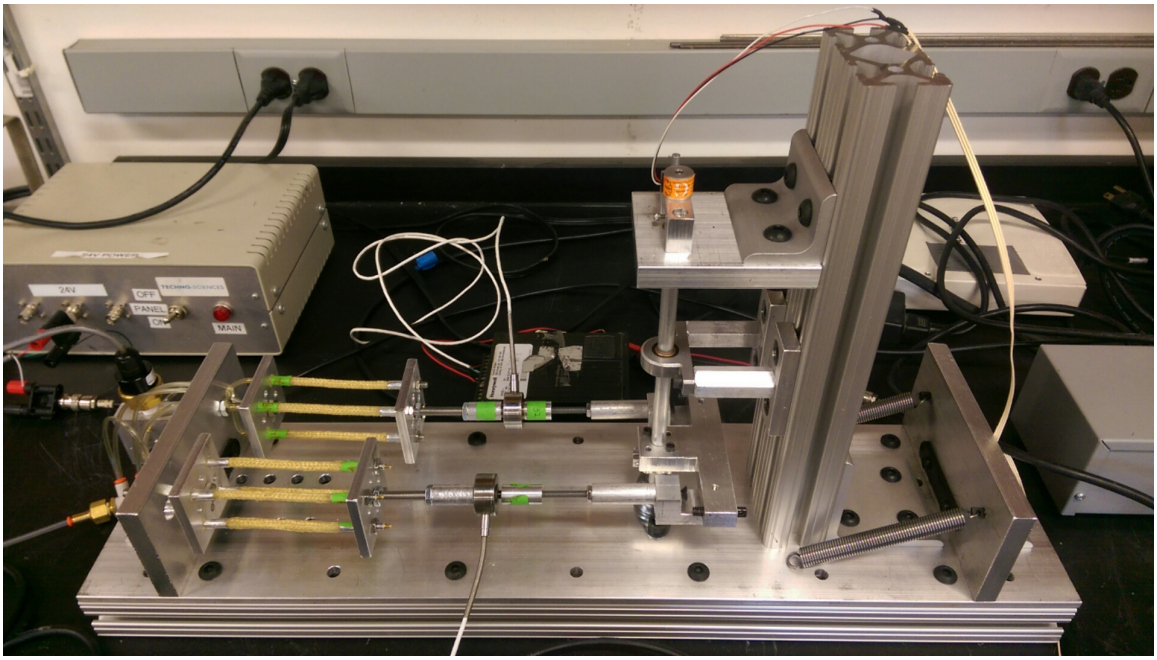

Figure 3.11: Physical assembly of a bidirectional actuator with an antagonist pair of miniature PAM bundles.

To collect quasi-static experimental data for the bidirectional actuator, the actuation pressure for the agonist PAM was slowly increased from zero to 552 kPa (80 psi), pausing in 138 kPa (20 psi) increments. The data acquisition was completed using LabVIEW SignalExpress. The experimental setup is designed to allow for the data collection of angular displacement, agonist and antagonist forces, and the pressure supplied to the agonist bundle. The angular displacement was recorded using a Single Shaft Contactless Hall-IC Angle Sensor (Model No. QP-2HC), whose shaft was inserted into a drilled hole in the top of the pivot rod of the bell crank and secured with a setscrew, allowing the angle sensor shaft to rotate in unison with the pivot shaft. The agonist force was measured with a Honeywell load cell (Model No. 31) rated for 445 N (100 lb) and

the antagonist force was measured with a Honeywell load cell (Model No. 31) rated for 4450 N (1000 lb). The pressure was measured with an Omega pressure transducer (Model No. PX181B) rated for 689 kPa (100 psig).

Due to the distance between the vertical support plate and the bell crank, as well as the compliant nature of the miniature PAMs, there is some sagging in the system. Three sets of data were collected and compared to determine the best method to handle the sagging. First, the system was allowed to sag while data was collected. Second, a block supported the slack underneath during testing. Third, the miniature PAM bundles were tightened to reduce the slack in the system. For the former two cases, the miniature PAM bundles were tightened until the point just when the load cells no longer read zero pounds of force.

The experimental data for the displacement angle, agonist bundle force, and antagonist bundle force collected for the three cases are plotted in Figs. 3.12-13. For this testing, each bundle was composed of four miniature PAMs, as described above. As expected, tightening the bundles to reduce slack increases both the agonist and antagonist forces, because both bundles are starting with initial extensions, which correspond to higher forces. This reduces the overall equilibrium angle for the system, which is undesirable because bidirectional PAM actuators already have limited ranges of motion. There is little difference between the actuator performance with the system allowed to slack or having the slack supported underneath, with the later only achieving a minimally larger equilibrium angle.

As the pressure in the system (agonist bundle) is increased, the agonist bundle contracts and the antagonist bundle extends. This means the antagonist bundle is

operating on the loading portion of its force versus contraction profile. As the agonist bundle is depressurized, the antagonist bundle is allowed to return to its resting length and is operating on the unloading portion of its force versus contraction profile. However, the agonist system is always operating on the unloading portion of its force versus contraction profile because it is able to shift its length in response to its changing actuation pressure. While the agonist motion is limited due to the resistive antagonist force, the agonist bundle is never stretched or operated on the loading portion of its hysteresis curve. The hysteresis in the antagonist data during operation causes a corresponding hysteresis in the equilibrium angle. During pressurization, the equilibrium angle at a given pressure value is lower than the equilibrium angle during depressurization at the same pressure value.

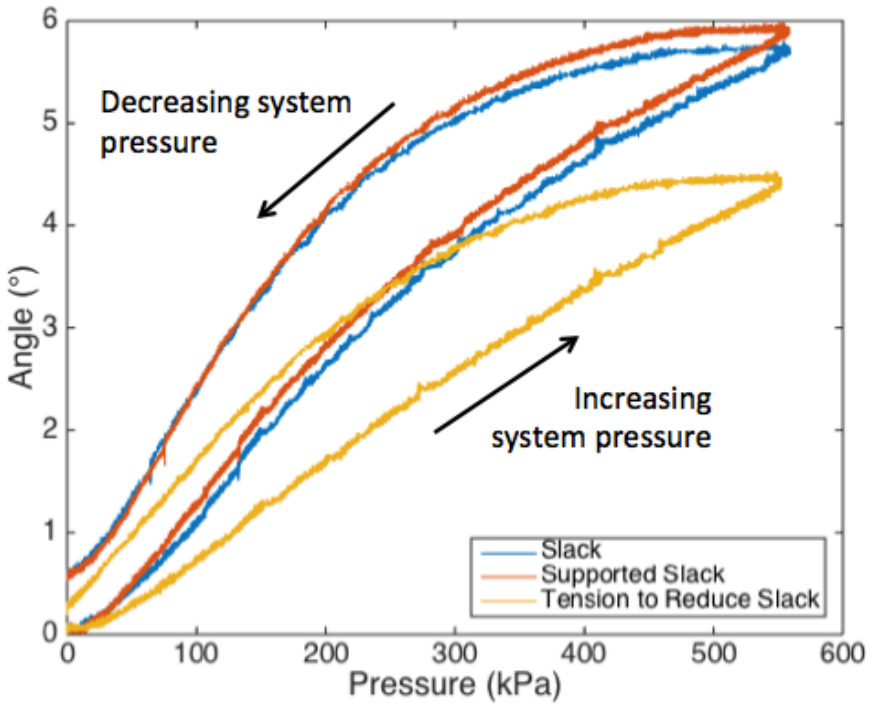

Figure 3.12: Displacement versus pressure during quasi-static operation of the bidirectional actuator with an antagonist pair of miniature PAM bundles.

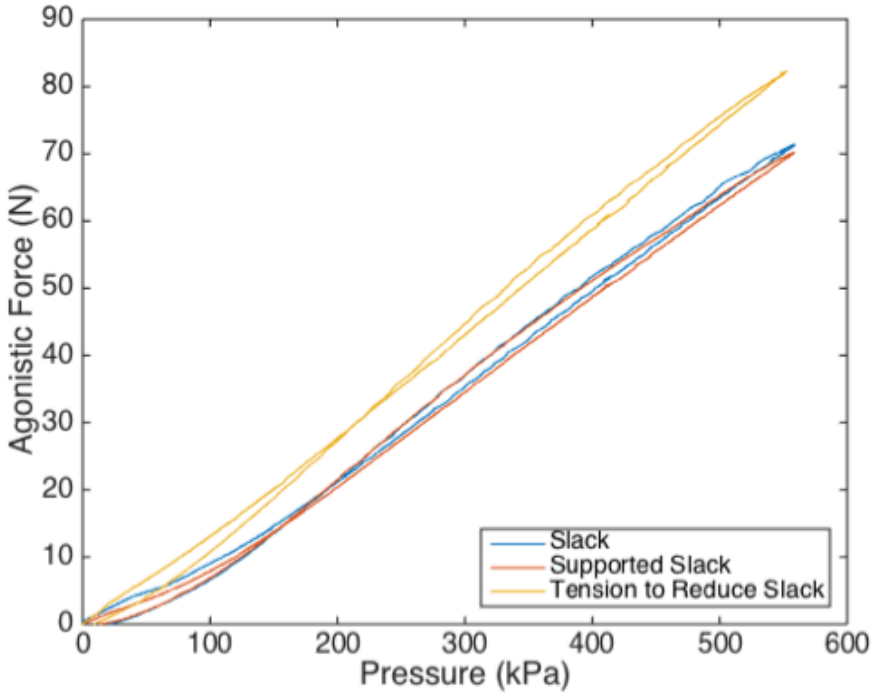

(a) Agonist Force

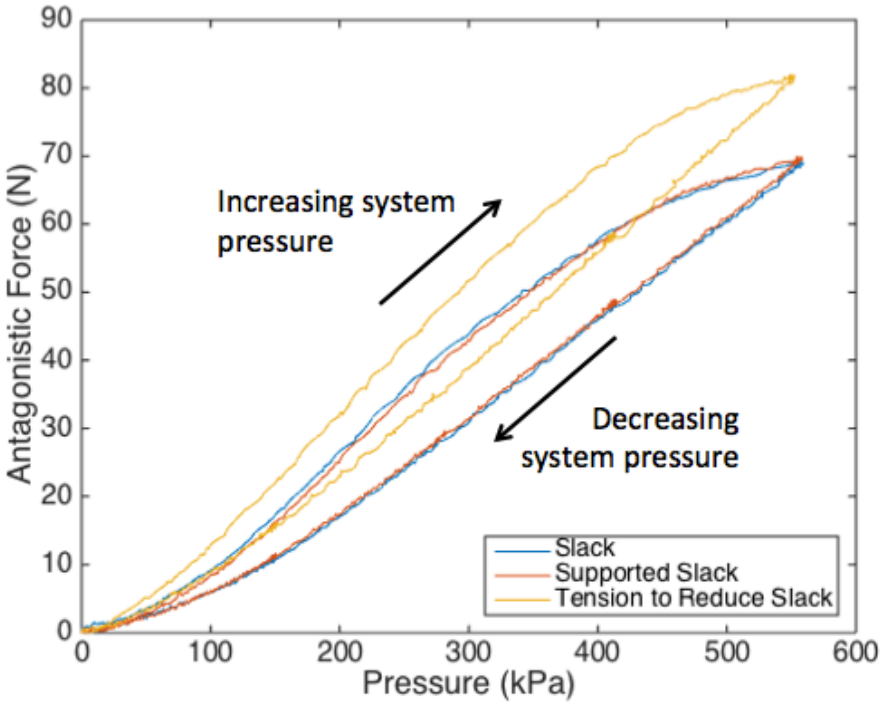

(b) Antagonist Force

Figure 3.13: (a) Agonist and (b) antagonist force versus pressure during quasi-static operation of the bidirectional actuator with an antagonist pair of miniature PAM bundles.

3.4. Development of a Quasi-Static Model for the Bidirectional Actuator

3.4.1. System Geometry

The bidirectional miniature PAM bundle actuator considered here is a single degree of freedom system. Accounting for the system geometry, the angular displacement of the pivot shaft, measured by the angle sensor, corresponds to a set contraction of the agonist miniature PAM bundle and a set extension bundle of the antagonist bundle. The agonist and antagonist forces of the bundles are directly related, through a nonlinear relationship, to the displacement of each bundle, and, therefore, the angular displacement of the system. As the agonist bundle is pressurized, it wants to contract and rotate the system about the pivot shaft. The antagonist bundle produces an opposing force to this motion. Either bundle in the system can be pressurized and act as the agonist bundle, and either bundle can provide the resistive force as the antagonist bundle.

The antagonist pair geometry presented in Fig. 3.14 was originally presented by Vocke *et al.* (2014) to describe the behavior of a bidirectional PAM actuator with an offset lever configuration. As the agonist muscle contracts, it pulls on the bell crank and causes the system to rotate about the pivot point. The antagonist muscle simultaneously extends, producing an opposing force to the deflection of the system, until the system reaches an equilibrium state where the opposing torques are equal. The system is presented in its undeflected (dashed gray lines) and deflected (solid black lines) states. The benefit of using an offset lever configuration is that it reduces the moment arm for the antagonist PAM bundle relative to the moment arm for the agonist PAM bundle at a given deflection, δ. The use of an offset lever, instead of a conventional lever or pulley, is

one method of increasing the achievable deflection at a given pressure by reducing the antagonist torque relative to the agonist torque at a given deflection.

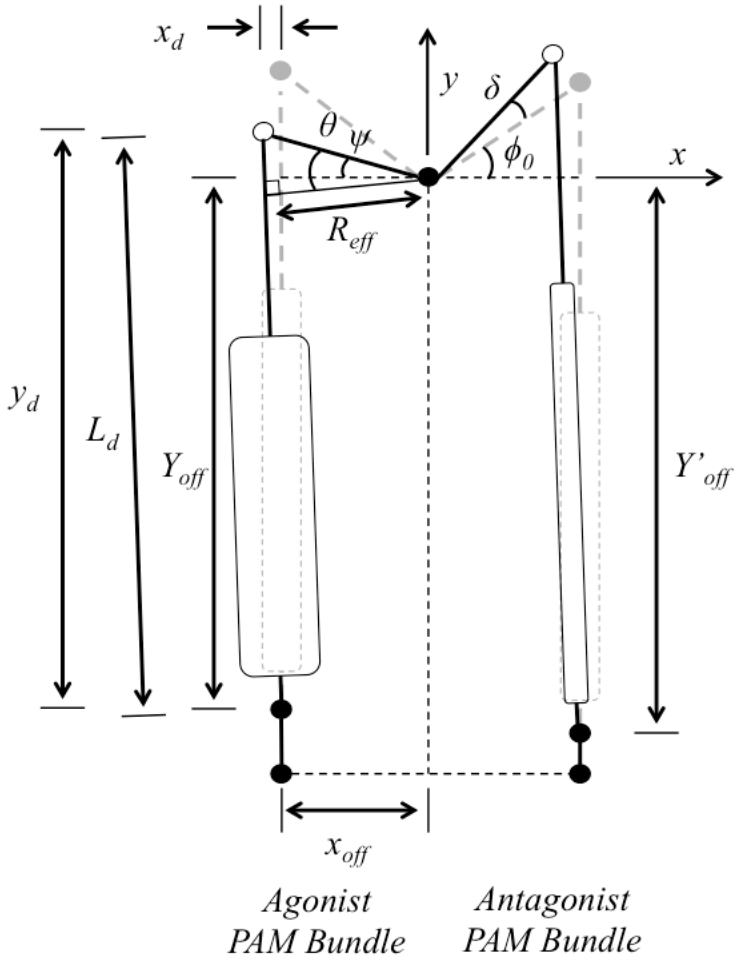

Figure 3.14: Dimensioned sketch of a bidirectional PAM actuator with a bell crank lever mechanism. Similar to the sketch provided by Vocke *et al.* (2014).

The constant, known system parameters are offsets of the PAM mounting points from the bell crank pivot point in the x-direction and y-direction (x_{off} and y_{off}) for each bundle, as well was the angle ϕ_0, characterizing the angle between the x-axis and the PAM lever line at zero displacement. During angular displacement of the system, the

angle, ψ, between the x-axis and the active PAM lever line is found by subtracting the system displacement angle, δ, from ϕ_0:

$$\psi = \phi_0 - \delta. \tag{3.13}$$

The displacements of the agonist bell crank pivot point from the PAM mounting point in the x-direction and y-direction (x_d and y_d) are determined as follows:

$$x_d = x_{off} \frac{\cos(\psi)}{\cos(\phi_0)} - x_{off} \tag{3.14}$$

$$y_d = x_{off} \frac{\sin(\psi)}{\cos(\phi_0)} + y_{off}. \tag{3.15}$$

The corresponding length (L_d) between the PAM mounting point to the agonist bell crank pivot point is defined as:

$$L_d = \sqrt{x_d^2 + y_d^2}. \tag{3.16}$$

The angle between the active lever line and the axis of the effective moment arm (R_{eff}) is determined by:

$$\theta = \psi + \operatorname{atan}\left(\frac{x_d}{y_d}\right). \tag{3.17}$$

The corresponding effective moment arm is:

$$R_{eff} = x_{off} \frac{\cos(\theta)}{\cos(\phi_0)}. \tag{3.18}$$

The change in length, ΔL, of the agonist bundle, which is the only part of the arm with flexible length, is found by subtracting the current length between the pivot shaft to the agonist bell crank pivot point from the original length:

$$\Delta L = -L_d + y_{off} + \tan(\phi_0)\, x_{off}. \tag{3.19}$$

A positive displacement corresponds to a contraction and a negative displacement corresponds to an extension.

The same approach is used to find the displacement of the antagonist (passive) bundle. Due to the length variation in the miniature PAM bundles, the antagonist bundle has a different offset of the bell crank pivot point from the PAM mounting point in the y-direction. Here, the angle, ψ, between the active PAM lever line and the x-axis is found by adding the system displacement angle, δ, to ϕ_0:

$$\psi = \phi_0 + \delta. \tag{3.20}$$

Otherwise, the calculations are identical. The displacements of the agonist bell crank pivot point from the PAM mounting point in the x-direction and y-direction and the corresponding length between the PAM mounting point to the agonist bell crank pivot point are:

$$x_d = x_{off} \frac{\cos(\psi)}{\cos(\phi_0)} - x_{off}. \tag{3.21}$$

$$y_d = x_{off} \frac{\sin(\psi)}{\cos(\phi_0)} + y_{off}. \tag{3.22}$$

$$L_d = \sqrt{x_d^2 + y_d^2}. \tag{3.23}$$

The angle between the active PAM lever line to the axis of the effective moment arm (R_{eff}) and the corresponding effective moment arm are:

$$\theta = \psi + \operatorname{atan}\left(\frac{x_d}{y_d}\right). \tag{3.24}$$

$$R_{eff} = x_{off} \frac{\cos(\theta)}{\cos(\phi_0)}. \tag{3.25}$$

Finally, the change in length of the antagonist bundle is:

$$\Delta L = -L_d + y_{off} + \tan(\phi_0)\, x_{off}. \tag{3.26}$$

A modification was applied to the original geometry to more accurately account for the contraction or extension of each miniature PAM in each bundle. Because one bundle plate is held fixed at the end of the assembly, while the other plate is allowed to rotate to maintain a perpendicular alignment with the axis of the fixed PAM attachment point to the bell crank pivot points, the miniature PAMs in each bundle will not all contract or extend to exactly the same length. This variation is depicted in Fig. 3.15.

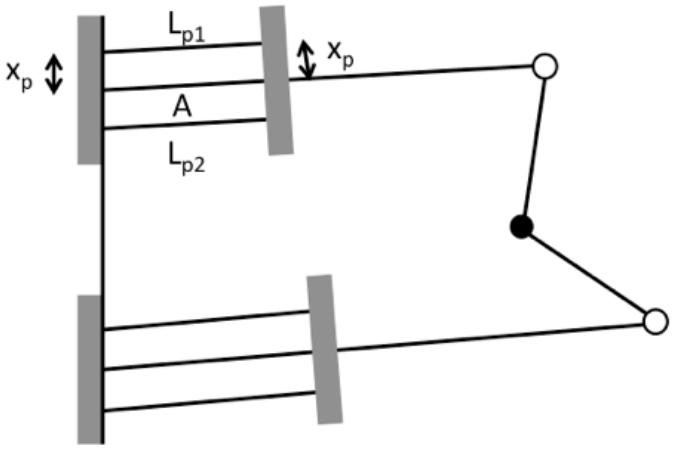

Figure 3.15: Modified PAM bundle geometry during angular displacement of the bidirectional actuator.

The same approach can be used to find the contraction length of each miniature PAM in the agonist bundle or the extension length of each miniature PAM in the antagonist bundle, with the appropriate choice of the overall initial length, L_0, and contraction or extension, ΔL, for the bundle. Fig. 3.16 shows the dimensions for each of the PAMs in a bundle of a given bundle contraction or extension length, A, found using:

$$A = L_0 - \Delta L. \tag{3.27}$$

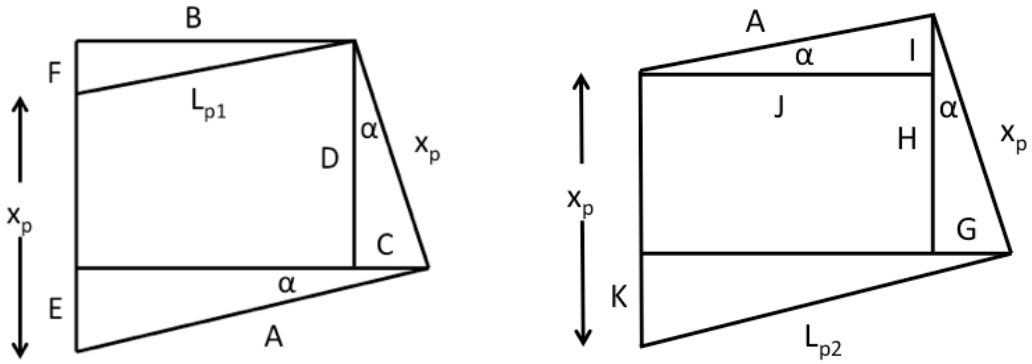

(a) Shorter PAM length, L_{p1} (b) Longer PAM length, L_{p2}

Figure 3.16: Modified PAM bundle geometry during angular displacement of the bidirectional actuator.

The angle between the y-axis and the axis of the bundle is:

$$\alpha = \text{atan}\left(\frac{x_d}{y_d}\right). \tag{3.28}$$

From Fig. 3.16a, the bundle dimensions are found using:

$$C = x_p \sin(\alpha) \tag{3.29}$$

$$B = A\cos(\alpha) - C \tag{3.30}$$

$$D = x_p \cos(\alpha) \tag{3.31}$$

$$E = A\sin(\alpha) \tag{3.32}$$

$$F = D - \left(x_p - E\right). \tag{3.33}$$

The length of the two PAMs with the most contraction in the agonist bundle or the least extension in the antagonist bundle is:

$$L_{p1} = \sqrt{F^2 + B^2}. \tag{3.34}$$

From Fig. 3.16b, the remaining bundle dimensions are found using:

$$J = A\cos(\alpha) \tag{3.35}$$

$$I = A\sin(\alpha) \tag{3.36}$$

$$H = x_p \cos(\alpha) - I \tag{3.37}$$

$$G = x_p \sin(\alpha) \tag{3.38}$$

$$K = x_p - H. \tag{3.39}$$

The length of the two PAMs with the least contraction in the agonist bundle or the most extension in the antagonist bundle is:

$$L_{p2} = \sqrt{K^2 + (J + G)^2}. \tag{3.40}$$

For each displacement angle, there is a single corresponding contraction or extension value for each PAM in the system. The contraction values and operating pressure for the agonist bundle, and extension values for the antagonist bundle, can be used to determine the corresponding agonist and antagonist force produced by each miniature PAM. These forces are then summed to predict the total force produced by the agonist and antagonist bundles. While only the active miniature PAMs in the antagonist bundle contribute to the agonist bundle force, each miniature PAM in the antagonist bundle is extended and contributes to the total antagonist force. The variations in length due to the bundle geometry correction to account for the different lengths of each PAM in the bundle when one bundle plate is held fixed and the other is allowed to rotate have a minimal effect on the total force in each bundle; however, this modification to the model geometry is provided for completeness.

The moment produced by each bundle about the system pivot point, O, can be found using the total force in each bundle and the effective moment arm for each bundle corresponding to a given displacement angle:

$$M_0 = r \times F = FR_{eff}. \tag{3.41}$$

Using the total bundle forces and effective moment arms for each bundle, the total moment about the system pivot point due to the bidirectional actuator can be found using:

$$M_{0,tot} = M_{0,a} - M_{0,p} = F_a R_{eff,a} - F_p R_{eff,p}. \tag{3.42}$$

To solve for the equilibrium conditions for the system, find the equations of motion and set the state derivatives equal to zero. To find the equations of motion for the system, sum the moments about the internally fixed pivot point *O* and set the total moment about *O* equal to the time rate of change of the angular momentum about *O*. Fig. 3.17 is the free body diagram for the system. For a pinned (inertially-fixed) pivot-point *O*, the equations of motion can be found using:

$$^I\frac{d}{dt}\left(\,^I\bar{h}_O\right) = \bar{M}_O \tag{3.43}$$

The angular momentum of the system and its time-derivative are:

$$^I\bar{h}_O = I_O\ ^I\omega^B\hat{b}_3 = I_O\dot{\theta}\hat{b}_3 = I_O\dot{\theta}\hat{e}_3 \tag{3.44}$$

$$^I\frac{d}{dt}\left(\,^I\bar{h}_O\right) = I_O\ ^I\alpha^B\hat{e}_3 = I_O\ddot{\theta}\hat{e}_3. \tag{3.45}$$

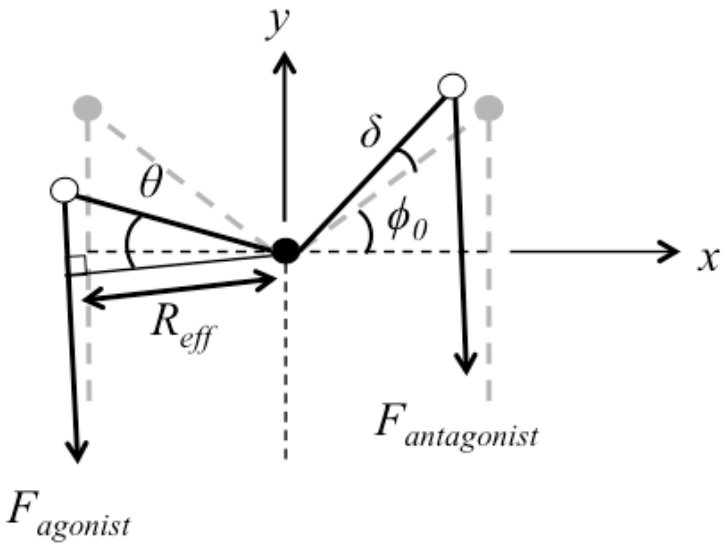

Figure 3.17: Free body diagram for bidirectional actuator with bell crank mechanism.

For the position and angular velocity states, the derivatives are angular velocity and angular acceleration. Setting these derivatives to zero, we have:

$$\dot{\delta}^* = 0 \tag{3.46}$$

$$\ddot{\delta}^* = \frac{M_{0,tot}(P, \delta^*)}{I_0} = 0 \tag{3.47}$$

where the $\dot{\delta}^*$ and $\ddot{\delta}^*$ denote the equilibrium conditions. Equilibrium occurs when: $\ddot{\delta} = \dot{\delta} = 0$ because the system is neither moving nor accelerating. $M_{0,tot}$ can be written as a function of the displacement angle, δ^*, and the operating pressure of the agonist bundle. For a given pressure, the equilibrium displacement angle can be found in MATLAB using a numeric solver.

Although these equations of motion are sufficient for estimating the quasi-static and equilibrium behavior of the system, they would need to be improved to accurately predict dynamic behavior. The system will experience viscous damping due to multiple sources, including dynamic damping in the miniature PAMs, damping in the springs, and frictional damping at the bell crank pivot points. The viscous damping coefficient for the system is difficult to predict due to the number of contributing sources. Because damping is traditionally incorporated into the model with a $-c\dot{\delta}$ term, where c is the rotational friction or damping coefficient, damping is zero at the equilibrium condition when $\dot{\delta} = 0$. Thus, damping can be reasonably ignored in the prediction of quasi-static steady-state behavior for the system.

There are additional considerations that would need to be incorporated into a model for the dynamic behavior of the pneumatic actuator and the dynamic behavior of the system. Kang *et al.* (2009) proposed a model for the dynamic modeling of the actuation of PAMs that accounted for the airflow dynamics through pneumatic valve

orifices and the thermodynamics of the air inside the bladder as the actuation pressure fluctuates. Robinson *et al.* (2014) developed a dynamic model for the pneumatic actuators that accounted for the compressibility of air, heat transfer in the system valves, PAM volume fluctuation during actuation, and the PAM deadband pressure. Woods *et al.* (2014) developed a dynamic model for an antagonist pair bidirectional actuator for trailing edge flap control. The model incorporated a spool valve mass flow rate model, a tubing loss model, the PAM model (including an internal PAM pressure model, PAM internal air volume model, and the PAM force model), the system geometry and kinematics, and the flap dynamics equation of motion with inertia, stiffness, and damping terms.

3.4.2. Hysteresis

As discussed in Section 3.3.3, the equilibrium angle and antagonist bundle force vary depending on whether the agonist bundle is being pressurized or depressurized. This is a consequence of the hysteresis in the PAM performance data due to internal friction in the miniature PAMs (Chou and Hannaford 1996, Davis and Caldwell 2006). From Fig. 3.12, the hysteresis accounts for approximately a degree of difference between the pressurization and depressurization quasi-static equilibrium angles at 276 kPa (40 psi). Therefore, using the average miniature PAM agonist model developed in Section 2.3.1 and the antagonist model developed in Section 3.2.2 to predict the actuation behavior of miniature PAMs will cause the bidirectional actuator model under predict the antagonist force and over predict the agonist force as the system is pressurized. Each PAM contributes up to a 5 N (1.1 lb) magnitude variation in its agonist and antagonist force when the experimental data with the hysteresis is compared to the model of the average

miniature PAM force. With blocked forces in the 55 N (12.4 lb) range at a maximum pressure of 621 kPa (90 psi), this force variation between the model and experimental data with hysteresis is significant when each PAM in the agonist and antagonist bundle is contributing to the total error in force predicted by the model.

To better predict the behavior of the bidirectional actuator, the models of the individual miniature PAMs are updated to account for hysteresis. Hocking and Wereley (2013) modeled the friction force as:

$$F_F = -k_F(F_{PAM})\,\mathrm{sgn}(v) \tag{3.48}$$

where k_F is a friction coefficient, F_{PAM} is average miniature PAM force without friction, and v is the velocity. The total PAM force is $F = F_{PAM} + F_F$. The velocity is positive during contraction (the unloading portion of the curve), so the friction force decreases the overall miniature PAM force. During extension, the velocity is negative (the loading portion of the curve) and the friction force increases the overall miniature PAM force.

The agonist hysteresis is well predicted by varying the friction coefficient as a function of pressure as:

$$k_F = -0.001P + 0.22. \tag{3.49}$$

The results are presented in Fig. 3.18 for the four miniature PAMs included in the agonist bundle. This model is worse in the free contraction region; however, the high passive stiffness of the antagonist bundle should prevent the system from achieving a high enough displacement angle to operate in the more poorly predicted regions.

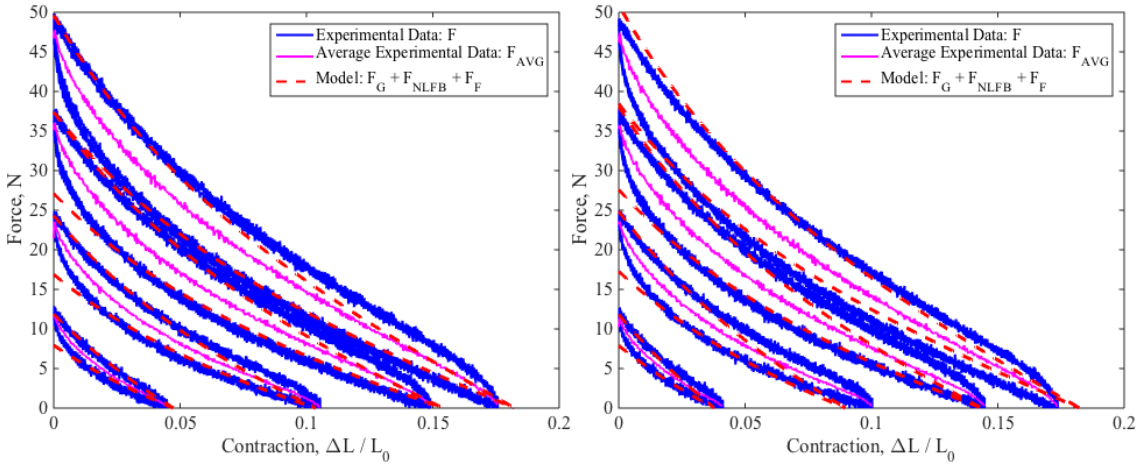

(a) Miniature PAM #2 (b) Miniature PAM #4

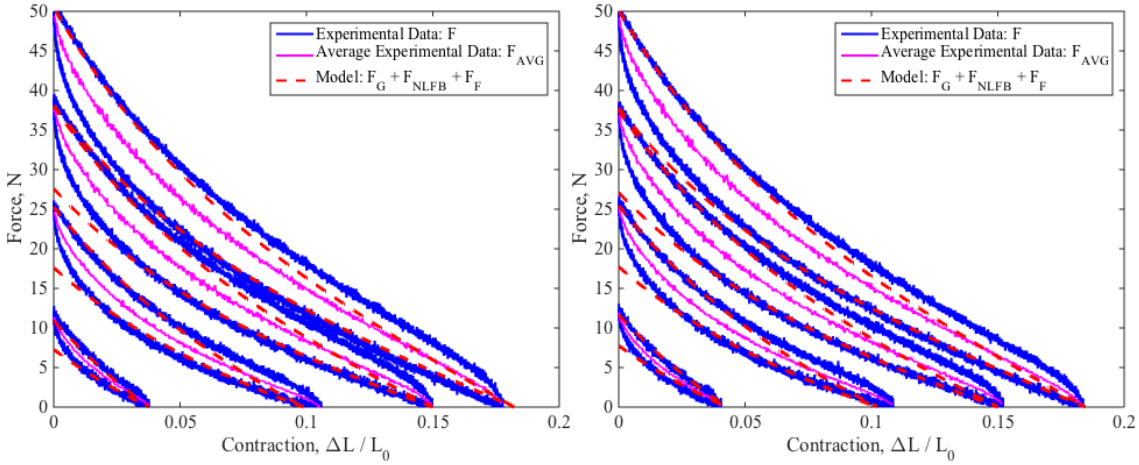

(a) Miniature PAM #7 (b) Miniature PAM #8

Figure 3.18. Model of agonist actuation behavior of miniature PAMs: the Gaylord Force (F_G) plus the Nonlinear Force Balance Model (F_{NLFB}) plus the Friction Force (F_F) plotted versus the experimental data (F) and average experimental data (F_{AVG}) at 138, 276, 414, and 552 kPa (20, 40, 60, and 80 psi).

The antagonist hysteresis for the unpressurized miniature PAMs is well predicted by assuming a constant friction coefficient of $k_F = 0.12$. The results are presented in Fig. 3.19 for the four miniature PAMs included in the antagonist bundle. Although the model still under predicts the force during the loading portion of the hysteresis curve at lower extensions, the friction coefficient was chosen to better predict the experimental data at higher extensions.

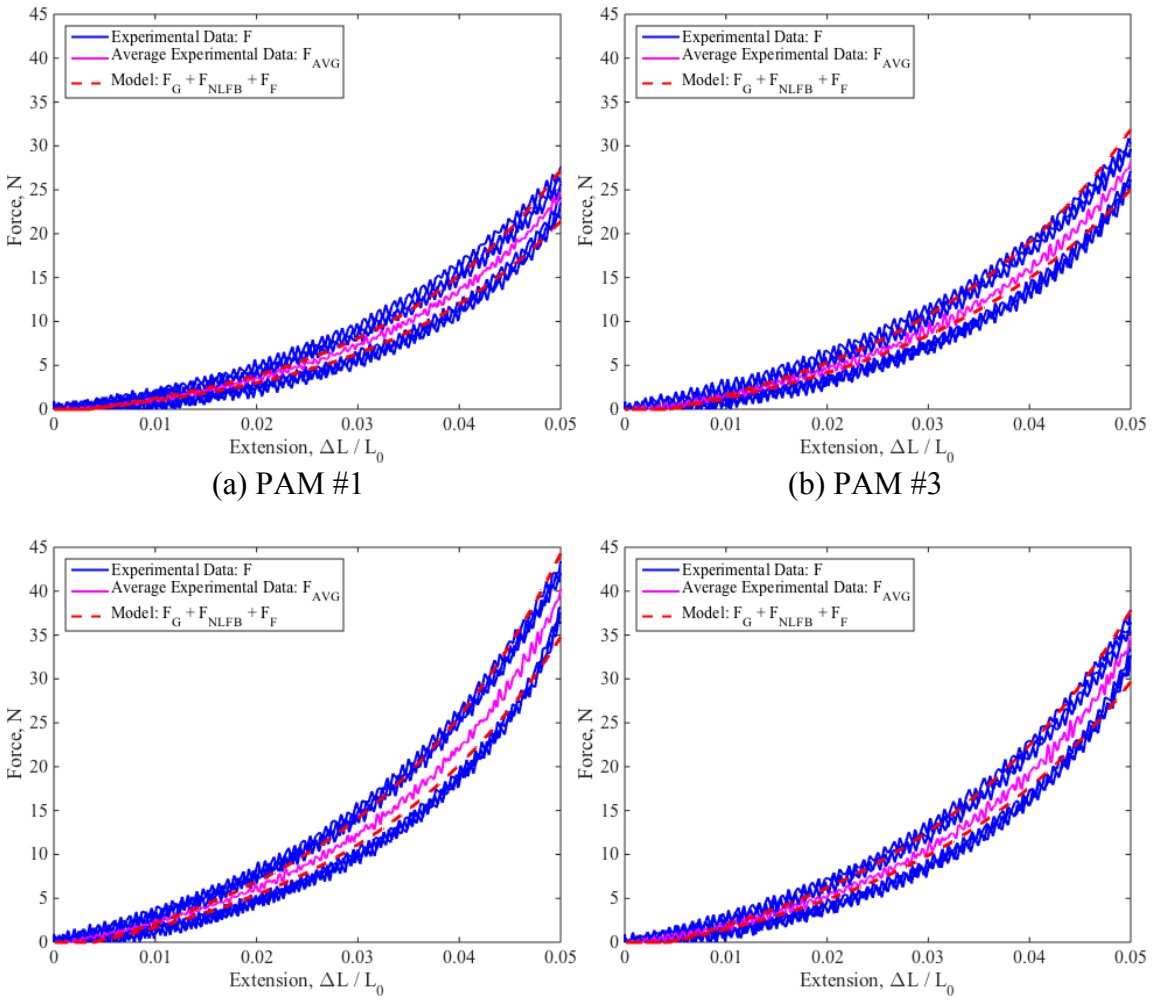

Figure 3.19. Model of the antagonist actuation behavior of unpressurized miniature PAMs: the Gaylord Force (F_G) plus the Nonlinear Force Balance Model (F_{NLFB}) plus the Friction Force (F_F) plotted versus the experimental data (F) and average experimental data (F_{AVG}).

3.4.3. Spring Forces

The current model only predicts the equilibrium behavior for the system without any externally applied forces. The system was designed to attach spring forces to the bell crank to provide an additional applied moment to resist angular displacement. The model needs to be updated to incorporate the effect of the springs on the equilibrium angle and forces.

As seen in Fig. 3.20, as the displacement angle, δ, changes, the lengths and moment arms of the springs also vary. The calculations of the spring lengths and effective moment arms are similar to the calculations for the displacement and effective moment arms of the agonist and antagonist bundles.

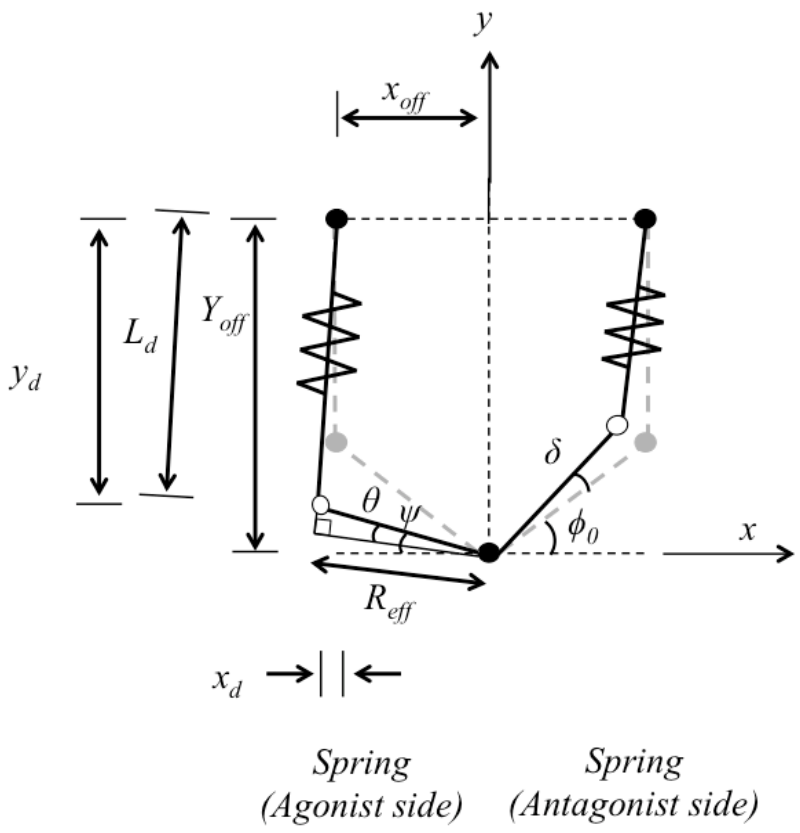

Figure 3.20: Dimensioned sketch of the applied torques due to spring forces in a bidirectional PAM actuator with a bell crank lever mechanism.

For the spring attached to the agonist arm of the bell crank (spring #1), the constant, known system parameters are the offsets of the spring mounting points from the bell crank pivot point in the x-direction and y-direction (x_{off} and y_{off}) for each spring, as well was the angle ϕ_0 between the x-axis and the initial lever arm of the bell crank.

During angular displacement of the system, the angle, ψ, between the x-axis and the active lever arm is found by subtracting the system displacement angle, δ, from ϕ_0:

$$\psi = \phi_0 - \delta. \tag{3.50}$$

The displacements of the agonist bell crank pivot point from the spring mounting point in the x-direction and y-direction (x_s and y_s) are determined as follows:

$$x_s = x_{off} \frac{\cos(\psi)}{\cos(\phi_0)} - x_{off} \tag{3.51}$$

$$y_s = -x_{off} \frac{\sin(\psi)}{\cos(\phi_0)} + y_{off}. \tag{3.52}$$

The corresponding spring length (L_s) is:

$$L_s = \sqrt{x_s^2 + y_s^2}. \tag{3.53}$$

The angle between the active lever arm and the axis of the effective moment arm (R_{eff}) for the spring force is determined by:

$$\theta = \psi - \text{atan}\left(\frac{x_d}{y_d}\right). \tag{3.54}$$

The corresponding effective moment arm is:

$$R_{eff} = x_{off} \frac{\cos(\theta)}{\cos(\phi_0)}. \tag{3.55}$$

The length and effective moment arm of the spring attached to the antagonist half of the bell crank (spring #2) are found using a similar approach. The angle, ψ, between the x-axis and the active lever arm is found by adding the system displacement angle, δ, to ϕ_0:

$$\psi = \phi_0 + \delta. \tag{3.56}$$

The displacements of the antagonist bell crank pivot point from its spring mounting point in the x-direction and y-direction and the spring length are determined as follows:

$$x_s = x_{off}\frac{\cos(\psi)}{\cos(\phi_0)} - x_{off} \tag{3.57}$$

$$y_s = -x_{off}\frac{\sin(\psi)}{\cos(\phi_0)} + y_{off} \tag{3.58}$$

$$L_s = \sqrt{x_s^2 + y_s^2}. \tag{3.59}$$

The angle between the active lever arm and the axis of the effective moment arm (R_{eff}) for the spring force and the moment arm are determined by:

$$\theta = \psi - \text{atan}\left(\frac{x_d}{y_d}\right) \tag{3.60}$$

$$R_{eff} = x_{off}\frac{\cos(\theta)}{\cos(\phi_0)}. \tag{3.61}$$

The spring force for each spring is:

$$F_s = k(L_s - L_0) \tag{3.62}$$

where L_0 is the unstretched length of the spring.

An updated free body diagram is provided in Fig. 3.21. With the springs included in the system, the total moment is updated to include the additional moments due to the spring forces. Now, summing of the moments about the pivot point yields:

$$M_{0,tot} = F_a R_{eff,a} - F_p R_{eff,p} - F_{s1} R_{eff,s1} + F_{s2} R_{eff,s2}. \tag{3.63}$$

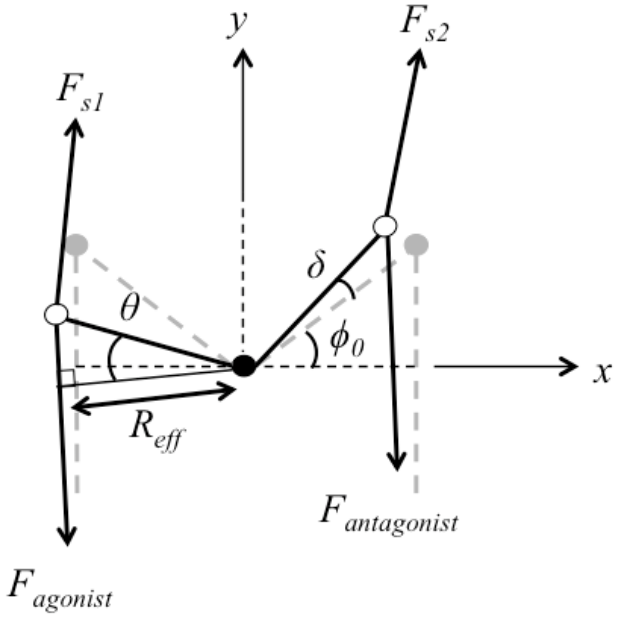

Figure 3.21. Free body diagram for bidirectional actuator with bell crank mechanism and extension springs.

To find the equilibrium angle, δ^*, of the system for a given actuation pressure, the angular acceleration of the system is set equal to zero and numerically solved for the equilibrium displacement angle using the updated expression for $M_{0,tot}$, which is a function of the actuation pressure and displacement angle:

$$\ddot{\delta}^* = \frac{M_{0,tot}(P, \delta^*)}{I_0} = 0. \tag{3.64}$$

3.4.4. Comparison of Model to Experimental Results

The experimental data and model predictions for the equilibrium angle and corresponding agonist and antagonist bundle forces at pressures of 20, 40, 60, and 80 psi are provided in Tables 3.4-5. The model predictions are provided for the model developed using the original miniature PAM force model of the average experimental data without the corrections for hysteresis, and for the model developed using the updated miniature PAM force model to account for the hysteresis.

Table 3.4: Equilibrium angle versus agonist bundle actuation pressure determined through experiment and predicted through modeling with and without considering the hysteresis in the miniature PAM actuation behavior.

Pressure (psi)	Equilibrium Angle (°)		
Nominal	Experiment	Model	
		Without hysteresis	With hysteresis
80	5.7	6.0	5.5
60	4.8	5.2	4.8
40	3.7	4.1	3.8
20	2.1	2.5	2.5

Table 3.5: Equilibrium agonist and antagonist bundle forces versus agonist bundle actuation pressure determined through experiment and predicted through modeling with and without considering the hysteresis in the miniature PAM actuation behavior.

Pressure (psi)	Equilibrium Agonist Bundle Force (lb)			Equilibrium Antagonist Bundle Force (lb)		
Nominal	Experiment	Model		Experiment	Model	
		Without hysteresis	With hysteresis		Without hysteresis	With hysteresis
80	16.7	18.6	16.9	17.6	21.7	19.5
60	12.5	13.0	11.7	12.8	14.9	13.2
40	8.0	7.1	6.3	7.8	8.0	7.0
20	4.0	1.3	1.1	3.7	1.3	1.1

When the nonlinear force balance model for the average miniature PAM actuation behavior is used, the model of the quasi-static behavior of the bidirectional actuator over predicts the equilibrium angle and the force values at equilibrium when compared to the experimental results. Adding a friction term to account for the hysteresis and assuming the agonist bundle operates on the unloading portion of the hysteresis curve and the antagonist bundle operates on the loading portion of the hysteresis curve during pressurization reduces the predicted equilibrium angle and corresponding equilibrium force values closer to those determined through experimental testing. The following results are presented for only the model with hysteresis correction.

Even with the hysteresis model, the individual miniature PAM model force predictions are less accurate at lower pressures, under predicting the experimental force values. This likely explains why the model force predictions are lower and the equilibrium angle is less accurate for the 20 psi case. Additionally, there is likely some torsional friction in the system, especially at the bearing locations for the pivot shaft and the pivot points on the bell crank. This torsional friction would resist the angular displacement of the system, which would slightly increase the agonist force and decrease the antagonist force at the equilibrium positions. The system may also not be starting at an equilibrium angle of exactly zero degrees, but having a non-zero initial displacement angle has a minimal effect on the results for small initial displacement angles.

The experimental data and model predictions for the equilibrium angle and bundle forces for the system with springs are provided in Table 3.6. Here, the spring constant for each spring was measured to be 4.55 lb/inch and the resting length of each spring was 4.5 inches. As in the case without the springs, the model is worse at lower pressures. For the 60 and 80 psi cases, the model predicts the experimental equilibrium angle within 0.3 degrees and the corresponding equilibrium forces within 1.4 lb.

Table 3.6: Equilibrium angle and forces versus agonist bundle actuation pressure determined through experiment and predicted through modeling for a bidirectional actuator with springs providing an applied torque.

Pressure (psi)	Equilibrium Angle (°)		Equilibrium Agonist Bundle Force (lb)		Equilibrium Antagonist Bundle Force (lb)	
Nominal	Experiment	Model	Experiment	Model	Experiment	Model
80	5.0	5.2	16.4	17.7	16.0	15.9
60	4.1	4.4	12.4	12.4	11.7	10.3
40	2.9	3.4	8.1	7.0	7.3	4.9
20	1.3	2.2	4.0	1.6	3.5	0

Experimental data was also collected with an initial extension in each bundle. To update the model for this scenario, the initial force readings from the load cells in the unpressurized system (F_a = 1.5 lb, F_p = 1.7 lb) were recorded. These readings were used to estimate the initial extension in each bundle from their corresponding antagonist force versus contraction models. When the bundle length at a given displacement angle is calculated, the initial extension length is added to the resting length of the bundle before the change in length at the given displacement angle is subtracted to find the current length. The data for this case is provided in Table 3.7. This process increases the forces in each bundle and reduces the equilibrium angle at each pressure from the experimental results from Tables 3.4-5. Here, the model is predicts the experimental angle within 0.4 degrees at the higher measured pressures, and the corresponding forces within 1.8 lb.

Table 3.7: Equilibrium angle and forces versus agonist bundle actuation pressure determined through experiment and predicted through modeling for a bidirectional actuator with an initial extension in the miniature PAM bundles.

Pressure (psi)	Equilibrium Angle (°)		Equilibrium Agonist Bundle Force (lb)		Equilibrium Antagonist Bundle Force (lb)	
Nominal	Experiment	Model	Experiment	Model	Experiment	Model
80	5.1	4.7	18.7	20.5	23.5	23.2
60	4.3	4.1	14.2	14.8	17.4	16.4
40	3.2	3.2	9.6	9.0	11.5	9.8
20	1.8	2.0	5.1	3.4	5.8	3.6

Using the model for the bidirectional actuator, the equilibrium conditions of the system are compared for different combinations of miniature PAMs operated at different actuation pressures. In Table 3.8, each bundle is assumed to have eight miniature PAMs, which are the eight miniature PAMs described in Table 3.1 that have been used throughout this study. In the four active PAM case, the agonist bundle is assumed to be

the agonist bundle specified in Section 3.3.3: miniature PAMs #2, 4, 7, and 8. In the two active PAM case, the agonist bundle is assumed to be PAMs #4 and 8. The behavior for each case will vary slightly depending on the combination of miniature PAMs included in each bundle; however, the general trends should be consistent.

In Table 3.8, the equilibrium angle and corresponding forces are predicted using the bidirectional actuator model for two energy equivalent cases. In the first case, eight active agonist miniature PAMs actuated at half-pressure are expected to achieve an equilibrium angle of 3.6°, compared to the 4.3° achieved by four active agonist miniature PAMs actuated at full-pressure. Similarly, four active agonist miniature PAMs actuated at half-pressure are expected to achieve an equilibrium angle of 3.3°, compared to the 3.7° achieved by two active agonist miniature PAMs actuated at full-pressure. The bidirectional actuator system can achieve higher deflection angles when operated at higher pressures in energy equivalent configurations because there are fewer energy losses in the system. The corresponding equilibrium forces are higher when the agonist bundles are operated at higher pressures.

Table 3.8: Equilibrium angle and forces versus agonist bundle actuation pressure and number of active agonist miniature PAMs for energy equivalent configurations.

No. Agonist PAMs	No. Antagonist PAMs	Pressure (psi)	Equilibrium Angle (°)	Equilibrium Agonist Bundle Force (lb)	Equilibrium Antagonist Bundle Force (lb)
8	8	40	3.6	10.5	11.6
4	8	80	4.3	19.4	21.7
4	8	40	3.3	7.2	7.8
2	8	80	3.7	11.2	12.3

3.5. Conclusions

PAMs are unidirectional actuators that can be operated in an antagonistic pair configuration to produce bidirectional motion. This study considered the antagonist behavior of a bundle of miniature PAMs and the quasi-static behavior of two bundles of miniature PAMs in an agonist-antagonist configuration. The antagonist behavior of a bundle of miniature PAMs can be modeled by summing the force versus contraction profiles of the individual miniature PAMs included in a bundle after applying a shift in the curves based on the length variations between the miniature PAMs in the bundle. This model applies to both agonist and antagonist behavior. The percent error for the ideal model, generated by summing the actuation behavior of the individual miniature PAMs without applying the shift to account for length variations, and the percent loss from the ideal model to the corrected model are much higher for antagonistic behavior than the agonistic behavior due to the high passive stiffness of PAMs as they are extended past their natural resting length.

In this study, a bidirectional actuator was designed to allow for the characterization and modeling of the bidirectional behavior of two bundles of miniature PAMs operated in an agonist-antagonist configuration. Pressure, angular displacement, agonist bundle force, and antagonist bundle force data were collected during the quasi-static operation of the bidirectional actuator. The quasi-static behavior was modeled using system geometry, with a modification to account for the different lengths of each PAM in the bundle when one bundle plate is held fixed and the other is allowed to rotate. Additionally, the individual miniature PAM models of the agonist and antagonist behavior were updated to account for the hysteresis in the miniature PAM experimental

data. The force variations due to this hysteresis account for a significant portion of the total bundle forces at the low-force operating range of the bidirectional actuator considered here.

A given angular displacement of the actuator corresponds to a specific contraction of the agonist bundle and extension of the antagonist bundle, which in turn correspond to specific agonist and antagonist force values for each bundle. The force versus contraction profiles of the bundles are functions of the force versus contraction profiles of the individual miniature PAMs in the bundles and the variation in lengths of the miniature PAMs in the bundle. The consideration of energy equivalent configurations illustrated the efficiency benefits of operating the fewest number miniature PAMs, at higher operating pressures, necessary to achieve a desired force or deflection.

Due to the high passive stiffness of PAMs as they are stretched passed their natural resting length, the achievable system deflection is limited, so researchers have looked into methods of improving the range by choosing appropriate mechanism through with PAMs generate the system deflection and by introducing a bias contraction and pressure. To improve the performance of the bidirectional actuator considered here, the dimensions of the bell crank mechanism could be optimized, and a bias contraction could be introduced to the system. A bias pressure would then be needed to ensure joint stiffness. Improvements to the miniature PAM fabrication process to reduce the length variation in the miniature PAMs would correspond to an increase in both the agonist and antagonist forces at a given contraction or extension.

The next step in the research should be to conduct dynamic testing of the bidirectional actuator to see how the agonist-antagonist configuration of two bundles of

miniature PAMs performs dynamically. Some necessary modeling considerations to predict this dynamic behavior would include the airflow dynamics and heat transfer at the valve orifices, the thermodynamics and compressibility of the pressurized air inside the PAMs during actuation, and the losses, inertia, stiffness, and experimentally-determined damping in the system (Kang *et al.* 2009, Robinson *et al.* 2014, Woods *et al.* 2014).

4. Space Qualified Pneumatic Artificial Muscles

4.1. Introduction

4.1.1. Application of PAMs to Space Robotics

Pneumatic artificial muscles (PAMs), or McKibben artificial muscles, are lightweight, naturally compliant actuators that behave like human muscles. A PAM consists of bladder made from elastomeric tubing, surrounded by a braided sleeve, and sealed with an end fitting attachment at each end. When pressurized through one of its two end fittings, a PAM expands radially and contracts axially, generating a pulling force in the axial direction. PAMs produce their maximum force when held at their resting state (blocked force) and zero force after being allowed to fully contract to their actuated state (free contraction). Figure 4.1 shows a PAM being held at its blocked force and free contraction states.

PAMs are used in robotic manipulators, including robotic hands (Boblan *et al.* 2003, Röthling *et al.* 2007), arms (Tondu *et al.* 2005, Robinson *et al.* 2011), and legs (Colbrunn 2000, Vermeulen 2006). Researchers have developed pneumatically actuated power assist devices for hand gripping (Sasaki *et al.* 2004, Tadano *et al.* 2010, Wu *et al.* 2010) and arm actuation (Ying *et al.* 2007), which could be applied to improve the mobility of hands and arms in pressure suits (Salmoiraghi and Akin 2012). Pillsbury *et al.* (2015) considered the use of miniature PAMs to pneumatically power an extra-vehicular activity (EVA) glove exoskeleton to improve the dexterity of astronauts wearing EVA gloves.

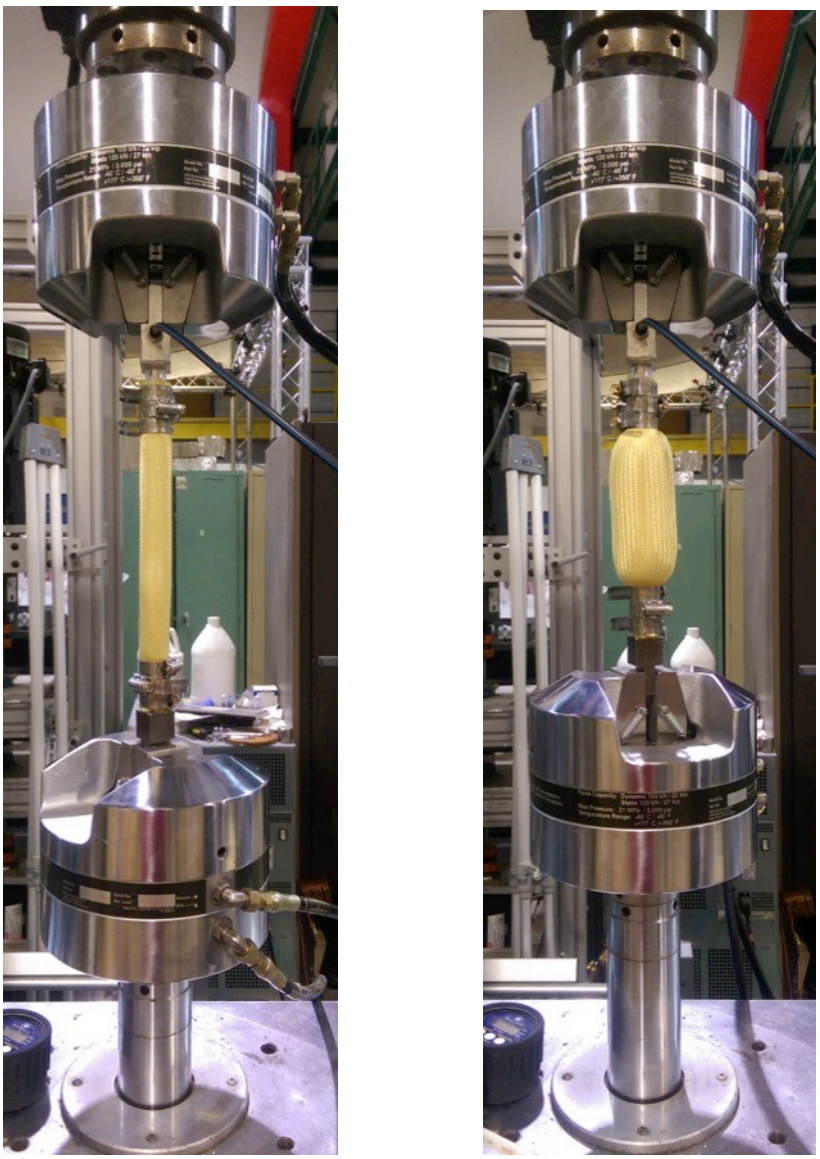

(a) Blocked Force (b) Free Contraction

Figure 4.1: The blocked force and free contraction states of a PAM with a Latex Rubber Tubing (1" OD, ¾" ID) bladder and Kevlar (1.5" nominal OD) braided sleeve.

There are numerous applications for robotics in space, examples of which include rovers, the Space Shuttle Robotic Manipulator System, and the International Space Station Mobile Servicing System. A review of space robotics is provided by Wilcox *et al.* (2006). However, little prior research has been completed on the use of PAMs as actuators for space robotics.

Key benefits of PAMs include their high power-to-weight ratios and specific work at low actuation pressures (Chou and Hannaford 1994, Robinson *et al.* 2011, Vocke *et al.* 2012). PAMs have a simple structure that can be assembled from commercially available materials. Additionally, PAMs have been endurance-tested for over 120 million loading cycles with minimal wear and without any noticeable performance degradation (Woods *et al.* 2012). Although the range of acceptable bladder and braided sleeve materials would be limited for space-qualified PAMs, the high power-to-weight ratios and specific work offer potential weight-savings benefits over traditional electric motors. Additionally, the excellent durability and fatigue-resistance properties of PAMs would be beneficial for longer duration space robotics missions.

4.1.2. Space Qualified Materials

To utilize PAMs in space robotics, researchers must determine the appropriate choice of space-qualified materials for the components of PAMs. An overview of the necessary considerations when selecting materials for use in space is provided by Finckenor and de Groh (2015) in *Space Environment Effects* from the International Space Statin Researcher's Guide Series published by the NASA ISS Program Sciences Office. Materials in space are exposed to vacuum, radiation, atomic oxygen, thermal cycling, contamination, and impacts from debris. NASA maintains a handbook that overviews the appropriate measures for conducting material testing at ground facilities: GEVS-SE Rev A General Environmental Verification Specification for STS & ELV Payloads, Subsystems and Components.

The vacuum in space will cause outgassing, or the release of gasses trapped in materials, which can result in contamination of other nearby surfaces (Finckenor and de

Groh 2015). NASA's Materials and Processes Technical Information System (MAPTIS) includes the Materials Selection Database and Satellite Contamination and Materials Outgassing Knowledgebase, which provide information on low outgassing materials with testing results from ASTM E595, Standard Test Method for Total Mass Loss and Collected Volatile Condensable Materials from Outgassing in a Vacuum Environment, and ASTM E1559, Standard Test Method for Contamination Outgassing Characteristics of Spacecraft Materials.

In space, materials are exposed to extreme temperatures and thermal cycling. The range of temperatures and rate of cycling for a material depend on numerous factors, including its orbit, thermo-optical properties, time exposure to sunlight and shadow, and it's views of the Sun, Earth, and other spacecraft surfaces (Dever *et al.* 2005). Dever *et al*. (2005) provide a review of the effects of thermal cycling on different materials.

Atomic oxygen is abundant in low Earth orbit (LEO). It is formed through interactions of diatomic oxygen with short-wavelength ultraviolet radiation from the sun, and survives in the low atmospheric density environment of LEO. Atomic oxygen can cause significant erosion and degradation of materials. Protective coatings, when applied correctly to minimize the chances of contamination or cracking, can help protect materials from interaction with atomic oxygen (Banks *et al.*, 2004). ASTM E2089, Standard Practices for Ground Laboratory Atomic Oxygen Interaction Evaluation of Materials for Space Applications, provides guidelines for ground laboratory analysis of material interaction with atomic oxygen.

In the following study, the actuation behavior of PAMs assembled from candidate bladder and braided sleeve materials for use in space are characterized. This work is

being done in conjunction with materials selection and mass loss testing conducted at the Naval Research Laboratory in Washington, DC. The goal of the present research is to assess whether PAMs assembled from candidate space qualified materials are able to handle the loads and performance requirements for space robotics, and to compare the relative actuation performance of different bladder and braided sleeve materials. Additional mass loss testing, temperature range evaluations, and thermal cycling would need to be conducted to further assess the space qualified nature of the PAMs.

4.2. Bladder Comparisons

Our research group has previously used the Super-Soft Latex Rubber Tubing and Kevlar Braided Sleeve (1420 Denier Kevlar 49) as one of our standard pairs of bladder and braided sleeve for pneumatic artificial muscles. To assess the performance of candidate space qualified bladder and braided sleeve materials, a Latex Rubber Tubing bladder with a 1" outer diameter and a ¾" inner diameter is used as the reference bladder and a Kevlar Braided Sleeve with a 1.5" nominal outer diameter is used as the reference braided sleeve. A picture of the reference PAM is provided in Fig. 4.2.

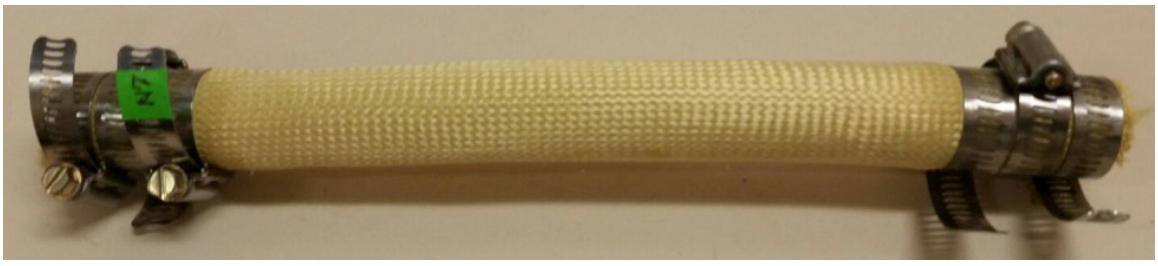

Figure 4.2: PAM with a Latex Rubber Tubing (1" OD, ¾" ID) bladder and Kevlar (nominal 1.5" OD) braided sleeve.

The bladder materials compared in this study are listed in Table 4.1. The first entry is the standard bladder material for reference. The additional materials compared are Viton Fluoroelastomer Tubing and Pharma-50 Silicone Tubing. The Viton Fluoroelastomer Tubing was tested for two different outer diameters and thicknesses: 1" outer diameter with a 1/8" wall thickness and a 7/8" OD with a 1/16" wall thickness. The Pharma-50 Silicone Tubing had a 7/8" OD and a 1/8" wall thickness. Both candidate materials had slightly higher Shore Hardness values than the standard Latex Tubing, but were still sufficiently soft to utilize as PAM bladders. A picture of the bladder materials is provided in Fig. 4.3. Other bladder materials considered included Tygon Tubing, Platinum-Cured Silicone Tubing, and Platinum-Cured BioPharm Silicone Tubing. However, these materials were too stiff to use as bladders for PAMs.

Table 4.1: Bladder Materials.

Material	OD (in.)	ID (in.)	Shore Hardness	Temperature Range (°F)
Latex Rubber Tubing	1	3/4	Soft (Durometer 40A)	0 – 150 °F
Viton Fluoroelastomer Tubing	1	3/4	Soft (Durometer 60A)	-10 – 400 °F
Viton Fluoroelastomer Tubing	7/8	3/4	Soft (Durometer 60A)	-10 – 400 °F
Pharma-50 Silicone Tubing	7/8	5/8	Soft (Durometer 50A)	-60 – 460 °F

(a) Latex (b) Viton (7/8" OD) (c) Viton (1" OD) (d) Pharma-50

Figure 4.3: Bladder materials.

Each PAM was assembled from a Kevlar Braided Sleeve with a 1.5" nominal outer diameter. The braided sleeve was pulled tight over the bladders during assembly to maximize the braid angle and resulting blocked force of the PAMs. The braided sleeve, bladder, and end fittings were attached with epoxy and hose clamps. The properties for each PAM are provided in Table 4.2.

Table 4.2. Properties of PAMs used in bladder comparison.

Bladder Material	Resting Length (in.)	Braid Angle Prediction (°)	Blocked Force @ 90 psi (lb)	Free Contraction @ 90 psi (%)
Latex Rubber Tubing (1" OD, ¾" ID)	7 13/16	69	954	30.4
Pharma-50 Silicone Tubing (7/8" OD, 5/8" ID)	7 7/8	71	958	26.4
Viton Fluoroelastomer Tubing (1" OD, ¾" ID)	7 3/4	68.5	898	22.1
Viton Fluoroelastomer Tubing (7/8" OD, ¾" ID)	7 7/16	70.5	1059	30.8

The average length of the four PAMs used for the bladder comparison is 7 7/32 in. with a standard deviation of 0.1943 in. Kothera *et al.* (2009) showed that the blocked force and free contraction ratios are independent of length (free contraction increases linearly with length). Thus, for the small variation in lengths considered here, the experimental results are comparable. A significant variation in lengths could affect the experimental results due to the non-cylindrical shape of the PAMs near the end fittings—the tip effects would have a more significant influence on PAM actuation behavior for shorter PAMs.

Quasi-static testing was completed in 15 psi increments from 30 to 90 psi. Displacement and force data were collected using a 22 kip MTS servo-hydraulic test

machine. Data was collected for each PAM over the course of three complete cycles from its blocked force state to its free contraction state and back to its blocked force state. The force versus contraction profiles for each of the four PAMs are provided in Figs. 4.4-6. Additionally, the average experimental data from testing at 60 and 90 psi are provided in Fig. 4.7.

The 7/8" OD Viton Fluoroelastomer Tubing had the best performance with the highest blocked force and free contraction values. The Latex Rubber Tubing and Pharma-50 Silicone Tubing both had similar blocked force performance, with approximately a 10% reduction in total blocked force at 90 psi from the 7/8" OD Viton Fluoroelastomer Tubing. The 1" OD Viton Fluoroelastomer Tubing performed worst, with a 15% reduction in total blocked force at 90 psi. The Latex Rubber Tubing achieved comparable free contraction values to the 7/8" OD Viton Fluoroelastomer Tubing at higher pressures, while the Pharma-50 Silicone Tubing and the 1" OD Viton Fluoroelastomer Tubing achieved less free contraction. The Pharma-50 Silicone Tubing had a free contraction 14% less than that 7/8" OD Viton Fluoroelastomer Tubing, while the 1" OD Viton Fluoroelastomer Tubing achieved 28% less free contraction.

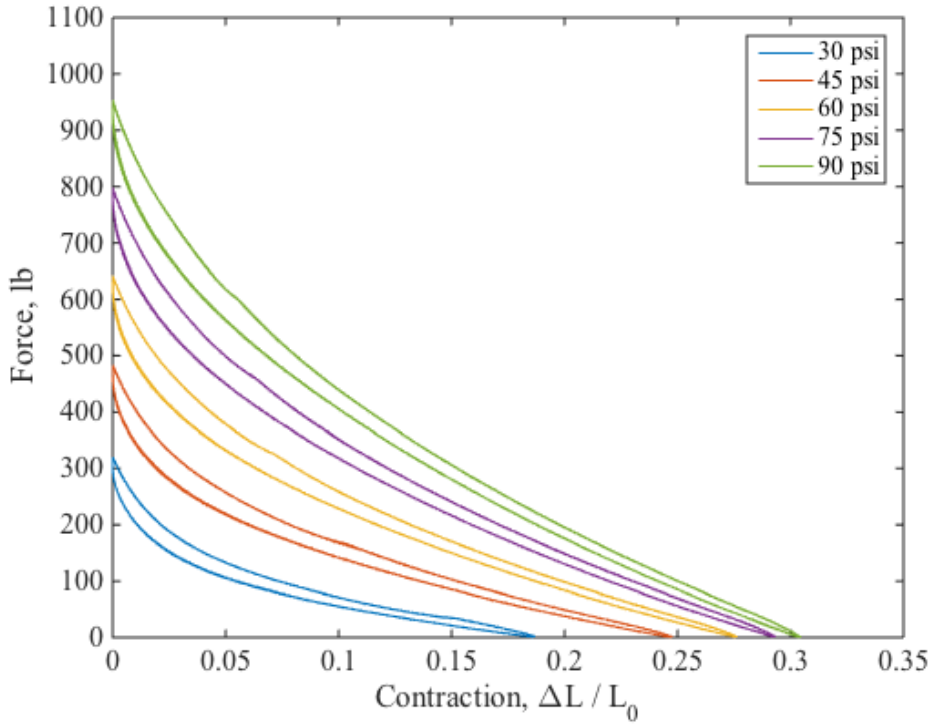

Figure 4.4: Experimental data for the force versus contraction profiles of pneumatic artificial muscles with a Latex Rubber (1" OD, ¾" ID) bladder and a Kevlar (nominal 1.5" OD) braided sleeve.

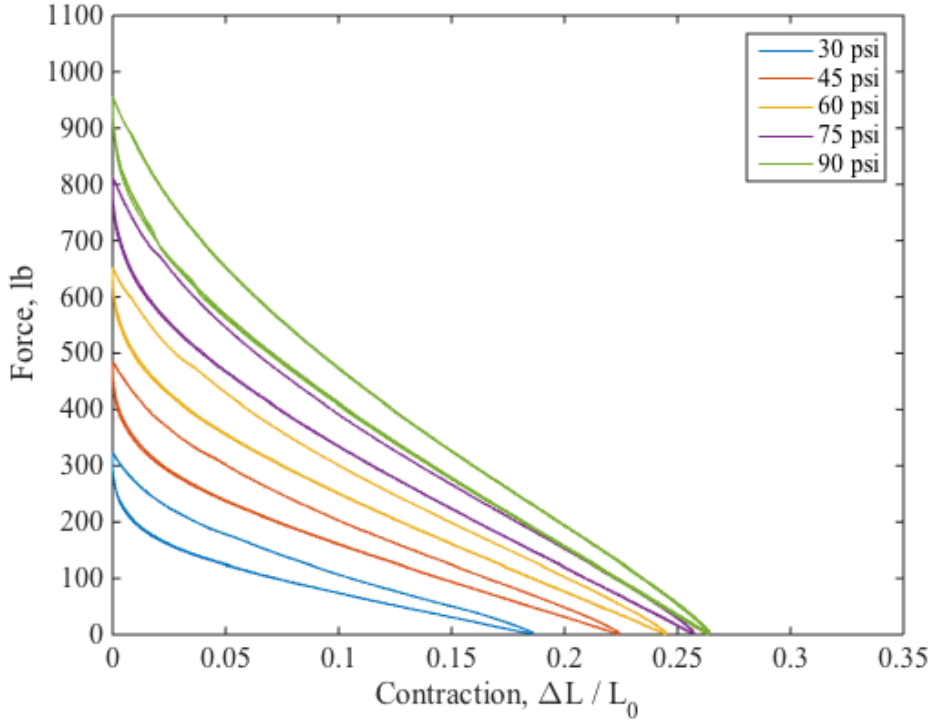

Figure 4.5: Experimental data for the force versus contraction profiles of pneumatic artificial muscles with a Pharma-50 Silicone (7/8" OD, 5/8" ID) bladder and a Kevlar (nominal 1.5" OD) braided sleeve.

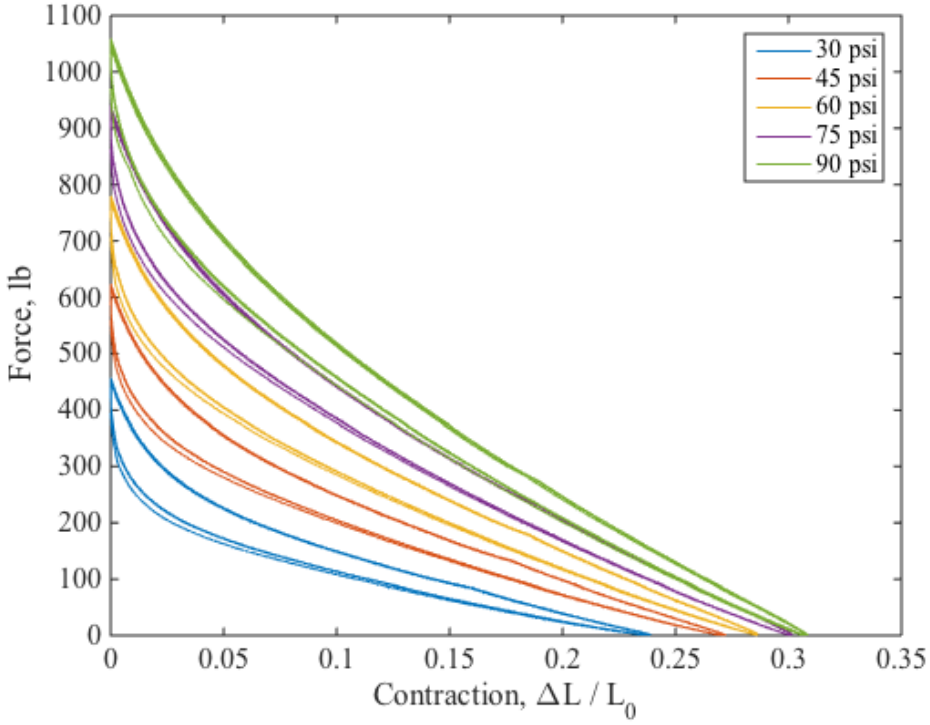

(a) Viton Fluoroelastomer (7/8” OD, ¾” ID)

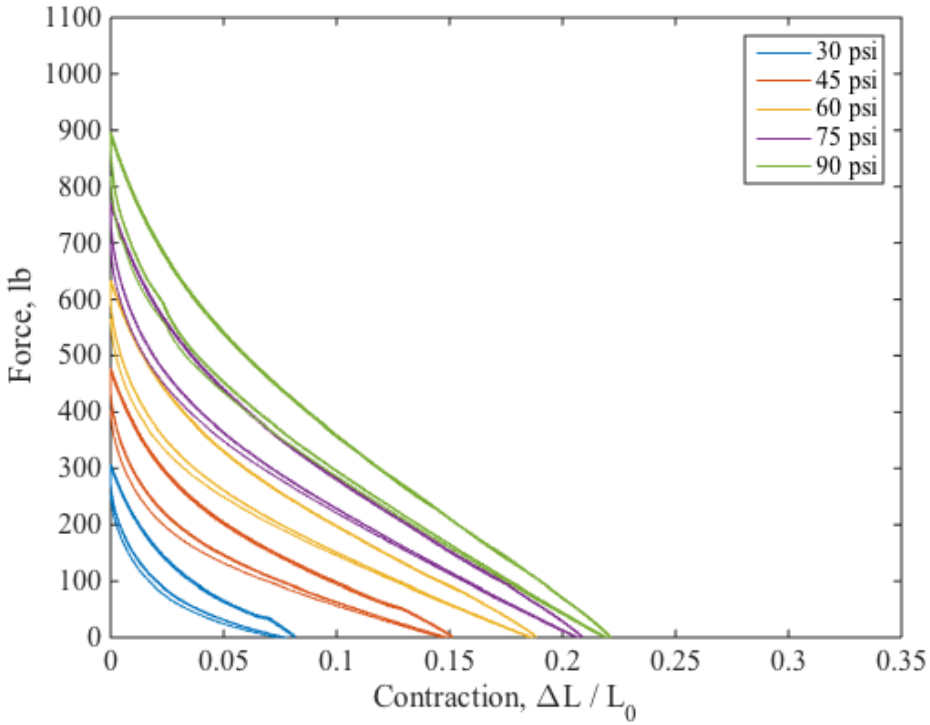

(b) Viton Fluoroelastomer (1” OD, ¾” ID)

Figure 4.6: Experimental data for the force versus contraction profiles of pneumatic artificial muscles with a (a) Viton Fluoroelastomer (7/8” OD, ¾” ID) and (b) Viton Fluoroelastomer (1” OD, ¾” ID) bladder and a Kevlar (nominal 1.5” OD) braided sleeve.

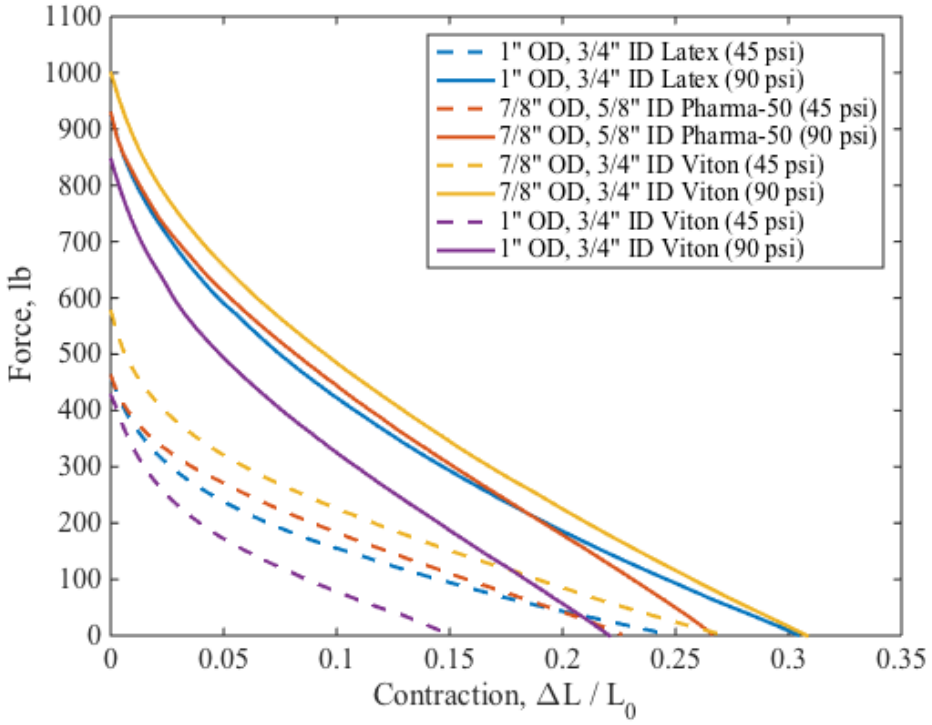

Figure 4.7: Average experimental data for the force versus contraction profiles of pneumatic artificial muscles with Latex, Pharma-50, and Viton (7/8" OD and 1" OD) bladders and a nominal 1.5" OD Kevlar braided sleeve.

There is hysteresis the PAM data, which is a consequence of internal friction in PAMs (Chou and Hannaford 1996, Davis and Caldwell 2006). The bottom half of each curve is the unloading portion (from blocked force to free contraction) and the top half is the loading portion (from free contraction to blocked force). A comparison of the hysteresis in the PAM data for the different bladder materials at each test pressure, 30 – 90 psi is provided in Table 4.3. The data is compared using a hysteresis ratio, which is determined as follows:

$$Hysteresis\ ratio = \left| \frac{\int_{BF}^{FC} F_{unloading}\, dl + \int_{FC}^{BF} F_{loading}\, dl}{\int_{BF}^{FC} F_{unloading}\, dl} \right| \tag{3.27}$$

where BF is the blocked force state (zero contraction) and FC is the free contraction state. $F_{loading}$ is the force along the loading (upper) portion of the force versus contraction curve and $F_{unloading}$ is the unloading (lower) portion of the force versus contraction curve.

The data from the PAM with Latex Rubber Tubing bladder has the least amount of hysteresis. The hysteresis in the Pharma-50 Silicone Tubing and the 7/8" OD Viton Fluoroelastomer Tubing are comparable across the range of pressures, and the 1" OD Viton Fluoroelastomer Tubing experienced the most hysteresis.

Table 4.3: PAM hysteresis data—bladder comparison with Kevlar braided sleeve (nominal 1.5" OD).

	Hysteresis Ratio				
Bladder Material	30 psi	45 psi	60 psi	75 psi	90 psi
Latex Rubber Tubing (1" OD, ¾" ID)	0.28	0.19	0.15	0.12	0.10
Pharma-50 Silicone Tubing (7/8" OD, 5/8" ID)	0.44	0.28	0.22	0.19	0.17
Viton Fluoroelastomer Tubing (1" OD, ¾" ID)	0.85	0.52	0.34	0.27	0.25
Viton Fluoroelastomer Tubing (7/8" OD, ¾" ID)	0.41	0.28	0.23	0.19	0.18

4.3. Braided Sleeve Comparisons

The braided sleeve materials compared in this study are listed in Table 4.4. The first entry is the standard Kevlar braided sleeve with a 1.5" nominal outer diameter for reference. The additional materials compared are Kevlar braided sleeve with a 2" nominal outer diameter, Vectran LCP braided sleeve with a 1.5" nominal outer diameter, and Vectran LCP braided sleeve with a 2" nominal outer diameter. A picture of the braided sleeve materials is provided in Fig. 4.8.

Table 4.4: Braided Sleeve Materials

Material	Nominal OD	Denier	Nominal Wall Thickness
Kevlar Braided Sleeve	1.5”	1420	0.012”
Kevlar Braided Sleeve	2”	1420	0.011”
Vectran Braided Sleeve	1.5”	1500	0.020”
Vectran Braided Sleeve	2”	n/a	0.040”

(a) Kevlar (1.5” OD) (b) Kevlar (2” OD) (c) Vectran (1.5” OD) (d) Vectran (2” OD)

Figure 4.8: Braided sleeve materials.

Each PAM was assembled with Latex Rubber Tubing with a 1” outer diameter and a ¾” inner diameter. Each braided sleeve was pulled tight over its bladder during assembly to maximize the braid angle. The properties for each PAM are provided in Table 4.5.

Table 4.5. Properties of PAMs used in braided sleeve comparison.

Braided Sleeve Material	Resting Length (in.)	Braid Angle Prediction (°)	Blocked Force @ 75 psi (lb)	Free Contraction @ 75 psi (%)
Kevlar Braided Sleeve (1.5” OD)	7 13/16	69	800	30.2
Kevlar Braided Sleeve (2.0” OD)	7 3/8	70	1220	31.3
Vectran Braided Sleeve (1.5” OD)	7 3/4	72	1241	29.6
Vectran Braided Sleeve (2.0” OD)	7 1/4	65.5	753	23.8

Quasi-static testing was completed in 15 psi increments from 30 to 75 psi. The force versus contraction profiles for each of the four PAMs are provided in Figs. 4.9-10. Additionally, the average experimental data from testing at 45 and 75 psi are provided in Fig. 4.11. The PAMs assembled with 2" OD Kevlar and 1.5" OD Vectran braided sleeves achieved similar performance and out-performed the PAMs assembled with the 1.5" OD Kevlar and the 2" OD Vectran braided sleeves. The latter two PAMs achieved similar blocked force readings; however, the 1.5" OD Kevlar PAM's free contraction values were comparable to those of the 2" OD Kevlar and 1.5" OD Vectran, while the PAM with the 2" OD Vectran had the worst free contraction performance.

A comparison of the hysteresis in the PAM data for the different braided sleeve materials is provided in Table 4.6. The data is compared using the hysteresis ratio from Eqn. 3.1.

The hysteresis in the PAM with the 1.5" OD Kevlar braided sleeve was the lowest, while the hysteresis in the 2" OD Vectran braided sleeve was the highest. The hysteresis in the 2" OD Kevlar and 1.5" OD Vectran braided sleeves were comparable and close to that of the 1.5" OD Kevlar braided sleeve.

Table 4.6: PAM hysteresis data—braided sleeve comparison with Latex Rubber Tubing (1" OD, ¾" ID) bladder.

	Hysteresis Ratio			
Braided Sleeve Material	30 psi	45 psi	60 psi	75 psi
Kevlar Braided Sleeve (1.5" OD)	0.25	0.18	0.15	0.12
Kevlar Braided Sleeve (2.0" OD)	0.31	0.20	0.17	0.12
Vectran Braided Sleeve (1.5" OD)	0.38	0.26	0.22	0.20
Vectran Braided Sleeve (2.0" OD)	0.56	0.39	0.35	0.35

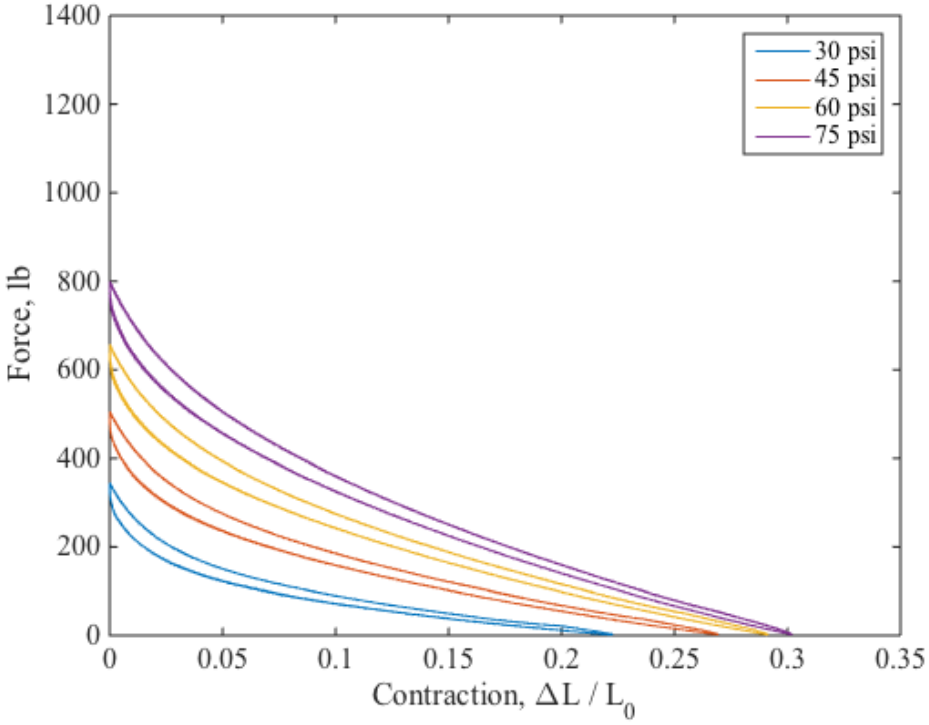

(a) Kevlar (1.5” OD)

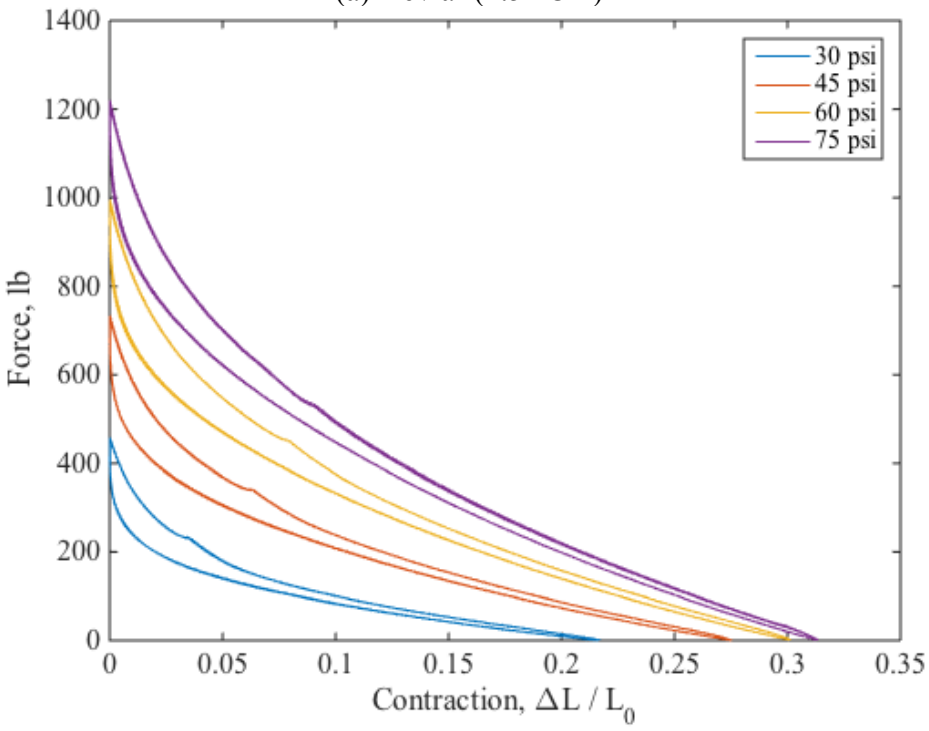

(b) Kevlar (2” OD)

Figure 4.9. Experimental data for the force versus contraction profiles of pneumatic artificial muscles with a (a) Kevlar (1.5” OD) and (b) Kevlar (2” OD) braided sleeves and a Latex Rubber Tubing (1” OD, ¾” ID) bladder.

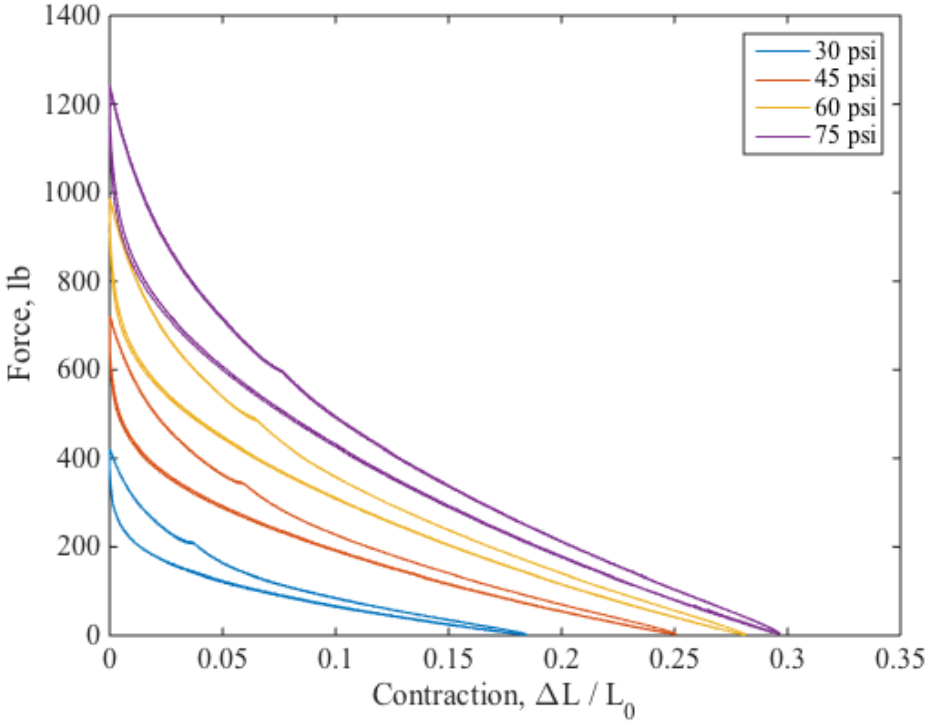

(a) Vectran (1.5” OD)

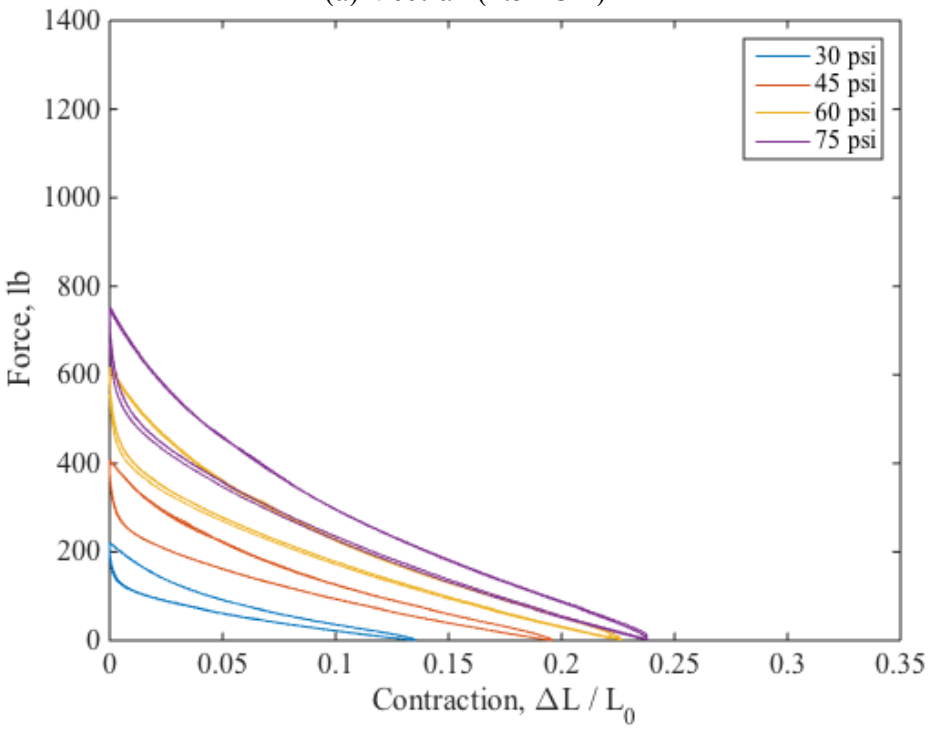

(b) Vectran (2.0” OD)

Figure 4.10. Experimental data for the force versus contraction profiles of pneumatic artificial muscles with a (a) Vectran (1.5” OD) and (b) Vectran (2” OD) braided sleeves and a Latex Rubber Tubing (1” OD, ¾” ID) bladder.

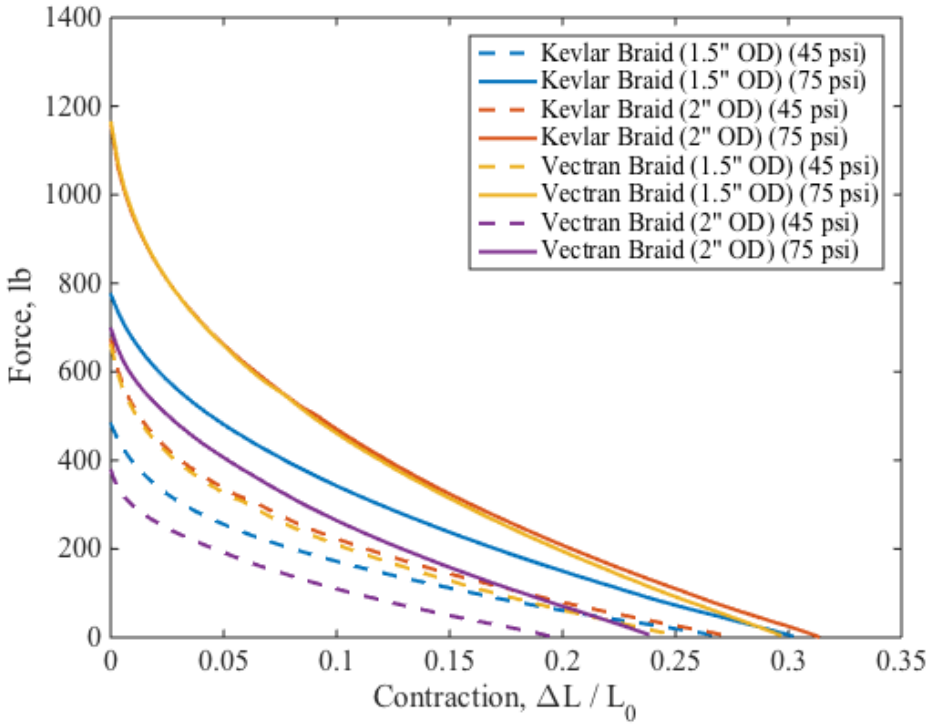

Figure 4.11. Average experimental data for the force versus contraction profiles of pneumatic artificial muscles with Kevlar (1.5” and 2” OD) and Vectran (1.5 and 2” OD) braided sleeves and a Latex Rubber Tubing (1” OD, ¾” ID) bladder.

4.4. Pairing of the Top-Performing Bladder and Braided Sleeve Materials

4.4.1. Bladder and Braided Sleeve Materials

For the final PAM comparisons, the material used for the braided sleeve is 1500 Denier Vectran T97 with a 1.5” nominal OD. This braided sleeve was one of the top two performing candidates from the braided sleeve comparisons and performed better than the Kevlar braided sleeve during mass loss testing.

Each bladder from the bladder comparison performed well, except the Viton Fluoroelastomer Tubing with the 1” OD and ¾” ID. The Latex Rubber Tubing (1” OD, ¾” ID), Pharma-50 Silicone Tubing (7/8” OD, 5/8” ID), and Viton Fluoroelastomer Tubing (1” OD and 7/8” ID) are now paired with the Vectran braided sleeve. Here, the

Viton Fluoroelastomer Tubing has a 1” OD and 7/8” ID, which has the same thickness as the better-performing Viton bladder from Section 4.2, but the same OD as the reference Latex Rubber Tubing bladder. A summary of these bladder materials is provided in Table 4.7. A picture of the three bladder materials is provided in Figure 4.12.

Table 4.7: Bladder Materials.

Material	OD (in.)	ID (in.)	Shore Hardness	Temperature Range (°F)
Latex Rubber Tubing	1	3/4	Soft (Durometer 40A)	0 to 150
Viton Fluoroelastomer Tubing	1	7/8	Soft (Durometer 60A)	-10 to 400
Pharma-50 Silicone Tubing	7/8	5/8	Soft (Durometer 50A)	-10 to 400

(a) Latex (b) Viton (c) Pharma-50

Figure 4.12: Bladder materials

4.4.1.1. Latex Rubber Tubing

A picture of the PAM assembled with the Latex Rubber Tubing (1” OD, ¾” ID) bladder and the Vectran (nominal 1.5” OD) braided sleeve is provided in Fig. 4.13. The 1500 Denier Vectran braided sleeve is thicker than the 1420 Kevlar braided sleeve of the same outer diameter. This difference in thickness results in the braided sleeve being more difficult to pull tightly over the bladder, so the resultant PAM has a slightly looser

Vectran braided sleeve than the Kevlar braided sleeve shown in Fig. 4.2. However, the nominal 1.5” OD Vectran is still a good fit for the 1” OD Latex bladder. Testing images of the unpressurized PAM and the pressurized PAM at its blocked force and free contraction states are provided in Fig. 4.14.

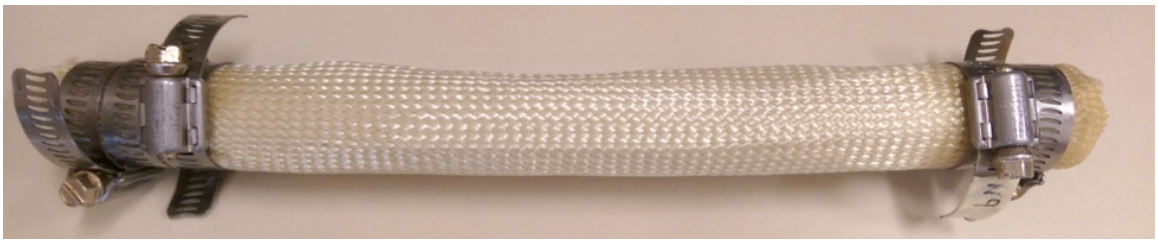

Figure 4.13: PAM with a Latex Rubber Tubing (1” OD, ¾” ID) bladder and Vectran (nominal 1.5” OD) braided sleeve.

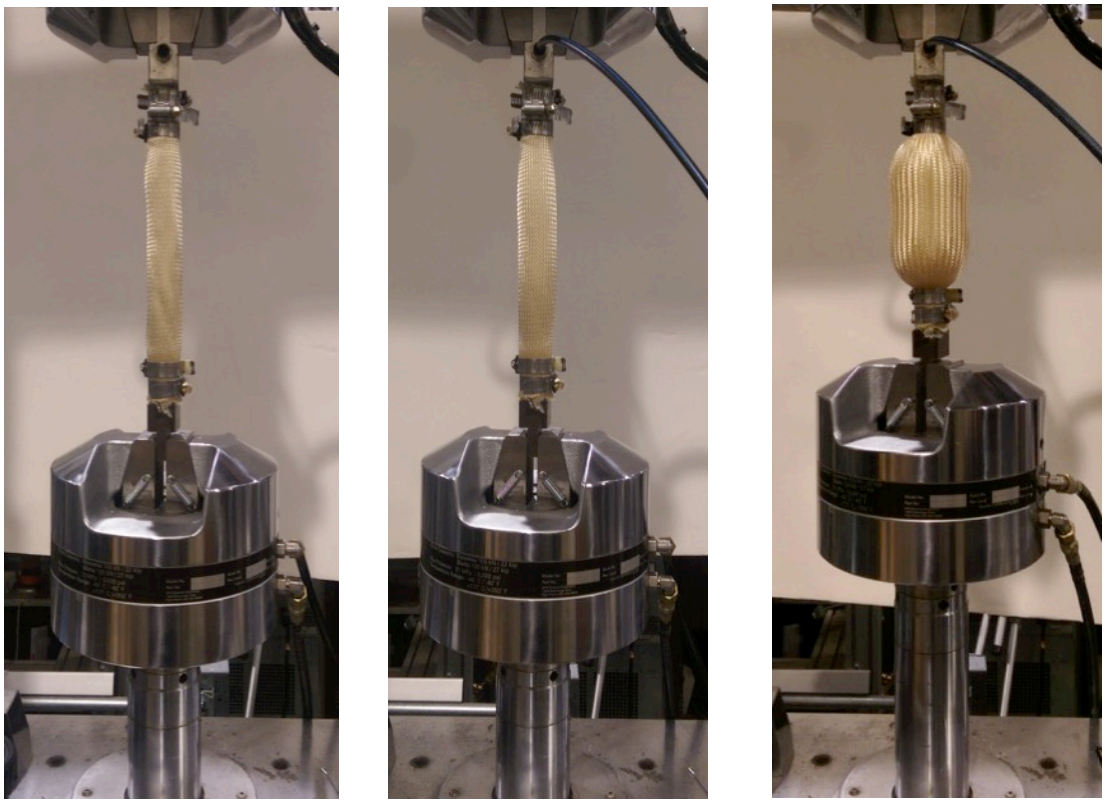

(a) Unpressurized (b) Blocked Force (c) Free Contraction

Figure 4.14: Quasi-static testing of a PAM with a Latex Rubber Tubing (1” OD, ¾” ID) bladder and Vectran (nominal 1.5” OD) braided sleeve.

4.4.1.2. Viton Fluoroelastomer Tubing

A picture of the PAM assembled with the Viton Fluoroelastomer Tubing (1” OD, 7/8” ID) bladder and the Vectran (nominal 1.5” OD) braided sleeve is provided in Fig. 4.15. Due to the non-cylindrical shape of the Viton bladder, as seen in Fig. 4.12, the PAM has a non-cylindrical shape in its unpressurized state, and the fit of the braid is loose. Testing images of the unpressurized PAM and the pressurized PAM at its blocked force and free contraction states are provided in Fig. 4.16. The shape of the PAM becomes cylindrical when pressurized.

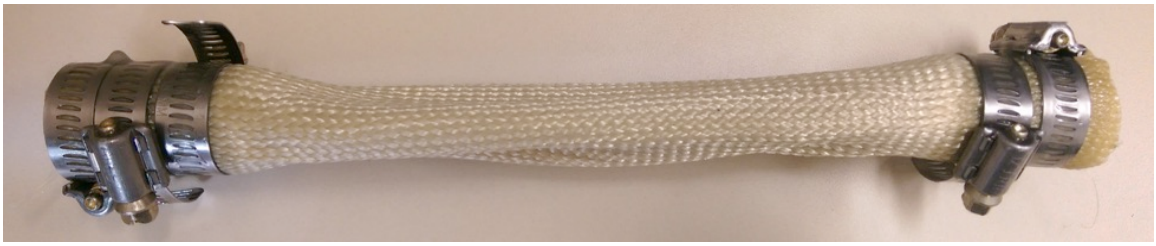

Figure 4.15. PAM with a Viton Fluoroelastomer Tubing (1” OD, 7/8” ID) bladder and Vectran (nominal 1.5” OD) braided sleeve.

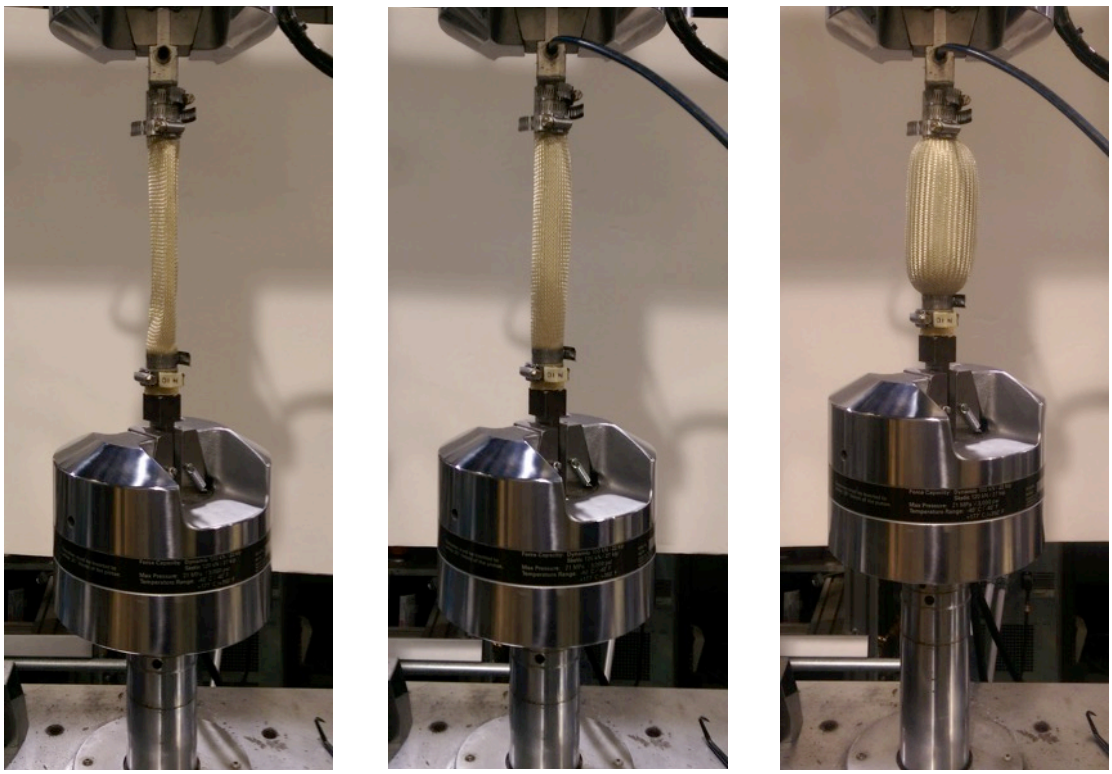

(a) Unpressurized (b) Blocked Force (c) Free Contraction

Figure 4.16: Quasi-static testing of a PAM with a Viton Fluoroelastomer Tubing (1” OD, 7/8” ID) bladder and a Vectran (nominal 1.5” OD) braided sleeve.

4.4.1.3. Pharma-50 Silicone Tubing

A picture of the PAM assembled with the Pharma-50 Silicone Tubing (7/8” OD, 5/8” ID) bladder and the Vectran (nominal 1.5” OD) braided sleeve is provided in Fig. 4.17. Because the outer diameter of the Pharma-50 tubing is smaller than that of the Latex Tubing (1” OD), the braided sleeve is looser on the assembled PAM with the Pharma-50 bladder. Testing images of the unpressurized PAM and the pressurized PAM at its blocked force and free contraction states are provided in Fig. 4.18. Due to the looseness of the braid, the bladder does expand some at the blocked force condition. This would slightly reduce the PAM’s achievable blocked force.

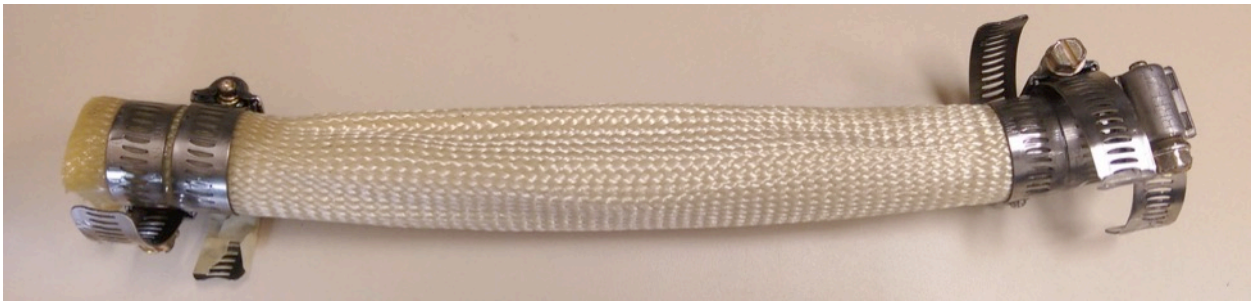

Figure 4.17. PAM with a Pharma-50 Silicone Tubing (7/8” OD, 5/8” ID) bladder and Vectran (nominal 1.5” OD) braided sleeve.

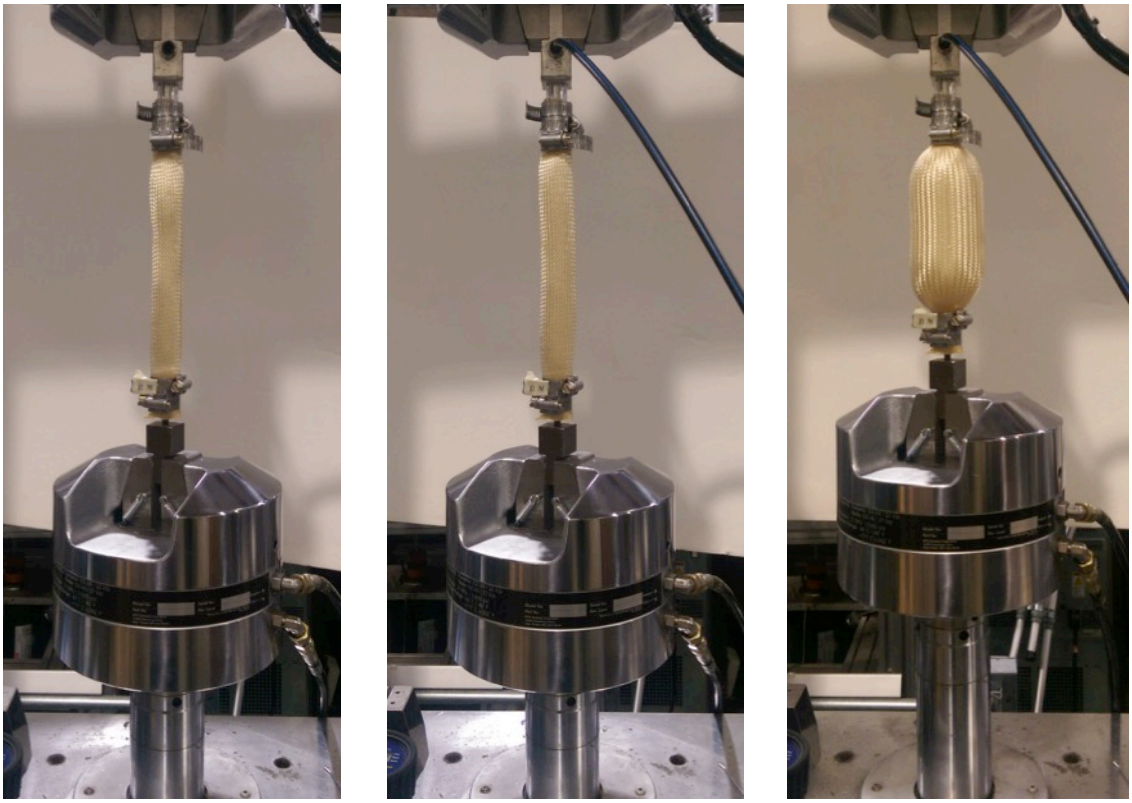

(a) Unpressurized (b) Blocked Force (c) Free Contraction

Figure 4.18. Quasi-static testing of a PAM with a Pharma-50 Silicone Tubing (1” OD, 7/8” ID) bladder and a Vectran (nominal 1.5” OD) braided sleeve.

4.4.2. Experimental Results

A summary of the properties of the three PAMs used for testing is provided in Table 4.8. The PAM with the Viton Fluoroelastomer Tubing (1" OD, 7/8" ID) bladder failed at its free contraction state while being cycled at 75 psi. A hole formed in the bladder along the natural fold of the Viton Fluoroelastomer Tubing. Because the failure happened away from the end fittings, the explanation for the failure is likely that the bladder was unable to handle the forces due to the pressurized air as a result of the bladder thickness and weakness along the fold due to the non-cylindrical shape of the tubing. Images of the failure are provided in Fig. 4.19. In the images, the braided sleeve has been cut away to reveal the location of the bladder failure.

Table 4.8: Properties of PAMs used in bladder comparison.

Bladder Material	Resting Length (in.)	Braid Angle Prediction (°)	Blocked Force @ 90 psi (lb)	Free Contraction @ 90 psi (%)
Latex Rubber Tubing (1" OD, ¾" ID)	7 3/4	72.5	1530	31.8
Viton Fluoroelastomer Tubing (1" OD, 7/8" ID)	7 3/4	n/a	n/a	n/a
Pharma-50 Silicone Tubing (7/8" OD, 5/8" ID)	7 7/8	74	1776	29.3

The force versus contraction profiles for each of the three PAMs are provided in Figs. 4.20-22. Experimental data was collected at 30 – 90 psi for the Latex Rubber Tubing (1" OD, ¾" ID) and the Pharma-50 Silicone Tubing (7/8" OD, 5/8" ID) bladders. For comparison, a complete set of loading and unloading data is provided for the Viton Fluoroelastomer Tubing (1" OD, 7/8" ID) bladder at 60 psi, and the single unloading portion of the force versus contraction curve prior to the bladder failure is provided for 75

psi. Additionally, the average experimental data from testing for the 60 and 90 psi cases are provided in Fig. 4.23. While the PAM with the Latex bladder achieved slightly better free contraction performance, by 2.5% contraction at 90 psi, the PAM with the Pharma-50 bladder generated 246 lb more force at its 90 psi blocked force state. The PAM with the Pharma-50 bladder also tended to produce a larger force over a majority of the percent contraction range relative to the PAM with the Latex bladder and the PAM with the Viton bladder at 60 psi.

(a)

(b)

Figure 4.19: Viton Fluoroelastomer Tubing (1” OD, 7/8” ID) bladder failure.

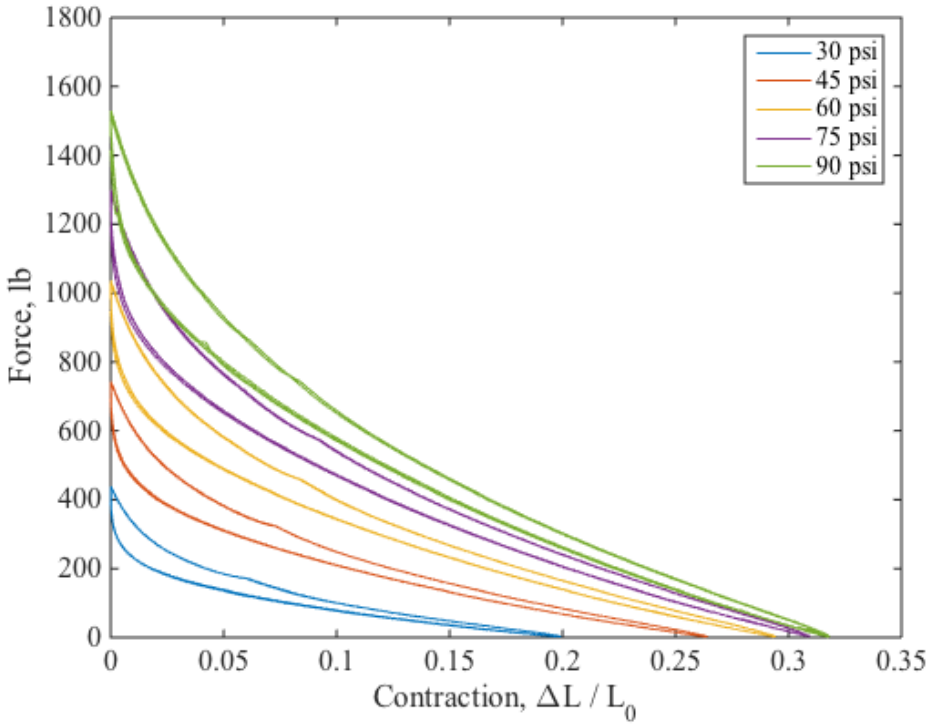

Figure 4.20. Experimental data for the force versus contraction profiles of pneumatic artificial muscles with a Latex (1" OD, ¾" ID) bladder and a Vectran (nominal 1.5" OD) braided sleeve.

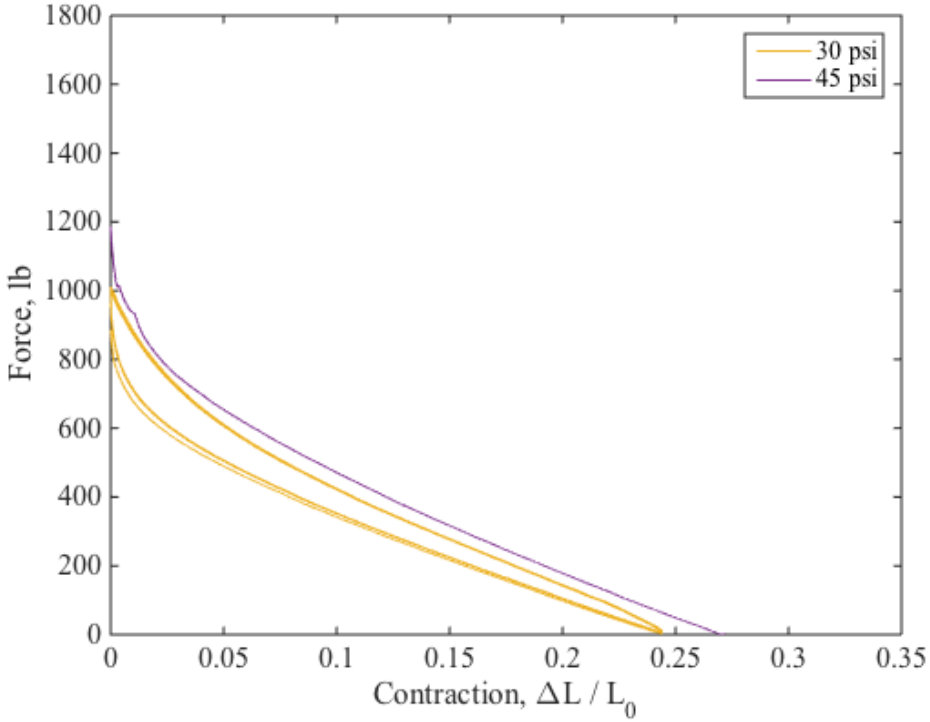

Figure 4.21. Experimental data for the force versus contraction profiles of pneumatic artificial muscles with a Viton (1" OD, 7/8" ID) bladder and a Vectran (nominal 1.5" OD) braided sleeve.

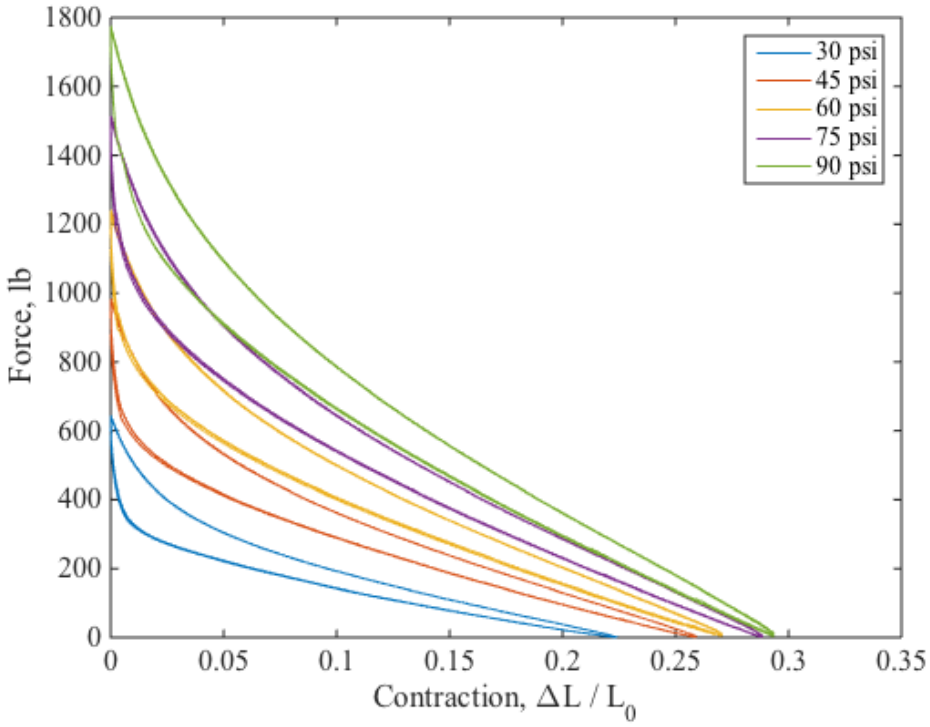

Figure 4.22. Experimental data for the force versus contraction profiles of pneumatic artificial muscles with a Pharma-50 (7/8" OD, 5/8" ID) bladder and a Vectran (nominal 1.5" OD) braided sleeve.

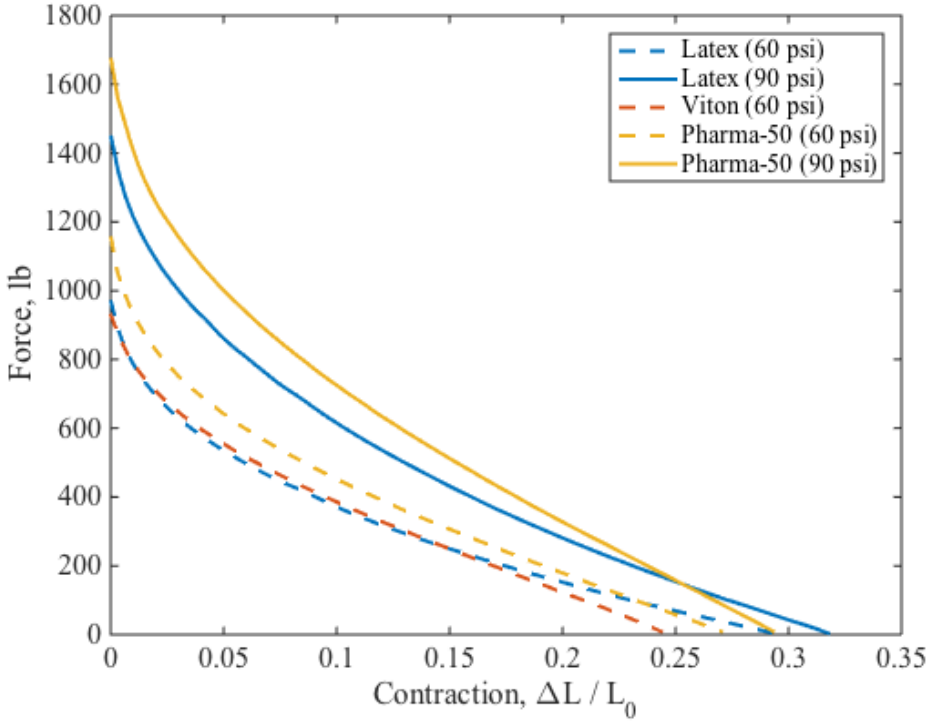

Figure 4.23. Average experimental data for the force versus contraction profiles of pneumatic artificial muscles with Latex, Viton, and Pharma-50 bladders and a nominal 1.5" OD Vectran braided sleeve.

A comparison of the hysteresis in the PAM data, for the bladder materials is provided in Table 4.9, using the hysteresis ratio from Eqn. 3.1. There is less hysteresis in the performance of the PAM with the Latex bladder than the PAM with the Pharma-50 bladder. Thus, the model of the average actuator behavior can better predict the actual performance of the actuator for the PAM with the Latex bladder.

Table 4.9: PAM hysteresis data—bladder comparison with Vectran braided sleeve (nominal 1.5" OD).

	Hysteresis Ratio				
Bladder Material	30 psi	45 psi	60 psi	75 psi	90 psi
Latex Rubber Tubing (1" OD, ¾" ID)	0.37	0.24	0.20	0.18	0.17
Viton Fluoroelastomer Tubing (1" OD, 7/8" ID)	n/a	n/a	0.27	n/a	n/a
Pharma-50 Silicone Tubing (7/8" OD, 5/8" ID)	0.42	0.31	0.28	0.23	0.22

The Mullins effect reveals another difference between the Latex and Pharma-50 bladders. The Mullins effect refers to the stress softening of a bladder material that occurs as a bladder experiences new maximum loading conditions. As the PAM is cycled at higher pressures, its blocked force and free contraction values increase until a steady state is reached for a given maximum pressure (Diani *et al.* 2009, Hocking and Wereley 2013).

The Mullins effect for each bladder is demonstrated in Fig. 4.24. For each bladder, the actuation profiles at 60 psi are provided after each PAM was cycled at 60 psi, 75 psi, and 90 psi in order of increasing pressure. The blocked force values increase slightly as the maximum cycling pressure is increased. However, the PAM with Pharma-50 bladder material experiences a much more significant increase in free contraction. Therefore, the performance of a PAM with a Pharma-50 bladder will be more dependent on the maximum loading conditions to which it has been previously exposed.

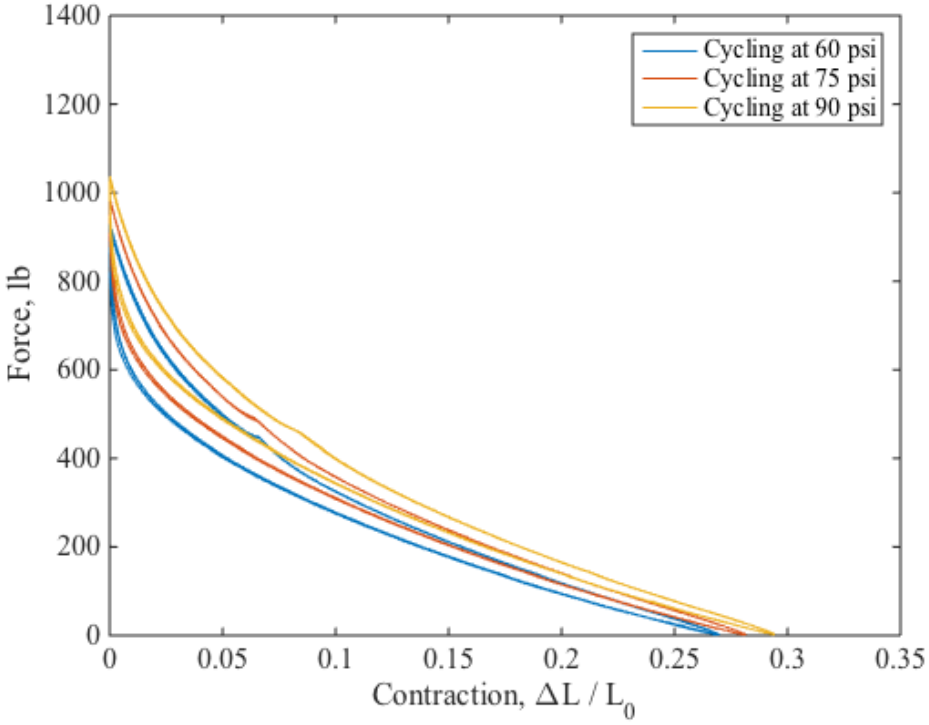

(a) Latex (1" OD, ¾" ID)

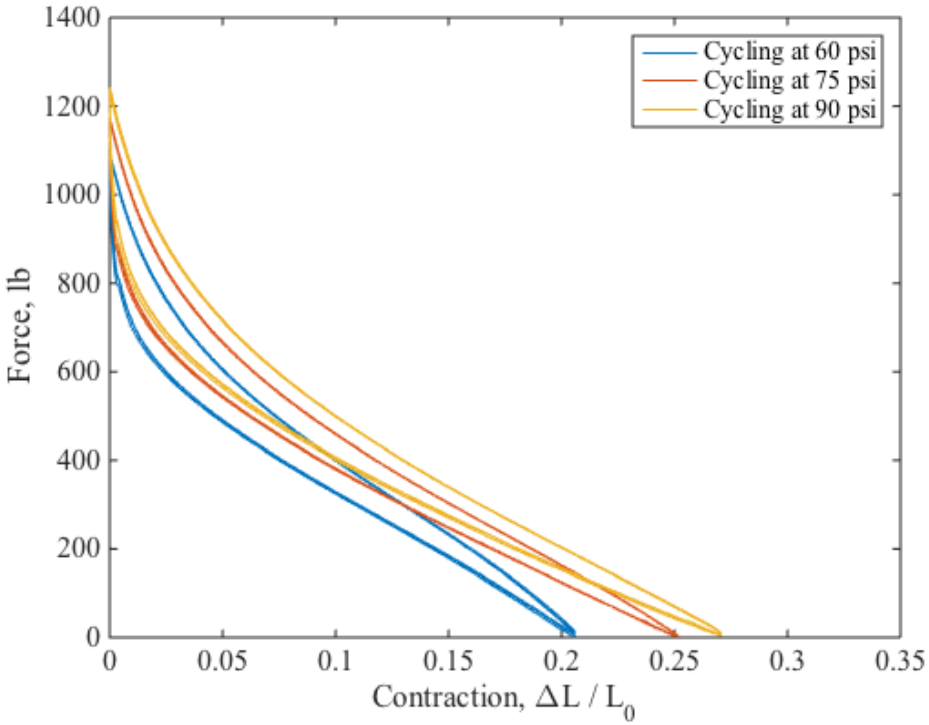

(b) Pharma-50 (7/8" OD, 5/8" ID)

Figure 4.24: Mullins effect: quasi-static experimental data at a pressure of (60 psi) after cycling at (60, 75, and 90 psi).

4.5. Conclusions

To assess the performance of candidate bladder and braided sleeve materials for space-qualified pneumatic artificial muscles, three different bladder materials and two different braided sleeve materials were compared using quasi-static testing. A PAM with a Latex Rubber Tubing (1" OD, ¾" ID) bladder and 1.5" OD Kevlar braided sleeve was used as the reference PAM for comparing the performance of the other materials. The Latex Rubber Tubing was compared to Viton Fluoroelastomer Tubing, with 1/8" and 1/16" thicknesses, and Pharma-50 Silicone Tubing, with a 1/8" thickness. The 1.5" OD Kevlar braided sleeve was compared to a 2" OD Kevlar braided sleeve and a 1.5" and 2" OD Vectran braided sleeve. The blocked force, free contraction, hysteresis, and general force versus contraction behavior for each PAM were experimentally determined and the results were compared.

The 1.5" OD Vectran braided sleeve was one of the top two performing braided sleeves and the better candidate for satisfying outgassing requirements. Three additional PAMs were made with this 1.5" OD Vectran braided sleeve and the Latex Rubber Tubing, Viton Fluoroelastomer Tubing, and Pharma-50 Silicone Tubing. While the PAM with the Viton Fluoroelastomer Tubing experienced a bladder failure during testing, the PAM with the Pharma-50 Silicone Tubing achieved higher blocked force values than the PAM with the Latex Rubber Tubing, and similar, although slightly lower, free contraction values. However, the PAM with the Pharma-50 Silicone Tubing experienced more hysteresis and a more significant stress softening of the bladder due to the Mullins effect.

In addition to assessing the performance of any additional bladder or braided sleeve candidates, the next step will be to choose a bladder and braided sleeve combination that meets NASA outgassing requirements and is able to achieve the necessary performance for a robotic application. A swaged end fitting design will need to be developed for the bladder and braided sleeve combination, which will ensure improved actuator robustness. Kothera *et al.* (2009) present a PAM developed using a swaging process in U.S. Patent No. 20090301292. Afterwards, burst testing, endurance testing, temperature range evaluations, and thermal cycling can be conducted to further assess the space-qualified nature of the PAM. Additional future design considerations include shielding against radiation and atomic oxygen.

5. Conclusions

5.1. Summary of Research and Key Conclusions

For this thesis, the agonistic and antagonistic actuation behavior of a bundle of miniature PAMs were experimentally characterized and modeled. These models were used to motivate the application of a variable recruitment control strategy to a parallel bundle of miniature PAMs as an attempt to mimic the selective recruitment of motor units in a human muscle. The unidirectional bundle models were then used to develop a model for a bidirectional actuator composed of an antagonistic pair of bundles of miniature PAMs.

Additionally, full-scale PAMs were fabricated from candidate space qualified bladder and braided sleeve materials. The actuation behaviors of the candidate space qualified PAMs were determined through quasi-static testing, and the experimental results were compared to determine which candidate space qualified materials could be used to make PAMs that are able to achieve the necessary load requirements for space robotics applications. The key results of this research are described as follows.

5.1.1. Variable Recruitment of Pneumatic Artificial Muscles

In this first study, the relationship between the application of a variable recruitment control strategy to a bundle of miniature PAMs and the selective recruitment of motor units in a human muscle is described. The fabrication, characterization, and modeling procedures for an individual miniature PAM are described, and a new model is presented to predict the quasi-static actuation behavior of a bundle of miniature PAMs

that accounts for length variations of miniature PAMs in the bundle. The model provides significant improvements in modeling accuracy from a simple summation of the actuation behavior of the individual miniature PAMs in the bundle.

The experimental and modeling results are used to motivate the application of a variable recruitment control strategy, through the comparison of energy equivalent configurations and operating efficiency calculations. Additionally, the losses in system efficiency due to length variations between miniature PAMs in the bundle demonstrate the need for improved accuracy in miniature PAM fabrication techniques.

5.1.2. Antagonistic Pair of Bundles of Miniature Pneumatic Artificial Muscles

The second study involved the development of a bidirectional actuator composed of an antagonistic pair of miniature PAM bundles. The antagonistic actuation behavior of a miniature PAM bundle was accurately modeled using the same modeling technique applied for the agonistic behavior of a miniature PAM bundle to account for the variation in active lengths of the miniature PAMs in the bundle. The improvements in the model accuracy from a simple summation of the force generated by the individual miniature PAMs were much more significant for the antagonistic bundle behavior than the agonistic bundle behavior due to the high passive stiffness of PAMs as they are stretched past their resting lengths.

Experimental testing of the bidirectional actuator revealed the need to account for hysteresis in the miniature PAM data when developing a model to predict the actuation behavior of the system. The results also highlighted the limited range of motion for bidirectional actuators without including a bias contraction and corresponding bias

pressure. A detailed outline of the system geometry and modeling approach is provided. Additionally, the expected performance of energy equivalent configurations is compared and the results support the conclusion from the unidirectional actuator study that it is most efficient to operate the fewest number of miniature PAMs necessary to achieve a desired performance objective by operating the active PAMs at higher pressures.

5.1.3. Space Qualified Pneumatic Artificial Muscles

In the third study, the benefits of developing PAMs from space qualified materials for use in space robotics are presented. Testing is performed on a different bladder and braided sleeve materials that are candidates for meeting space qualification requirements. The actuation performance and properties, including blocked force, free contraction, and hysteresis of the candidate bladder and braided sleeve materials were compared to the performance of a reference PAM assembled from a standard Latex Rubber Tubing bladder and Kevlar braided sleeve. The top-performing braided sleeve candidate was paired with the top-performing bladder materials for additional testing, which included a comparison of the stress softening of the bladder materials.

5.2. Contributions to Variable Recruitment and Space Qualified PAM Studies

The primary contribution of this research was the characterization and model development for the actuation behavior of bundles of miniature PAMs. This work advances current knowledge gained from previous variable recruitment studies by expending the work to include PAMs on the miniature scale. This testing offered

additional insights into modeling improvements that were less noticeable at the larger scales considered previously.

The experimental characterization of a bundle of miniature PAMs demonstrated the quasi-static actuation behavior of the bundle. The data revealed a nonlinear increase in force as the number miniature PAMs increased, as well as a slight loss in force generation due to inactive miniature PAMs in the bundles. The results also highlighted the performance benefits of operating the fewest number of necessary miniature PAMs at their highest operating pressure. A model was proposed to predict the agonistic force generation and contraction behavior of a bundle of miniature PAMs by accounting for the length and performance variations in the individual miniature PAMs included in the bundles. The proposed model was able to better predict the actuation behavior of the miniature PAM bundles than a simple summation of the individual miniature PAM actuation behaviors, providing a significant improvement in the model accuracy.

The efficiency benefits of applying a variable recruitment control technique to a bundle of miniature PAMs were predicted using the output mechanical work from the models, as well as the estimated input energy at each operating pressure. The results indicated that although there is the slight loss in system efficiency as more variation was introduced into bundles through the addition of new miniature PAMs, this loss was outweighed by the benefits of operating the fewest number of miniature PAMs in more optimal pressure ranges. However, the need to minimize the physical variations in the miniature PAMs included in bundles, through enhancements to the accuracy and precision of the miniature PAM fabrication process, was demonstrated. Small reductions

in the length variations within a bundle can provide significant improvements in bundle force production and efficiency.

The antagonistic actuation behavior of bundles of miniature PAM were also characterized and modeled using the same modeling technique by accounting for the length and performance variations in the individual miniature PAMs included in the bundles. The proposed model was able to better predict the antagonistic behavior of the miniature PAM bundles than a simple summation of the individual miniature PAM antagonistic behaviors, providing a significant improvement in the model accuracy. The model improvement was more significant for predicting than antagonistic behavior than the agonistic behavior due to the high passive stiffness of PAMs as they are extended past their resting length.

A bidirectional actuator composed of an antagonistic pair of miniature PAM bundles was developed. The actuation behavior of the agonist-antagonist pair was characterized and a model was proposed to predict the quasi-static actuation behavior. Improvements in modeling accuracy for the bi-directional actuator were achieved when the agonistic and antagonistic bundle behavior were modeled using individual miniature PAM models that captured the hysteresis in the miniature PAM actuation behavior. Additionally, the efficiency benefits of operating the minimum number of miniature PAMS necessary to achieve a desired deflection angle at higher operating pressures were demonstrated through the consideration of energy equivalent configurations.

Finally, full-scale PAMs were fabricated from candidate bladder and braided sleeve materials for meeting space qualification requirements and their quasi-static actuation behavior was characterized. Experimental data and observations related to the

blocked force, free contraction, hysteresis, and bladder stress softening properties of the PAMs were compared. To utilize PAMs in space robotics, PAMs that are able to generate the necessary loads must be developed from space qualified materials.

5.3. Suggestions for Future Work

This thesis focused on the characterization and modeling of the quasi-static behavior of bundles of miniature PAMs. The next logical step in this research would be to characterize and model the dynamic behavior of a single bundle of miniature PAMs, as well as the dynamic behavior of an antagonistic pair of miniature PAM bundles in a bidirectional actuator configuration. Dynamic modeling would require accounting for airflow dynamics, thermodynamics of the pressurized air, PAM volume fluctuations and deadband pressures, and system dynamics, including inertia, stiffness, and damping terms However, it would more effectively capture the actuation behavior of robotic manipulators during operation.

Once the dynamic behavior of the miniature PAM bundle actuators is understood, the dynamic models can be used to develop a variable recruitment control strategy for the actuators. A proof of concept actuator and variable recruitment controller could be used to better assess the performance and efficiency benefits of the control technique.

Future work should also include improvements to the fabrication process for miniature PAMs to minimize the variations in resting lengths. The losses in the force generation capabilities of the bundle were modeled by accounting for the length variations of the miniature PAMs in the bundle. A reduction in resting length variations would correspond to an increase in force generation capabilities of a bundle of miniature PAMs and improvements in the overall system efficiency. An alterative approach would

be to develop a shimming process to effectively match the actuator length of each miniature PAM in a bundle.

Additional candidate space qualified bladder and braided sleeve materials should be used to fabricate candidate space qualified PAMs for quasi-static characterization. Mass loss testing, temperature range evaluations, and thermal cycling would need to be conducted to determine if the materials can meet space qualification requirements. Additionally, burst testing and endurance testing should be completed once a space qualified bladder and braided sleeve combination is selected and a swaged end fitting design is developed for the space qualified PAM.

References

Ariga, Y., Maeda, D., Pham H. T. T., Uemura, M., Hirai, H., and Miyazaki, F., 2012, "Equilibrium-Point Control of Agonist-Antagonist System with Pneumatic Artificial Muscles: Application to EMG-Based Human-Machine Interface for an Elbow-Joint System," *2012 IEEE/RSJ Int. Conf. on Intell. Robots and Systems*, pp. 4380-4385. DOI: 10.1109/IROS.2012.6385790

ASTM E1559-09, 2009, "Standard Test Method for Contamination Outgassing Characteristics of Spacecraft Materials," *ASTM International*. DOI: 10.1520/E1559-09

ASTM E2089-15, 2015, "Standard Practices for Ground Laboratory Atomic Oxygen Interaction Evaluation of Materials for Space Applications" *ASTM International*. DOI: 10.1520/E2089-15

ASTM E595-15, 2015, "Standard Test Method for Total Mass Loss and Collected Volatile Condensable Materials from Outgassing in a Vacuum Environment," *ASTM International*. DOI: 10.1520/E0595-15

Azizi, E. and Roberts, T. J., 2013, "Variable gearing in a biologically inspired pneumatic actuator array," *Bioinspir. Biomim.* **8**. DOI: 10.1088/1748-3182/8/2/026002

Banks, B. A., de Groh, K. K., and Miller, S. K., 2004, "Low Earth Orbital Atomic Oxygen Interactions with Spacecraft Materials," *2004 Materials Research Society Fall Meeting*, *Materials Research Society Symposium Proc. 2004, NN8.1*, Cambridge University Press, New York. Also published as NASA/TM-2004-213400 (2004).

Boblan, I., Bannasch, R., Schwenk, H., Prietzel, F., Miertsch, L., and Schulz, A., 2004, "A Human-like Robot Hand and Arm with Fluidic Muscles: Biologically Inspired Construction and Functionality," *Embodied Artificial Intelligence*, Springer-Verlag, Berlin, pp. 160-179. DOI: 10.1007/978-3-540-27833-7_12

Bryant, M., Meller, M. A., and Garcia, E., 2014, "Variable Recruitment Fluidic Artificial Muscles: Modeling and Experiments," *Smart Mater. Struct.*, **23**. DOI: 10.1088/0964-1726/23/7/074009

Caldwell, D. and Tsagarakis, N., 2002, "Biomimetic Actuators in Prosthetic and Rehabilitation Applications," *Technol. Health Care*, **10**, pp. 107-20.

Chen, Y., Yin, W., Lui, Y., and Leng, J., 2011, "Structural Design and Analysis of Morphing Skin Embedded with Pneumatic Muscle Fibers," *Smart Mater. Struct.*, **20**. DOI: 10.1088/0964-1726/20/8/085033

Chou, C-P., and Hannaford, B., 1996, "Measurements and Modeling of McKibben Pneumatic Artificial Muscles," *IEEE Trans. Rob. Autom.*, **12**, pp. 90-102. DOI: 10.1109/70.481753

Chou, C-P., and Hannaford, B., 1994, "Static and Dynamic Characteristics of McKibben Pneumatic Artificial Muscles, *Proc. ICRA*, **1**, pp. 281-6. DOI: 10.1109/ROBOT.1994.350977

Colbrunn, R. W., *Design and Control of a Robotic Leg with Braided Pneumatic Actuators*, M.S. thesis, Case Western Reserve University, 2000. DOI: 10.1109/IROS.2001.976298

Davis, S. and Caldwell, D., 2006, "Braid Effects on Contractile Range and Friction Modeling in Pneumatic Muscle Actuators," *Int. J. Robot. Res.*, **25**, pp. 359-69. DOI: 10.1177/0278364906063227

De Volder, M., Moers, A. J. M., and Reynaerts, D., 2011, "Fabrication and Control of Miniature McKibben Actuators," *Sensors Actuators A*, **166**, pp. 111-6. DOI: 10.1016/j.sna.2011.01.002

Deaconescu, A. and Deaconescu, T., 2009, "Performance of a Pneumatic Muscle Actuated Rotation Module," *Proc. World Congress on Engineering*, **2**. DOI: 10.1.1.148.5736

Dever, J. A., Banks B. A., de Groh K. K., and Miller, S. K., 2005, "Degradation of Spacecraft Materials," *Handbook of Environmental Degradation of Materials*, Kutz, M., ed., William Andrew Publishing, Norwich, NY, pp. 465-501.

Diani, J., Fayolle, B., and Gilormini, P., 2009, A Review on the Mullins Effect," *Eur. Polym. J.*, **45**, pp. 601-12 DOI: 10.1016/j.eurpolymj.2008.11.017

Erim, Z., De Luca, C. J., Mineo, K. and Aoki, T., 1996, "Rank-Ordered Regulation of Motor Units," *Muscle & Nerve*, **19**, pp. 563-73.

Finckenor, M. M. and de Groh, K. K., 2015, *A Researcher's Guide to: International Space Station: Space Environmental Effects*, Rai, A. and Hosein, N., eds., *NASA*.

GEVS-SE Rev A General Environmental Verification Specification for STS & ELV Payloads, Subsystems and Components, 1996, *NASA*.

Henneman, E., Somjen, G., and Carpenter, D. O., 1965a, "Excitability and Inhibitibility of Motoneurons of Different Sizes," *J. Neurophysiol.*, **28**, pp. 599-620.

Henneman, E., Somjen, G., and Carpenter, D. O., 1965b, "Functional Significance of Cell Size in Spinal Motoneurons," *J. Neurophysiol.*, **28**, pp. 560-580.

Hocking, E. G. and Wereley, N. M., 2013, "Analysis of Nonlinear Elastic Behavior in Miniature Pneumatic Artificial Muscles," *Smart Mater. Struct.*, **22**. DOI: 10.1088/0964-1726/22/1/014016

Kang, B-S., Kothera, C. S., Woods, B. K. S., and Wereley, N. M., 2009, "Dynamic Modeling of McKibben Pneumatic Artificial Muscles for Antagonistic Actuation," *IEEE Int. Conf. on Robotics and Automation*, pp. 182-187. DOI: 10.1109/ROBOT.2009.5152280

Klute, G. and Hannaford, B., 1998, "Fatigue Characteristics of McKibben Artificial Muscle Actuators," *Proc. IROS*, **3**, pp. 1776-1782. DOI: 10.1109/IROS.1998.724854

Kothera, C. S., Jangid, M., Sirohi, J., and Wereley, N. M., 2009, "Experimental Characterization and Static Modeling of McKibben Actuators," *J. Mech. Design*, **131**. DOI: 10.1115/1.3158982

Kothera, C., Wereley, N. M., and Woods, B. K. S., 2009, "Fluidic Artificial Muscle Actuator and Swaging Process Therefor," U.S. Patent No. 20090301292.

"Materials and Processes Technical Information System (MAPTIS)," http://maptis.nasa.gov/, *NASA*.

Meller, M. A., Chipka, J. B., Bryant, M. J., and Garcia, E., 2015, "Modeling of the Energy Savings of Variable Recruitment McKibben Muscle Bundles," *Proc. SPIE*, **9429**. DOI: 10.1117/12.2084444

Park, Y-L., Chen, B-R., Pérez-Arancibia, N. O., Young, D., Stirling, L., Wood, R. J., Goldfield, E. C., and Nagpal, R., 2014, "Design and Control of a Bio-Inspired Soft Wearable Robotic Device for Ankle-Foot Rehabilitation," *Bioinspir. Biomim.*, **9**. DOI: 10.1088/1748-3182/9/1/016007

Peel, L. D., Mejia, J., Narvaez, B., Thompson, K., and Lingala, M., 2009, "Development of a Simple Morphing Wing Using Elastomeric Composites as Skins and Actuators," *Jour. Mechanical Design*, **131** (9), DOI: 10.1115/1.3159043

Pillsbury, T. E., Kothera, C. S., Wereley, N. M., 2015, "Effect of Bladder Wall Thickness on Miniature Pneumatic Artificial Muscle Performance," *Bioinspir. Biomim.*, **10**. DOI: 10.1088/1748-3190/10/5/055006

Pillsbury, T. E., Kothera, C. S., Wereley, N. M., and Akin, D. L., 2015, "Pneumatically Power Assisted Extra-Vehicular Activity Glove," *45th Int. Conf. on Environmental Systems*.

Robinson, R. M., Kothera, C. S., Woods, B. K. S., Vocke, R. D., Wereley, N. M., 2011, "High Specific Power Actuators for Robotic Manipulators," *J. Intell. Mater. Syst. Struct.*, **22**, pp. 1501-1511. DOI: 10.1177/1045389X11417653

Robinson, R. M., Kothera, C. S., and Wereley, N. M., 2014, "Variable Recruitment Testing of Pneumatic Artificial Muscles for Robotic Manipulators," *IEEE Trans. Mechatronics*, **20** (4), pp. 1642-1652. DOI: 10.1109/TMECH.2014.2341660

Röthling, F., Haschke, R., Steil, J. J., and Ritter, H., 2007, "Platform Portable Anthropomorphic Grasping with the Bielefeld 20-DOF Shadow and 9-DOF TUM Hand," *Proc. 2007 IEEE/RSJ Int. Conf. Intell. Robot. Syst.*, pp. 2951-2956. DOI: 10.1109/IROS.2007.4398963

Salmoiraghi, A. J. and Akin, D. L., 2012, "Review of Wearable Robotic Assistive Devices for Integration with Pressure Suit Arms," *42nd Int. Conf. on Environmental Systems*. DOI: 10.2514/6.2012-3487

Sasaki, D., Noritsugu, T., Takaiwa, M., and Yamamoto, H., 2004, "Wearable Power Assist Device for Hand Grasping using Pneumatic Artificial Rubber Muscle," *Proc. 2004 IEEE Int. Workshop on Robot and Human Interactive Comm.*, pp. 655-660. DOI: 10.1109/ROMAN.2004.1374840

Shin, D., Khatib, O., and Cutkosky, M., 2009, "Design Methodologies of a Hybrid Actuation Approach for a Human-Friendly Robot," *IEEE Int. Conf. on Robotics and Automation*, pp. 4369–4374. DOI: 10.1109/ROBOT.2009.5152744

Shin, D., Yeh, X., and Khatib, O., 2011, "Variable Radius Pulley Design Methodology for Pneumatic Artificial Muscle-Based Antagonistic Actuation Systems," *IEEE/RSJ Int. Conf. on Intell. Robots and Systems*, pp. 1830-1835. DOI: 10.1109/IROS.2011.6095180

Tadano, K., Akai, M., Kadota, K., and Kawashima, K., 2010, "Development of Grip Amplified Glove using Bi-articular Mechanism with Pneumatic Artificial Rubber Muscle," *2010 IEEE Int. Conf. on Robotics and Automation*, pp. 2363-2368. DOI: 10.1109/ROBOT.2010.5509393

Tondu, B., 2012, "Modelling of the McKibben Artificial Muscle: A Review," *J. Intell. Mater. Syst. Struct.*, **23**, pp. 225-253. DOI: 10.1177/1045389X11435435

Tondu, B., Ippolito, S., Guiochet, J., and Daidie, A., 2005, "A Seven-Degrees-of-Freedom Robot-Arm Driven by Pneumatic Artificial Muscles for Humanoid Robots," *Int. J. Robot. Res.*, **24**, pp. 257-274. DOI: 10.1177/0278364905052437

Tondu, B. and Lopez, P., 1997, "The McKibben Muscle and its use in Actuating Robot-Arms Showing Similarities with Human Arm Behaviour," *Ind. Robot: Int. J.*, **24** (6), pp. 432–439. DOI: 10.1108/01439919710192563

Tözeren, A., 2000, *Human Body Dynamics: Classical Mechanics and Human Movement*, Springer-Verlag, New York, pp. 14-21, 172-176.

Vermeulen, J., Verrelst, B., Vanderborght, B., Lefeber, D., and Guillaume, P., 2006, "Trajectory Planning for the Walking Biped 'Lucy,'" *Int. J. Robot. Res.*, **25**, pp. 867-87. DOI: 10.1177/0278364906069343

Vocke III, R. D., Kothera, C. S., Chaudhuri, A., Woods, B. K. S., Wereley, N. M., 2012, "Design and Testing of a High-Specific Work Actuator Using Miniature Pneumatic Artificial Muscles," *J. Intell. Mater. Syst. Struct.*, **23**, pp. 365-378. DOI: 10.1177/1045389X11431743

Vocke III, R. D., Kothera, C. S., and Wereley, N. M., 2014, "Mechanism and bias considerations for design of a bi-directional pneumatic artificial muscle actuator," *Smart Mater. Struct.*, **23** (12). DOI: 10.1088/0964-1726/23/12/125039

Watkins, J., 2014, *Fundamental Biomechanics of Sport and Exercise*, Routledge, New York, pp. 127-129.

Wilcox, B., Ambrose, R., and Kumar, V., 2006, "Space Robotics," *International Assessment of Research and Development in Robotics*, World Technology Evaluation Center, Inc., pp. 25-39, Chap. 3.

Winter, D. A., 2005, *Biomechanics and Motor Control of Human Movement*, 3rd ed., John Wiley & Sons, Hoboken, pp. 203-209.

Woods, B. K. S., Gentry, M. F., Kothera, C. S., and Wereley, N. M., 2012, "Fatigue Life Testing of Swaged Pneumatic Artificial Muscles as Actuators for Aerospace Applications," *J. Intell. Mater. Syst. Struct.*, **23**, pp. 327-343. DOI: 10.1177/1045389X11433495

Woods, B. K. S., Kothera, C. S., Wang, G., Wereley, N. M., 2014, "Dynamics of a Pneumatic Artificial Muscle Actuation System Driving a Trailing Edge Flap," *Smart Mater. Struct.*, **23** (9), 2014. DOI: 10.1088/0964-1726/23/9/095014

Woods, B. K. S., Kothera, C. S., and Wereley, N. M., 2011, "Wind Tunnel Testing of a Helicopter Rotor Trailing Edge Flap Actuated via Pneumatic Artificial Muscles," *J. Intell. Mater. Syst. Struct.*, **22**, pp. 1513-1528. DOI: 10.1177/1045389X11424216

Wu, J., Huang, J., Wang, Y., and Xing, K., 2010, "A Wearable Rehabilitation Robotic Hand Driven by PM-TS Actuators," *Intelligent Robotics and Applications*, Liu, H., Ding, H., Xiong, Z. and Zhu, X., eds., Springer-Verlag, Berlin, **6425**, pp. 440-450. DOI: 10.1007/978-3-642-16587-0_41

Ying, C., Jia-fan, Z., Can-jun, Y., and Bin, N., 2007, "Design and Hybrid Control of the Pneumatic Force-Feedback Systems for Arm-Exoskeleton by Using On/Off Value," *Mechatronics*, **17**. DOI: 10.1016/j.mechatronics.2007.04.001